NEARSIDE AND FARSIDE:
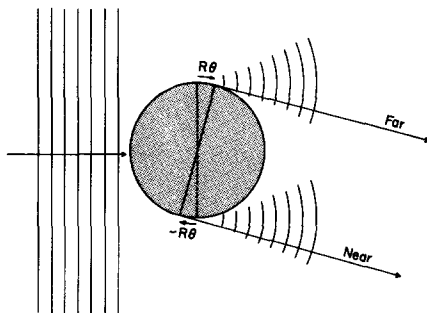# THE OPTICS OF HEAVY ION ELASTIC SCATTERING*

M. S. HUSSEIN

Instituto de Fisica, Universidade de Sao Paulo, C.P. 20516, Sao Paulo, Brazil

and

K. W. McVOY

Physics Department, University of Wisconsin-Madison, Madison, WI 53706, U.S.A.

Abstract—Sommerfeld's edge-wave formulation of diffraction is employed to show how angular distributions for heavy-ion elastic scattering can profitably be interpreted as 2-slit diffraction patterns modified by refraction. Just as in peripheral transfer reactions, each "slit" in the elastic amplitude is a peripheral ℓ-window, one in the nearside amplitude and one in the farside.

The nearside/farside decomposition thus has a particularly simple physical interpretation for high-energy scattering amplitudes from strong absorbers. We apply it to a variety of light heavy-ion data ($^6Li + {}^{90}Zr$, $^{16}O + {}^{28}Si$, $^{12}C + {}^{12}C$, etc.), to illustrate its ability to clarify such optical phenomena as Fraunhofer diffraction, nuclear rainbows, potential ambiguities and the forward glory effect. We also indicate its usefulness in nonoptical phenomena like the "polarization" amplitude describing absorption due to Coulomb excitation.

This article is dedicated to the memory of John Blair, who contributed so much to our understanding of nuclear optics.

CONTENTS

1. INTRODUCTION

1.1. Purpose of the review

Certain features of nuclear scattering, such as fine-structure compound-nucleus resonances, involve the full complexity of the nuclear many-body problem, and in general can be treated only in a statistical approximation like that of the Hauser–Feshbach approach. Direct reactions, on the other hand, occur too quickly to excite complex degrees of freedom, and so produce angular distributions which often are determined simply by the geometry of the interaction, plus a few mean-field parameters. Because the complex many-body effects manifest themselves in the fine-structure of the energy dependence, they can be suppressed by energy averaging. This enhances effects like bulk refraction or diffraction, due to the "simple" degrees of freedom of the scatterers, which can then be understood in mean-field terms.

Phenomenological local optical potentials are an example of such a mean-field approach, and have long proved their usefulness in both light-ion and heavy-ion collisions, as a remarkably successful means of producing a "prejudiced phase-shift analysis" of energy-averaged angular distributions. In the light-ion, low-energy regime of traditional tandem experiments, involving few partial waves, the angular distributions are very "quantum mechanical", and one has simply had to accept the optical-potential fits to the data as facts

of nature, with little insight into their physical content and even less into how the computer search attained them, or how variations in the V, W, R and a parameters of the potentials would produce corresponding variations in the angular distributions.

As heavier projectiles have become available, and as bombarding energies have increased, the number of partial waves involved has correspondingly grown, reflecting decreased wavelengths and the ever-closer approach to the simplifications of the ray-optics limit. This is the domain of semi-classical or WKB approximations, and we wish here to seek out those among them which are most appropriate to "high energy" heavy-ion scattering (high in a sense to be defined precisely below). Our purpose is to demonstrate how they can be put to very practical use, both in understanding the physical (i.e., optical) meaning of these angular distributions (such as the fact that they are "pure shadow"), and in obtaining simple analytic expressions showing how their characteristic features depend on the optical model parameters and on the bombarding energy.

1.2. The 2-slit picture of absorbers

The central key to understanding these high-energy angular distributions is the edge-diffraction phenomenon illustrated in Fig. 1a, which is caused by the *strong absorption* feature of heavy-ion optical potentials in their central regions.[1,2] The point of the figure is that *any sharp edged absorber*, i.e., one which is uniformly black across most of its area, produces a diffraction pattern which can be described in terms of *"edge waves" alone*.[3]

As an extreme example, consider the familiar sharp-cutoff black-disc amplitude of the Blair model, $f(\theta) = iRJ_1(kR\theta)/\theta$. Outside its central maximum, its diffraction rings are *equally spaced* in angle, $\Delta\theta = \pi/kR$, a sure sign of a *2 source* interference pattern. This is difficult to see from the customary Kirchoff integral, which writes $f(\theta)$ as an integral over the *area* of the disc. However, Born and Wolf[3] point out, following Sommerfeld, that for $kR \gg 1$ the area integral can be done by stationary phase, and reduces to an integral around the *periphery* of the disc, describing the edge wave. The central maximum of the diffraction pattern thus arises from a "shining rim". As θ increases, however, the bright sections of the rim shrink to two diametrically-opposed bright *spots* in the "scattering plane", as indicated
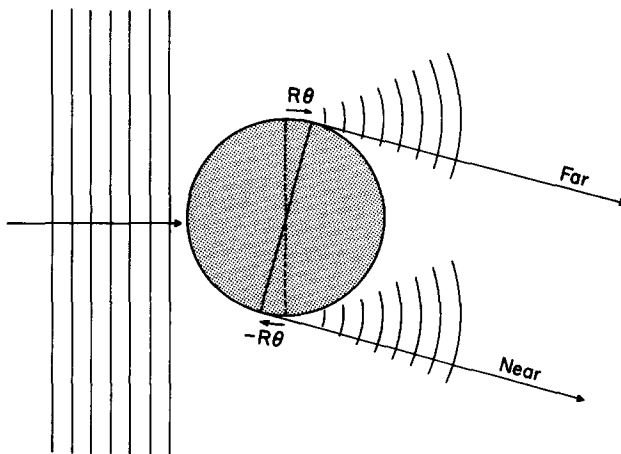

Fig. 1a. Schematic indication of the edge-waves generated by a plane wave incident on a spherical absorber.
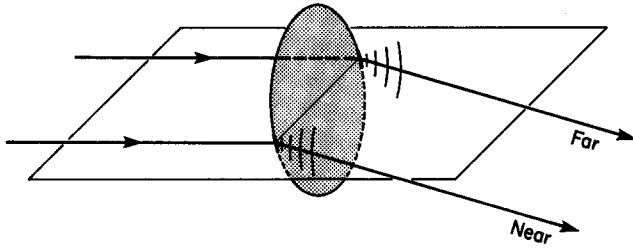
Fig. 1b. Edge waves generated by a black disc, indicating their localization in the reaction plane for θ outside the central diffraction peak.

in Fig. 1b, and shown in detail in Section 2.2.1 below. Mathematically, this simply describes the asymptotic form of $J_1(kR\theta)$,

$$f(\theta) = iRJ_1(kR\theta)/\theta$$

$$\simeq \frac{-R}{(2\pi k\theta)^{1/2}}[e^{-i(L\theta-\pi/4)} - e^{i(L\theta-\pi/4)}], \quad (L = kR, \quad L\theta > 1), \quad (1.1)$$

but physically its two running-wave components describe the edge-waves originating from the two bright spots, whose fixed separation $\Delta\ell = 2L$ is responsible for the constant period, $\Delta\theta = 2\pi/\Delta\ell$, of the diffraction pattern. This will become even clearer in Section 1.4 below when we obtain the analogous scattering amplitude for an absorber with a "rounded" edge, of finite thickness a. Provided that $a \ll R$, this amplitude is also a sum of two such terms, but each one has the diffraction-fan shape of transmission through an ℓ-window of width ka, making its physical meaning unambiguous.

Any such elastic-scattering diffraction pattern can thus profitably be viewed as a 2-slit interference pattern: it is the fixed separation between the two slits which determines the (constant) period $\Delta\theta = \pi/kR$ of its Fraunhofer diffraction pattern, while the width ka of the ℓ-window determines its angular envelope (single-slit pattern). Since the slit-separation $2R$ is fixed, the variations observed in heavy-ion angular distributions must arise primarily from changes in this single-slit pattern. Our review is consequently a study of the two ℓ-window diffraction patterns, which we identify with the "Near-side" and "Far-side" components of the full scattering amplitude. In particular, any parametrization of the full angular distri-

Fig. 1c. Identification of Near (positive-angle) and Far (negative-angle) trajectories.

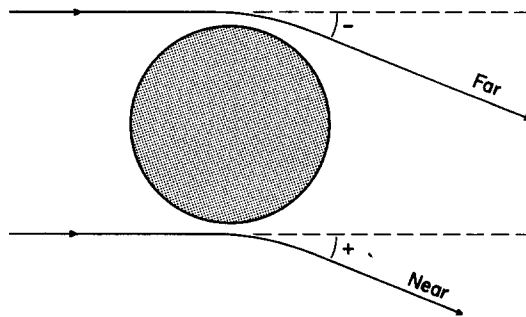bution in terms of potential parameters is found to be very efficiently done in terms of these two component amplitudes separately. It is this which makes the N/F decomposition particularly useful for strong absorbers.

The review is thus intended as a practical aid to optical-model practitioners, but also as an attempt to provide as much insight as possible into the significance of features like diffraction oscillations, absorbed rainbows, exponential shadows and orbiting. We are following in a time-honored path of semi-classical footsteps, which has generated a substantial literature, beginning with the classic work of Ford and Wheeler[4] on real-potential scattering. The most significant advances made since that time are, in our opinion, those of Frahn and collaborators[1] (the strong-absorption approach) and of Knoll and Schaeffer[5] (the refractive approach, but with diffraction included via complex ℓ's).

Unfortunately, neither approach has been widely applied in the analysis of data. That of Knoll and Schaeffer (a semi-classical technique for evaluating optical potential scattering amplitudes), which uses the powerful and elegant methods[6,7] of complex angular momentum, is the more fundamental of the two, but the complex-plane mathematics are somewhat forbidding, and have not previously lead to simple closed formulae suggesting how the scattering amplitudes depend on the optical potential parameters.

In contrast, Frahn's overriding purpose, sometimes pursued at the price of oversimplification, was precisely to obtain "closed form" expressions for the scattering amplitude. They were not based on optical potentials at all, but rather on parametrizations of the S-matrix elements $S(\ell)$ in ℓ-space—an attractive idea in view of the known fact that optical potentials generally provide an "overparametrized" form of the scattering amplitude, as shown by the existence of different but "phase-equivalent" potentials.

As far as we are aware, it was Frahn who first recognized the central importance of the 2-slit or edge-wave interpretation of the scattering amplitude for strong absorbers, but by great misfortune he was ahead of his time in two respects. For one, the physical significance (independent of the edge-wave phenomenon) of the Near-side/Far-side decomposition had not yet been appreciated when Frahn began his work, so there was no *general* framework available to fit it into. Secondly, the experimental data available at that time for elastic heavy-ion angular distributions were largely limited to the very small-angle region of the "Fresnel oscillations", which is so Coulomb-dominated as to be only minimally sensitive even to peripheral features of the nucleus–nucleus interaction; it was to these small-angle features that most of Frahn's attention was directed. It is only presently that data (at least for the lighter-ion systems) are becoming available at energies high enough to reach impact parameters where Fraunhofer interference and possible refractive effects like nuclear rainbows are becoming important; Frahn's insight into the two-slit nature of the angular distributions was never really put to an interesting test in his parametrized models.

We have learned much from both the Frahn and the Knoll and Schaeffer approaches. Our real purpose in the present review is (1) to translate their rather obscure mathematical formulae into the simple physical language of the 2-slit diffraction picture, (2) to generalize the Frahn picture (using some of the Knoll and Schaeffer ideas) to include refractive effects more realistically than he was able to in his simple parametrizations, and (3) to show how both approaches can be seen as particular applications of the more general Near-side/Far-side decomposition technique. We do this by using optical potentials to generate the phase shifts necessary for such a decomposition, not because this is necessarily the most fundamental means of generating scattering amplitudes, but for the practical reason that most fits to elastic data are currently done via optical potentials, and because fast optical codes exist to which the Near/Far decomposition can readily and inexpensively be appended. Further-

more, the "equal geometry" parametrizations of the Frahn type are distinctly too limited to provide adequate fits to current heavy-ion data. It seems to us that Frahn's search for a "model-independent" phase-shift parametrization to be fitted to data is a very sensible goal. If it is ever to be achieved, it will certainly have to be in Near/Far terms, like the ones generated[1] so far. The optical potential offers itself as a convenient crutch for the moment, to permit a familiarity with Near/Far decompositions to be developed. But it is, fundamentally, merely a special (and local) phase-shift parametrization of a somewhat obscure sort; a more direct one may someday be found.

1.3. Examples of Near-side/Far-side decompositions

As Fig. 1c indicates, Near-side trajectories are the positive-angle ones (like Coulomb trajectories), corresponding to a repulsive interaction or reflection; Far-side trajectories are negative-angle ones, passing behind the target, caused in general by a combination of diffraction and attractive–interaction refraction. Any scattering amplitude can be written (in a manner defined precisely below) as a sum of Near-side and Far-side components,

$$f(\theta) = f_N(\theta) + f_F(\theta),$$

whose most important property is that the Fraunhofer diffractive oscillations occur in neither f_N nor f_F, but only in their interference; other types of interference, such as rainbow minima, occur in either f_N or f_F alone.
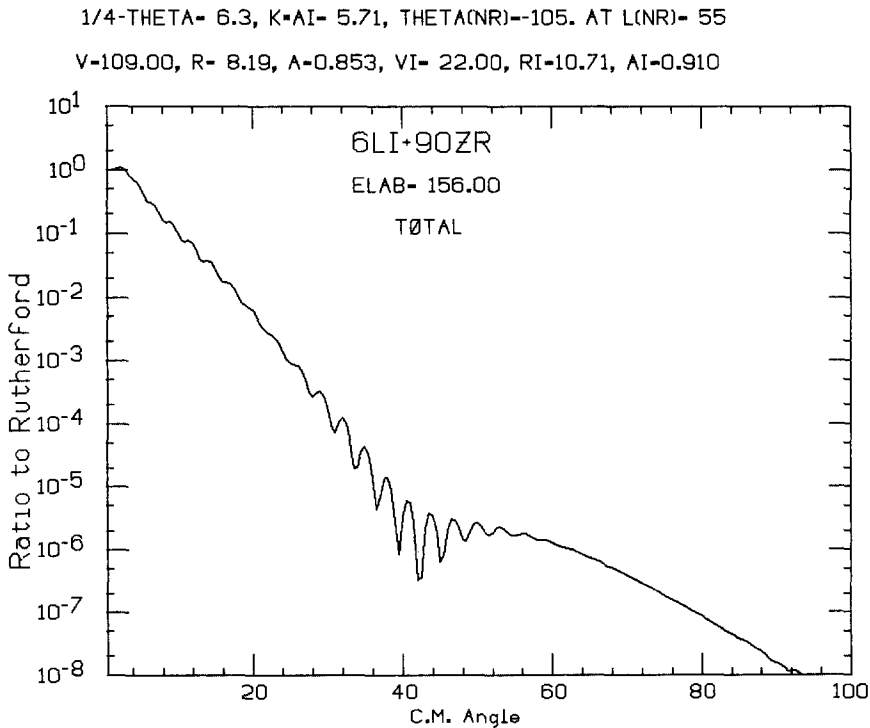
Fig. 2. Elastic angular distribution, ^{6}Li + ^{90}Zr. The W-S potential parameters for all angular distributions shown are given in the legends at the tops of the figures.

1/4-THETA-20.1, K*AI- 6.20, THETA(NR)--175. AT L(NR)-234

V-100.00, R- 5.87, A-0.640, VI- 50.00, RI- 5.87, AI-0.640
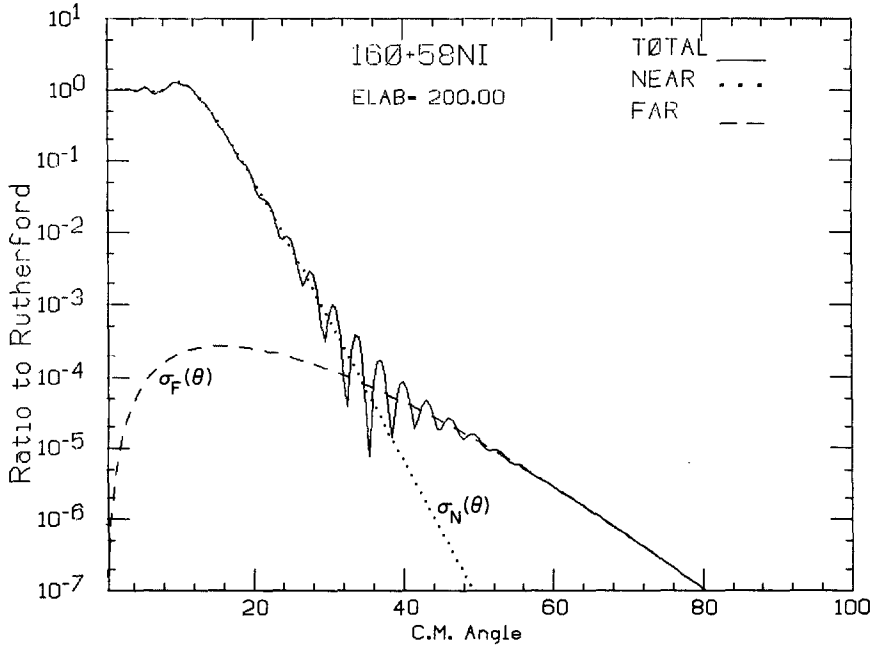
Fig. 3a. $d\sigma/d\sigma_R$ for $^{16}O + ^{58}Ni$, with N/F components.

1/4-THETA-20.1, K*AI- 6.20, THETA(NR)--175. AT L(NR)-234

V-100.00, R- 5.87, A-0.640, VI- 50.00, RI- 5.87, AI-0.640
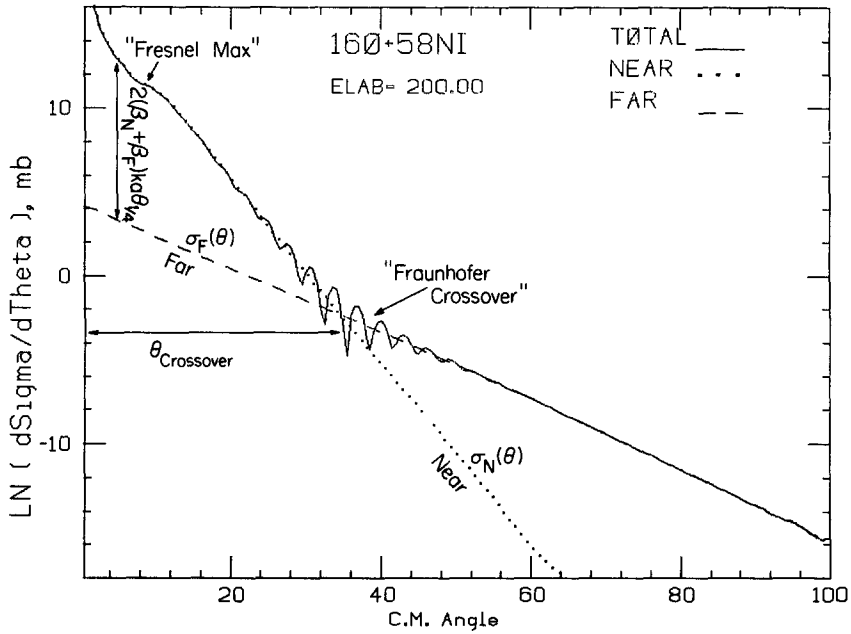
Fig. 3b. $d\sigma/d\theta$ for the same potential.

M. S. Hussein and K. W. McVoy

1/4-THETA-20.1, K*AI- 6.20, THETA(NR)--175. AT L(NR)-234

V- 0.00, R- 5.87, A-0.640, VI- 50.00, RI- 5.87, AI-0.640

16Ø+58NI

ELAB- 200.00

TØTAL ——
NEAR ...
FAR — —
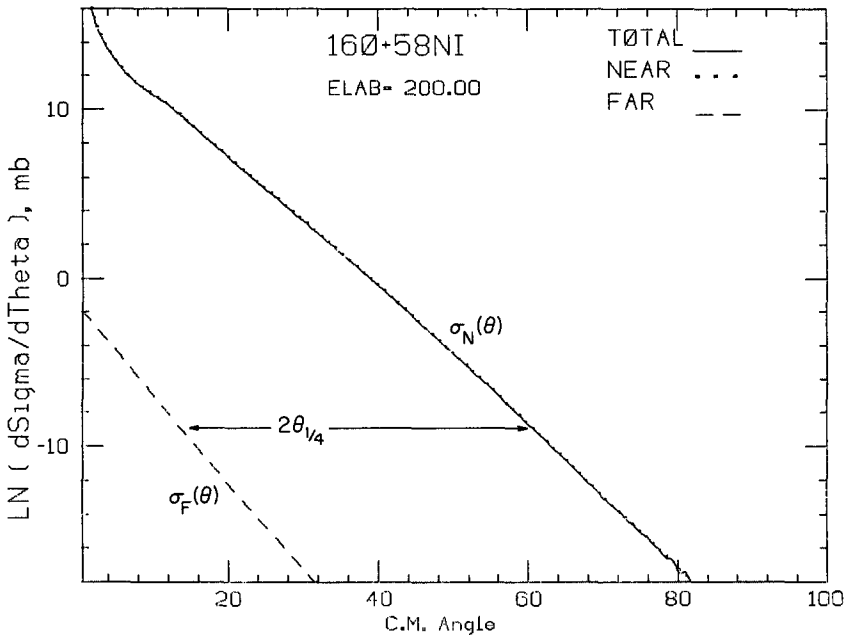
Fig. 3c. Same as 3b, with $V = 0$. $\sigma_N(\theta) \simeq \sigma_F(\theta - 2\theta_{1/4})$, where $\theta_{1/4}$ is the Coulomb shift.

As a prototype example of such decompositions, Fig. 2 shows an optical model angular distribution recently fitted to data[8] for 156 MeV ^{6}Li on ^{90}Zr, and Fig. 3a shows a very similar one calculated for 200 MeV ^{16}O on ^{58}Ni, *assuming* a "refractive type" optical potential, $V = 100$ MeV, $W = 50$ MeV. The Near/Far decomposition for the ^{6}Li case will be given later. For the moment we consider the ^{16}O + ^{58}Ni case (even though the potential is not yet known and is probably not "refractive") because its larger Coulomb repulsion separates the "Fresnel" oscillations at very forward angles more clearly from the "Fraunhofer" oscillations around 35°. Figure 3b shows the same angular distribution in the form of a logarithmic plot of $d\sigma/d\theta = 2\pi \sin\theta \, d\sigma/d\Omega$, rather than the customary $(d\sigma/d\Omega)/(d\sigma_R \, d\Omega)$ of Fig. 3a; its advantage is that any exponential falloff as a function of angle shows up clearly as a straight line.* This figure also includes the "cross sections"

$$\sigma_N(\theta) = 2\pi \sin\theta \, |f_N(\theta)|^2$$

and

$$\sigma_F(\theta) = 2\pi \sin\theta \, |f_F(\theta)|^2, \tag{1.2}$$

and shows directly that the diffractive oscillations near 35° result from Near/Far (N/F) interference between otherwise-smooth amplitudes. For comparison, Fig. 3c shows the same cross-sections, but with $V = 0$. This is scattering by a pure absorber (plus the Coulomb field). It is entirely Near-dominated, with no refraction whatever; furthermore $\sigma_N(\theta)$ and

---

* Note that the "Fresnel maximum" of Fig. 3a, at 14°, is reduced to a "shoulder" at the same angle in $d\sigma/d\theta$. It is this shoulder in all subsequent $d\sigma/d\theta$ plots which marks the transition from Coulomb to nuclear scattering.
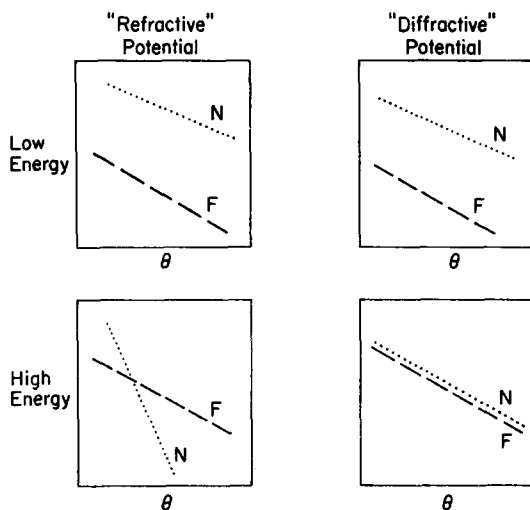
Fig. 3d. Schematic caricature of $\sigma_N(\theta)$ and $\sigma_F(\theta)$ for refractive and diffractive potentials.

$\sigma_F(\theta)$ are parallel straight lines on a logarithmic plot. Figures 3b and 3c thus show that, for this interaction, $\sigma_N(\theta)$ and $\sigma_F(\theta)$ both decay exponentially (the entire angular range beyond the Coulomb shoulder is classically forbidden), with slopes which are equal when $V = 0$, but different when $V \neq 0$.

To insure that the reader does not "miss the forest for the trees", we provide in Fig. 3d a schematic indication of the behavior of $\sigma_N(\theta)$ and $\sigma_F(\theta)$ for the two extremes of a "refractive" potential (roughly, $V \gg W$, in Woods–Saxon terms) and a "diffractive" potential ($V < W$). The strong refraction of the former is seen to give $\sigma_N(\theta)$ a much larger slope than that of $\sigma_F(\theta)$ (at energies well above the Coulomb barrier), so that they cross one another "quickly" in θ, producing the localized Fraunhofer oscillations of Fig. 3b. In a less-refractive potential, $\sigma_N(\theta)$ and $\sigma_F(\theta)$ are closer to being parallel, as in Fig. 3c; if their magnitudes are comparable, this will cause a much wider range of Fraunhofer oscillations, as in the familiar black-disc example.

We remark in passing that all N/F decompositions presented here were computed with a VAX version of the PTOLEMY computer code, which is available on request from the University of Wisconsin.

1.4. Geometry-dominance in Born approximation

The underlying N and F amplitudes are thus seen to be remarkably simple. Why should this be, and what determines the slopes of their exponential falloffs? By far the simplest hint can be obtained by recourse to the Born approximation. Since E_{cm}/V is only 1.5 in this example, Born is certainly inadequate here (as we will see explicitly), but it *is* useful at higher energy, and its *form* provides exactly the type of insight we are after. For a spherically symmetric potential it gives the scattering amplitude

$$f(\theta) = -(2\mu/\hbar^2) \int_0^\infty j_0(qr)V(r)r^2 \, dr$$

$$= (i\mu/\hbar q^2) \int_0^\infty (e^{iqr} - e^{-iqr})V(r)r \, dr. \tag{1.3}$$
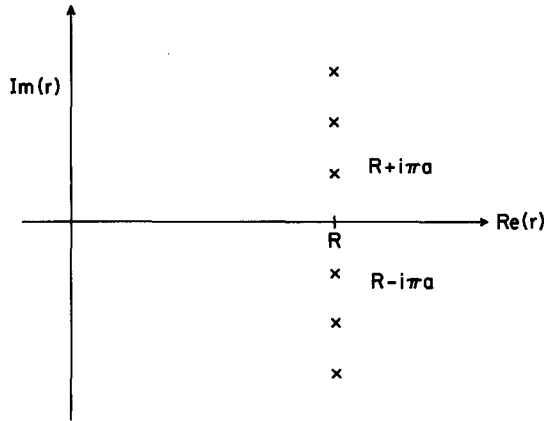
Fig. 4. Pole positions of $W\text{-}S$ potential in the complex r-plane.

The two terms in the integral correspond exactly to the Far-side and Near-side amplitudes. To evaluate them most simply we note, with Amado et al.[9], that an essential feature of the nuclear matter distribution is that it is "thin-skinned", i.e., that its surface thickness a is small compared to its radius R. This feature is traditionally represented by a Woods–Saxon shape for the radial matter distribution,*

$$U(r) = -\frac{V+iW}{1+e^{(r-R)/a}}. \tag{1.4}$$

As Ericson remarked long ago[10], the thin-skin feature is expressed in analytic-function terms by the fact that $V(r)$ has *poles* in the complex r-plane, at the points

$$R_n = R \pm i\pi a n, \quad n = 1, 3, \ldots, \tag{1.5}$$

shown in Fig. 4. We presume this to be a general feature of leptodermous potentials, and follow Amado et al.[9] in noting that, in the angular range

$$\frac{1}{\pi k a} \ll \theta \ll \frac{R}{a}\frac{1}{\pi k a}, \tag{1.6}$$

i.e., in the range covered by roughly the first 10 diffraction oscillations, the integrals in eqn. (1.3) can be evaluated by using 1st and 4th-quadrant contours in the r-plane. In the angular range (1.6), they are found to be dominated by the residues of the $n = \pm 1$ poles of (1.5), giving

$$f(\theta) = f_F(\theta) + f_N(\theta),$$

where, provided that $V(r)$ and $W(r)$ have the *same geometry*,

$$f_F(\theta) = CR_1\,e^{iqR_1},$$

(Equal geometry, Born Approximation)   (1.7)

---

* The argument is greatly simplified by neglecting the Coulomb interaction at this stage; its effect on $f_N(\theta)$ and $f_F(\theta)$ is well known to be just a shift in angle, which we include in eqn. (1.10) and verify in Section 3.5.

$$f_N(\theta) = CR_1^* e^{-iqR_1^*} = -f_F^*(\theta),$$

where

$$C = -(8\pi\mu/\hbar^2)(V+iW)(aR/q).$$

That is, for small angles where $q(\theta) \simeq k\theta$,

$$f_N(\theta) = C(R - i\pi a) e^{-ikR\theta} e^{-\pi ka\theta},$$

$$f_F(\theta) = C(R + i\pi a) e^{ikR\theta} e^{-\pi ka\theta}. \tag{1.8}$$

The result (1.7) shows in strikingly simple fashion how the *edge geometry* of the potential dominates the scattering in the $E \gg V$ limit, where refraction becomes weaker than absorption. In fact, (1.7) and (1.8) contain the essence of our entire optical message. Although given only for positive angles, these results are symmetric about $\theta = 0$, and in fact describe nothing more than the two-slit diffraction pattern indicated in Fig. 1a. The surface region at each limb of the target acts like a slit or ℓ-window (one N and one F), generating a diffracted wave from the region where the potential varies most rapidly with r (i.e., where $-V'(r)$, the radial force on the projectile, is largest). Each ℓ-window, of width ka, produces a diffraction fan of angular width $\sim 1/ka$, with an envelope $\simeq \exp -\pi ka|\theta|$. The path length of the far-side ray exceeds that of the near-side ray by the distance $2R\theta$, travelled along the surface of the scatterer (see Fig. 1a), making their phase difference $2\pi (2R\theta/\lambda) = 2kR\theta$, as indicated by the exponential factors in (1.8). Thus the condition for maxima in the 2-slit interference pattern is the usual

$$n\lambda = d \sin\theta \simeq 2R\theta,$$

so that the angular separation between successive maxima ($\Delta n = 1$) is $\Delta\theta = \lambda/2R$, i.e.,

$$\Delta\theta = \frac{\pi}{kR} \simeq \frac{\pi}{L_{max}}, \tag{1.9}$$

as usual for Fraunhofer interference. In the limit that $a \to 0$, the single-slit patterns do not decay exponentially and combine, as expected, to give the customary $J_1(L\theta)/\theta$ angular distribution of a sharp-edged black disc.

Thus it becomes clear why the Near/Far decomposition is so useful for the amplitude of an edge-scatterer: the N and F components each describe the diffraction pattern of a single slit or ℓ-window, which is clearly a simpler pattern to study than the full cross-section containing their interference.

This two-slit picture is the subject of our entire study. Its essential features are captured by (1.7), which is certainly correct at sufficiently high energies, and has had great success[9] in describing proton scattering by nuclei above 500 MeV. High-energy electron-nucleus scattering is similarly geometry-dominated, and could also doubtless be effectively described in N/F terms. However, nucleus–nucleus scattering in the few hundred MeV range, which concerns us here, is *not* yet geometry-dominated. Refraction (both Coulomb and nuclear) still plays a substantial role in determining the orientation and shape (asymmetry) of the single-slit patterns at these energies. Most of our efforts in subsequent sections will be devoted to understanding these refractive effects, which can roughly be summarized by the following improvement on (1.8) (again valid only for equal real and imaginary geometries):

$$f_N(\theta) \propto e^{-ikR\theta} e^{-\beta_N ka(\theta - \theta_{1/4})}$$

$$f_F(\theta) \propto e^{ikR\theta} e^{-\beta_F ka(\theta + \theta_{1/4})}, \tag{1.10}$$

where

$$\theta_{1/4} = \tan^{-1}(2\eta/kR) \cong V_{\text{coul}}(R)/E, \tag{1.11}$$

and

$$0 < \beta_F < \beta_N \leqslant \pi \tag{1.12}$$

are limits on the slope parameters for attractive real potentials, showing that attractive refraction makes the Near slope steeper than the Far.* This, combined with the Coulomb enhancement of σ_N over σ_F, given by

$$\ln\frac{\sigma_N(0)}{\sigma_F(0)} = 2(\beta_N + \beta_F)ka\theta_{1/4} \leqslant 4\pi ka\theta_{1/4}, \tag{1.13}$$

(indicated in Fig. 3b) shows how the N/F "crossover" is brought about by refraction superimposed on absorption. This predicts, in fact, that the crossover occurs at the angle

$$\theta_{\text{cross}} = \frac{\beta_N + \beta_F}{\beta_N - \beta_F}\theta_{1/4} \simeq \frac{\beta_N + \beta_F}{\beta_N - \beta_F}\frac{V_{\text{coul}}(R)}{E} \tag{1.14}$$

also indicated in Fig. 3b. Clearly this will produce a visible effect on the cross-section only if $\theta_{\text{cross}} < \pi$; in particular, if $\beta_N = \beta_F$, as in the case of pure absorption ($V = 0$), $\theta_{\text{cross}} \to \infty$ and no crossover occurs at all. Much oversimplified estimates of the slope parameters (not often valid) are

$$\beta_N \simeq \pi - \tan^{-1}(W/V), \qquad \text{(Caution!)} \quad (1.15)$$
$$\beta_F \simeq \tan^{-1}(W/V).$$

They are incorrect in not containing energy dependence, but do correctly show that $\beta_N = \beta_F$ if $V = 0$.

Altogether, these formulae provide an example of how semiclassical methods can provide useful estimates, in the form of N/F decompositions, of the dependence of heavy-ion elastic amplitudes on optical-potential parameters. Our purpose below is to explain the origin and physical significance of formulae like these, and to provide their more realistic generalizations. In particular, we are not inquiring into the *origin* of the potential itself, folding or otherwise. Rather, given a local optical potential, we merely investigate its optics.†

1.5. Further examples

An example of heavy-ion scattering by another "refractive-type" potential is given in Fig. 5, which shows how the angular distribution of one of the potentials (F75), employed at low energy by Cramer et al.[11] for $^{16}O + ^{28}Si$ scattering, changes with bombarding energy.‡ At energies near the 25-MeV Coulomb barrier (Fig. 5a), the scattering is N-side dominated over the entire angular range because the Coulomb field keeps all trajectories outside the nuclear force range. At higher energy (Fig. 5b) both the Near and Far sides are modified by the nuclear potential, the strong nuclear attraction producing N/F crossover at large angles.

---

* Both β_N and β_F depend on E (see below) and $\to \pi$ as $E \to \infty$.

† In the spirit of Goethes' observation on phenomenology: "Gott gibt uns die Nuesse, aber er bricht sie nicht auf."

‡ In this and most subsequent angular distributions, we plot $d\sigma/d\theta = 2\pi \sin\theta\, d\sigma/d\Omega$, rather than $d\sigma/d\sigma_R$, to make exponential falloffs readily recognizable.

1/4-THETA-61.6, K*AI- 2.25, THETA(NR)- -79. AT L(NR)- 12

V-100.00, R- 5.89, A-0.640, VI- 42.00, RI- 5.89, AI-0.640

16Ø+28SI   TØTAL ___
ELAB- 40.00   NEAR ...
                     FAR ---

F75

LN (dSigma/dTheta), mb

C.M. Angle
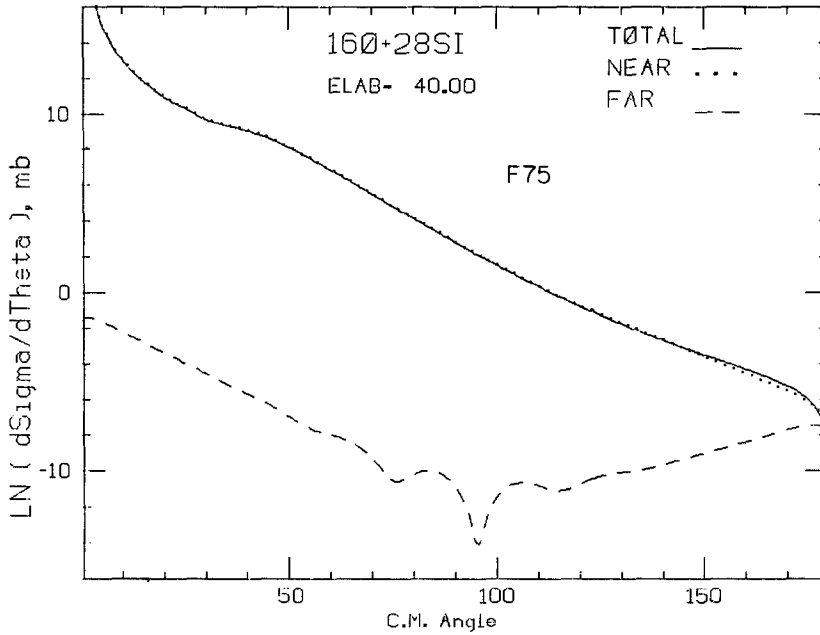
Fig. 5a. N/F decomposition for the "F75" potential of Cramer *et al.* of Ref. 11, at 40 MeV.

1/4-THETA-41.1. K*AI- 2.76, THETA(NR)--169. AT L(NR)- 99

V-100.00, R- 5.89, A-0.640, VI- 42.00, RI- 5.89, AI-0.640

16Ø+28SI   TØTAL ___
ELAB- 60.00   NEAR ...
                     FAR --

F75

LN (dSigma/dTheta), mb

C.M. Angle
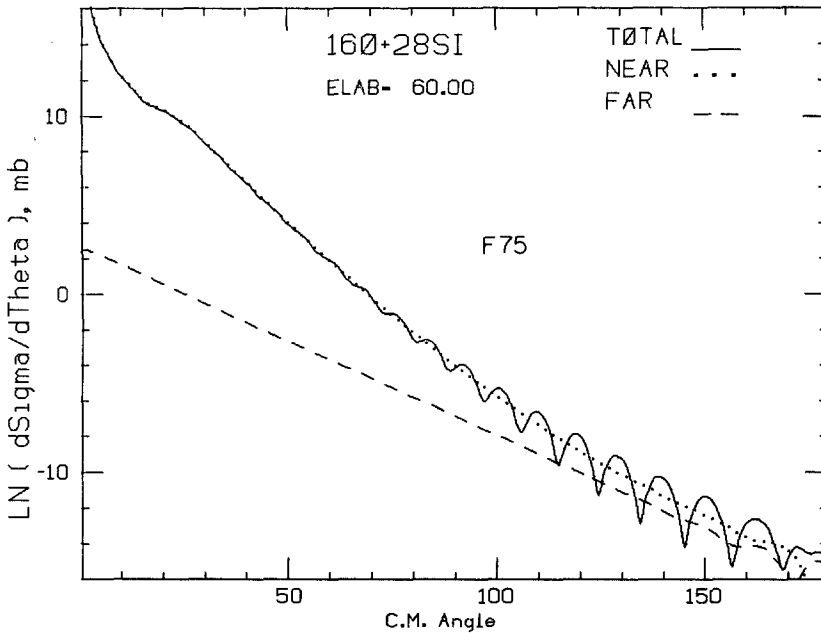
Fig. 5b. Same as 5a, at 60 MeV.

1/4-THETA-11.5, K*AI- 5.22, THETA(NR)--177. AT L(NR)-200
V-100.00, R- 5.89. A-0.640, VI- 42.00, RI- 5.89, AI-0.640

160+28SI

ELAB- 215.20

TØTAL ___
NEAR ...
FAR - -

F 75
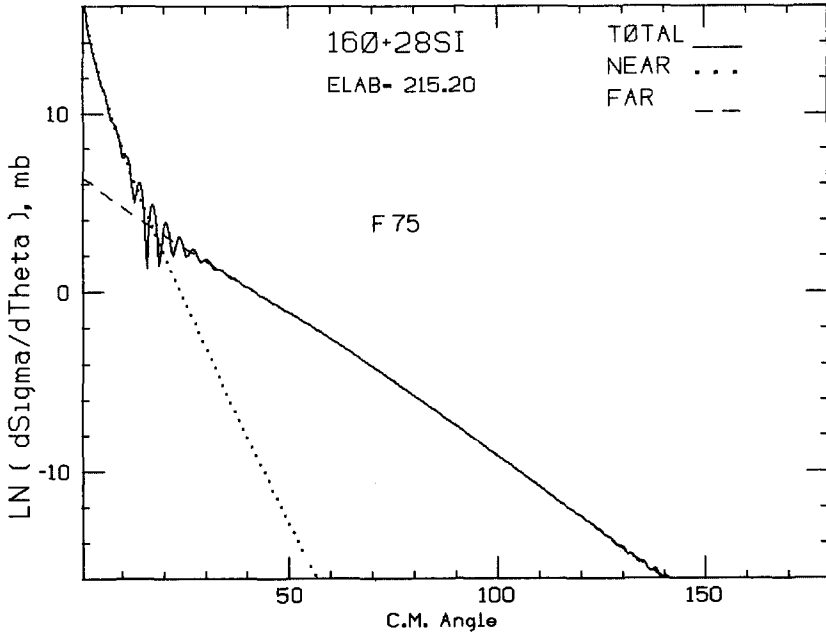
Fig. 5c. Same as 5a, at 215.2 MeV.

1/4-THETA- 9.9, K*AI- 4.51, THETA(NR)--177. AT L(NR)-200
V- 10.00, R- 7.50, A-0.618, VI- 23.40, RI- 6.83, AI-0.552

160+28SI

ELAB- 215.20

TØTAL ___
NEAR ...
FAR - -

"E18"
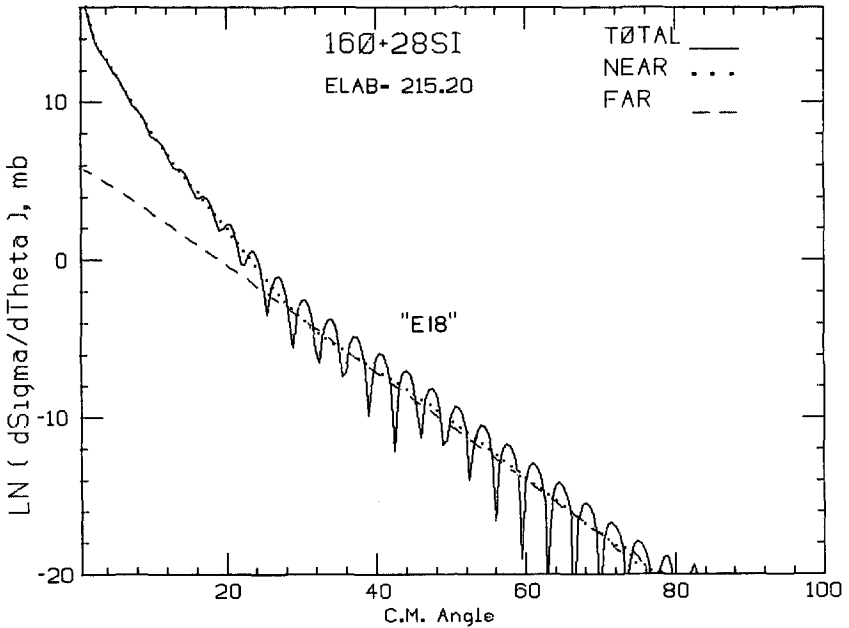
Fig. 6. The "E18" potential of Ref. 11, a potential of the "diffractive" type.

Finally, at the still higher energy of 215.2 MeV, the crossover has moved to forward angles and become very pronounced—in disagreement with the data at this energy, incidentally.

This potential does fit the data below $E_L = 80$ MeV, but its deep real potential (combined with equal real and imaginary geometries) gives too strong a crossover and subsequent Farside dominance at higher energies.

Figure 6 provides the very interesting N/F decomposition for the "diffractive-type" $E18$ potential of Cramer et al.,[11] whose much weaker real potential does fit the 215.2 MeV data. This potential does not produce a crossover, but rather generates *parallel* $\sigma_N(\theta)$ and $\sigma_F(\theta)$ falloffs beyond 30°, by an ingenious scheme to be analyzed in detail below. By making $\sigma_N(\theta) \simeq \sigma_F(\theta)$ over the entire angular range from 30° to 80°, this potential fills that entire angular range with diffractive oscillations.

As a final preliminary example, Fig. 7 shows the angular distribution which fits the data of Put and Paans[12] for 79.5 MeV α's on ^{90}Zr (measured out to about 150°). Its most important feature is the broad minimum-and-maximum at about 90° and 120°; they are clearly seen to be properties of the Far-side amplitude, and appear to be the best evidence so far available for a "nuclear rainbow", which will be discussed in more detail below. They provide one of the more interesting examples of structure due to $f_N(\theta)$ or $f_F(\theta)$ alone, rather than to their interference. In this case $f_F(\theta)$ is not edge-dominated, for its 90° minimum results from the interference of a peripheral-ℓ with an internal ℓ-contribution.

2. ELEMENTARY SEMI-CLASSICAL TECHNIQUES AND IMPORTANT OPTICAL THEOREMS

Although nuclei look like cloudy crystal balls to low-energy neutrons, they look more like

Fig. 7. Nuclear rainbow in $\sigma_F(\theta)$ for $\alpha + {}^{90}$Zr.

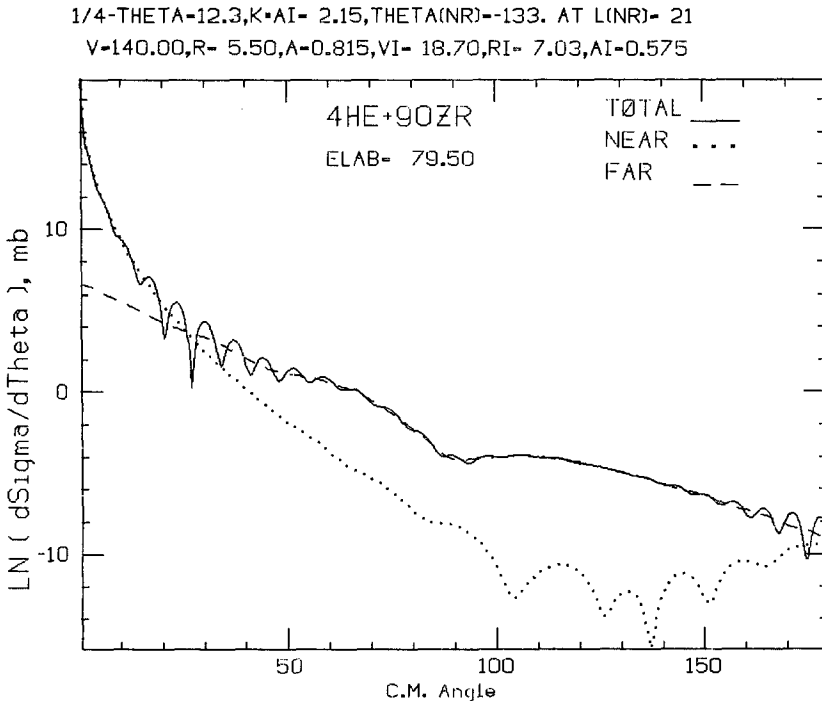black crystal balls to other nuclei. In fact, it is more subtle than that, for the detailed radial shapes of their refraction and absorption are critical to the resulting angular distributions, with such properties as "surface transparency" playing an important role. $\sigma_N(\theta)$ and $\sigma_F(\theta)$ become quite simple in the high energy range, roughly defined by $E \gtrsim V$, but to understand how and why, we need a few techniques and theorems from semiclassical or short-wavelength optics. These techniques provide an intriguing generalization of the customary textbook approach to optics, where refraction and diffraction are generally viewed as distinct phenomena. The essential point is that high energy heavy-ion scattering occurs almost entirely in classically forbidden angular regions, i.e., in the shadows cast by the peripheral ℓ-windows. The corresponding semi-classical impact parameters are complex, and at complex impact parameters diffraction and refraction merge into a single pheno-menon, for which the customary optical terminology is not always adequate. In this section we briefly review the necessary technology and obtain the theorems necessary to understand the features encountered in the examples of the previous section. Those readers interested only in the analysis of specific angular distributions can skip to Section 3, or even to Section 4.

2.1. The stationary-phase or saddle-point approximation to oscillatory integrals

Scattering amplitudes from spherically-symmetric scatterers are typically obtained in the form

$$f(q) = \int g(r)\,e^{iqr}\,dr, \tag{2.1}$$

where r ranges over all scattering centers in the target and the exponential "retardation factor" simply provides each center with its correct phase relative to the others. In the high energy limit, $q \to \infty$ and the integral will vanish entirely because of the high-frequency oscillations of the exponential factor, unless $g(r)$ contains compensating oscillations. If it does, the integral will be nonzero only at those q's for which this compensation occurs. These are just the q's corresponding to the classical-mechanics trajectories (or the geometric-optics rays) for this particular potential, and this is indeed the standard method for extracting the geometric-optics result from a general wave-mechanics scattering problem in the short-wavelength limit, $kR \gg 1$.

The standard form of the mathematical problem is an integral of the type

$$I = \int e^{i\phi(x)}\,dx, \tag{2.2}$$

generally with infinite limits, with $\phi(x)$ real on the line of integration and analytic in some region surrounding it. If $\phi(x)$ varies rapidly with x, the integral will be small, but if it has maxima or minima on the line of integration, these extrema will contribute the bulk of the integral, since they are just the points where the integrand fails to oscillate. If $\phi'(x_0) = 0$, then near that point

$$\phi(x) \simeq \phi(x_0) + \phi''(x_0)\,(x - x_0)^2/2.$$

If this is the only stationary point, the integral will come mainly from $x = x_0$, and it is customary to extend the limits to $\pm\infty$, since the contributions of far away points are strongly suppressed by oscillations, giving

$$I \simeq e^{i\phi(x_0)} \int_{-\infty}^{\infty} e^{i\phi''(x_0)(x-x_0)^2/2}\,dx = [2\pi i/\phi''(x_0)]^{1/2}\,e^{i\phi(x_0)} \tag{2.3}$$

If the stationary point occurs off the line of integration, at $x = z_0$, it is known as a saddle point, and a result of exactly the same form, evaluated at z_0, is obtained by deforming the contour to pass through z_0; the technique is then known as the method of steepest descents. In fact, even if the integrand contains a slowly-varying factor $A(x)$ in addition to the exponential, the approximation

$$\int A(x)\,e^{i\phi(x)}\,dx \simeq [2\pi i/\phi''(z_0)]^{1/2} A(z_0)\,e^{i\phi(z_0)}$$

where

$$\phi'(z_0) = 0, \tag{2.4}$$

is customarily employed, and is the one we shall use here. Its most frequent use is in the evaluation of an integral over impact parameters or ℓ-values.

2.2. The Near/Far decomposition

2.2.1. *Physical ideas and approximate formulae*

This decomposition of scattering amplitudes was employed by Ford and Wheeler[4] for purely practical mathematical reasons; the physical significance of f_N and f_F was recognized only later.[1,13-15] Perhaps the most physically direct way of being convinced of this significance is by considering a scattering (or reaction) amplitude in the standard form

$$f(\theta) = \int e^{i\mathbf{k}_f \cdot \mathbf{r}} V(r)\phi_\mathbf{k}^{(+)}(\mathbf{r})\,d^3r. \tag{2.5}$$

Choosing the z-axis along the incident $\mathbf{k}$ direction, and letting $\mathbf{k}_f$ and $\mathbf{r}$ make angles θ and θ' relative to it, respectively, $\mathbf{k}_f \cdot \mathbf{r} = k_f r \times (\cos\theta \cos\theta' + \sin\theta \sin\theta' \cos\phi)$, with ϕ as the azimuthal angle of $\mathbf{r}$ relative to $\mathbf{k}_f$: $\phi = 0$ and $\phi = \pi$ are points in the reaction plane containing $\mathbf{k}$ and $\mathbf{k}_f$. If $V(r)$ is a central potential, $V(r)\phi_\mathbf{k}^+(\mathbf{r})$ will have no ϕ-dependence, so the ϕ-integral can be done immediately,

$$f(\theta) = \iint r^2\,dr\,d(\cos\theta')\,e^{-ik_f r \cos\theta \cos\theta'} V(r)\phi_\mathbf{k}^{(+)}(r,\theta) \int_0^{2\pi} e^{-ik_f r \sin\theta \sin\theta' \cos\phi}\,d\phi$$

$$= 2\pi \iint r^2\,dr\,d(\cos\theta')\,e^{-ik_f r \cos\theta \cos\theta'} V(r)\phi_\mathbf{k}^{(+)}(r,\theta)\,J_0(k_f r \sin\theta \sin\theta')$$

$$= 2\pi \iint b\,db\,dz\,e^{-ik_f z \cos\theta} V(b,z)\phi_\mathbf{k}^{(+)}(b,z) J_0(k_f b \sin\theta), \tag{2.6}$$

with $b = r\sin\theta'$, $z = r\cos\theta'$. Recalling that, for large $\ell \simeq k_f b$,

$$J_0[(2\ell+1)\sin\theta/2] \simeq P_\ell(\cos\theta), \quad \ell > |\csc\theta|,$$

we have simply obtained a form of the partial-wave expansion of the scattering amplitude, with the sum over ℓ replaced by an integral over impact parameter b. This is not of great interest in itself, but if we backtrack for a moment and consider the high-energy and small-angle limit, where $k_f b \sin\theta \simeq \ell\theta \gg 1$, we can do the ϕ-integral in the stationary-phase approximation. Since the exponent $\ell\theta \cos\phi$ is stationary where $\phi = 0$ and $\phi = \pi$, the

stationary phase rules give

$$\int_0^{2\pi} e^{-i\ell\theta\cos\phi}\,d\phi \simeq \left(\frac{2\pi i}{\ell\theta}\right)^{1/2} e^{-i\ell\theta} + \left(\frac{2\pi i}{-\ell\theta}\right)^{1/2} e^{i\ell\theta}$$

$$= \left(\frac{2\pi}{\ell\theta}\right)^{1/2} [e^{-i(\ell\theta-\pi/4)} + e^{i(\ell\theta-\pi/4)}]$$

$$= 2\pi\left(\frac{2}{\pi\ell\theta}\right)^{1/2} \cos(\ell\theta-\pi/4)$$

$$\simeq 2\pi J_0(\ell\theta), \quad \ell > |\csc\theta|. \tag{2.7}$$

The final result is of course the same as eqn. (2.6), but it illustrates an interesting and important property of $f(\theta)$ in the large-kr limit: if $\ell \gg 1$, the only parts of the scatterer which contribute to $f(\theta)$ are *those in the scattering plane*, the $\phi = 0$ ones [$\exp(-i\ell\theta)$] lying on a Near-side trajectory, and the $\phi = \pi$ ones [$\exp(+i\ell\theta)$] lying on a Far-side trajectory, as indicated in Fig. 8.

The result can even be stated more explicitly in terms of the "edge wave". For large kR, the ℓ-integral of eqn. (2.6) can be done (for $f_N(\theta)$ or $f_F(\theta)$ separately) by steepest descents, and so will come from just a few key ℓ-values. For a strong absorber, as we saw in connection with Fig. 1b, there will be a *single* peripheral ℓ-value for each side-amplitude, which describes the edge wave; the circle of origin of this edge wave is indicated by the vertical longitude-circle of Fig. 8. Very near the forward direction (i.e., within the forward diffraction peak), where $\ell\theta < 1$, the "scattering plane" is not well-defined, and the edge wave originates from this entire vertical circle; at these angles the stationary-phase approximation of eqn. (2.7) fails.

Beyond the diffraction peak, however, where $\ell\theta > 1$, this stationary-phase approximation becomes steadily better. The Near and Far contributions then become definable and arise from ever-more-localized regions of this circle of longitude. The denominator arising from the stationary-phase approximation shows, in fact, that the contributing ϕ-range is $\Delta\phi \simeq (\ell\theta)^{-1/2}$, so as θ increases, these regions shrink to the diametrically opposed limb points of Fig. 8, whose fixed separation determines the (*constant*) period of the Fraunhofer diffraction pattern.

The N/F decomposition is more customarily approached through the partial wave expansion of the scattering amplitude,

$$f(\theta) = \frac{1}{2ik}\sum_\ell (2\ell+1)(e^{2i\delta(\ell)}-1)P_\ell(\cos\theta) \simeq \frac{1}{2ik}\sum_\ell (2\ell+1)e^{2i\delta(\ell)}P_\ell(\cos\theta), \tag{2.8}$$
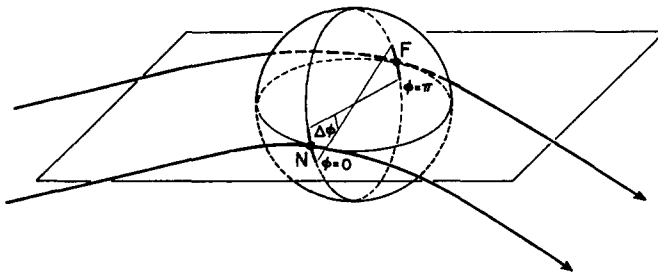

Fig. 8. Schematic indication of the edge waves, which originate in azimuthal-angle intervals of width $\Delta\phi \simeq (\ell\theta)^{-1/2}$, centered at the scattering-plane points $\phi = 0$ and $\phi = \pi$.

dropping the $\delta(1 - \cos\theta)$ term. Substantial insight into many features of the angular distribution is obtainable by writing the "standing wave" $P_\ell(\cos\theta)$ as a sum of two running waves (in θ). For large ℓ this can be done by using

$$P_\ell(\cos\theta) \simeq \left(\frac{2}{\pi\ell\sin\theta}\right)^{1/2} \cos(\ell\theta - \pi/4) = \left(\frac{1}{2\pi\ell\sin\theta}\right)^{1/2} [e^{i(\ell\theta - \pi/4)} + e^{-i(\ell\theta - \pi/4)}]. \quad (2.9)$$

Inserting this into (2.8) splits $f(\theta)$ into two sums, the first being exactly $f_F(\theta)$ and the second $f_N(\theta)$, showing that they are "operationally" distinguished by the sign of the component of the orbital angular momentum normal to the scattering plane: it is parallel to $\mathbf{k}_i \times \mathbf{k}_f$ for the Far side and antiparallel for the Near side.

In fact, if the partial-wave sums are approximated by integrals (valid only if $kR \gg 1$), we have

$$f_{N,F}(\theta) \simeq \frac{1}{ik}\left(\frac{1}{2\pi\sin\theta}\right)^{1/2} \int_0^\infty e^{i[2\delta(\ell) \mp (\ell\theta - \pi/4)]} \ell^{1/2} \, d\ell. \quad (2.10)$$

This important formula shows that $f_N(\theta)$ and $f_F(\theta)$ are nothing more than Fourier transforms of $S(\ell) = \exp[2i\delta(\ell)]$.

In the semiclassical limit, the integrals can be approximated by the stationary-phase method,

$$f_{N,F}(\theta) \simeq \frac{C_{N,F}}{(\sin\theta)^{1/2}} e^{\mp i\ell_0^{N,F}\theta}, \quad (2.11)$$

with

$$C_{N,F} = C_{N,F}(\theta) = \frac{1}{ik}\left(\frac{\ell_0^{N,F}}{2\pi\theta'(\ell_0^{N,F})}\right)^{1/2} e^{2i\delta(\ell_0^{N,F})}, \quad (2.12)$$

with $\ell_0^{N,F}$ determined as a function of θ by the famous deflection function equations,

$$\text{Near:} \quad \theta(\ell_0^N) = 2\frac{d\delta}{d\ell}\bigg|_{\ell = \ell_0^N}, \quad (2.13a)$$

$$\text{Far:} \quad \theta(\ell_0^F) = -2\frac{d\delta}{d\ell}\bigg|_{\ell = \ell_0^F}. \quad (2.13b)$$

We have isolated the $C(\theta)$ factor in (2.11) because for θ in a "deep shadow" region, as is generally the case for high energy heavy ion scattering, $C(\theta)$ is nearly constant because $\ell_0(\theta)$ is nearly constant.

2.2.2. Essential properties
We have reviewed this familiar material in order to list the following important properties of the near and far amplitudes:

2.2.2.1. Exploring the potential.
The deflection function equations (2.13) are equivalent to "trajectory equations" in classical mechanics. The simplest physical situation is that in which there is one saddle point, $\ell_0^N(\theta)$, for the Near side and one, $\ell_0^F(\theta)$, for the Far side. If this is so, the entire N and F amplitudes are given explicitly in terms of these saddles by (2.11), and (2.13), which then provide a 1-to-1 relation between θ and ℓ or θ and $b = \ell/k$. It is in this way that one can think of the angular distribution as "exploring the potential" in the short wavelength limit, since each θ comes from a specific trajectory identified by ℓ or b.

Since b is an asymptotic property of the trajectory, however, it is more informative to

relate it to a distance of closest approach, r_0, as Knoll and Schaeffer[5] point out. The classical distance of closest approach is that distance at which the radial motion stops, so the total energy is just potential plus angular kinetic energy,

$$E = V(r_0) + \frac{\hbar^2 \ell^2}{2\mu r_0^2} = V(r_0) + \frac{\hbar^2 k^2}{2\mu} \frac{b^2}{r_0^2} = V(r_0) + E\left(\frac{b}{r_0}\right)^2, \qquad (2.14)$$

i.e.,

$$b(r_0) = r_0 n(r_0) \equiv r_0 \sqrt{1 - \frac{V(r_0)}{E}}, \qquad (2.15)$$

where $V(r) = V_{\text{Nucl.}}(r) + V_{\text{coul}}(r)$. Thus (2.13) and (2.15) relate θ and r_0—though of course, only to within a wavelength or so. Incidentally, we note that the association of a given penetration distance r_0 with a specific angular region is impossible without the N/F decomposition, since $r_0^N(\theta)$ and $r_0^F(\theta)$ are in general different.

2.2.2.2. Single-trajectory dominance of σ_N and σ_F. The calculation of $\sigma_N(\theta)$ and $\sigma_F(\theta)$ is a simple extension of any optical-model code, and can be done as routinely and automatically as a normal optical-potential calculation. If $f_N(\theta)$ and $f_F(\theta)$ are each dominated by a single trajectory, i.e., by a single (usually complex) ℓ-value, then their calculation by the above generalization of an optical code is equivalent to doing the semiclassical calculation involving the complex ℓ-value, which is (given the speed of modern optical codes) generally considerably more difficult.

It is the edge-dominance or 2-slit nature of most heavy ion angular distributions which *does* make f_N and f_F dominated by a single trajectory each; this not only makes the N/F decomposition useful, but even assigns to each of them the physical significance of a single-slit diffraction pattern.

2.2.2.3. Running waves in angle. Equation (2.11) makes it clear that f_N and f_F are directly related to *running waves* travelling in opposite directions around the nucleus; this in turn directly relates them to Regge poles[7] whenever these are an important feature of the scattering amplitude.

2.2.2.4. Real phase shifts and rainbow shadows. In the special case of scattering by a *real* optical potential (which has little relation to heavy-ion collisions), the phase shifts $\delta(\ell)$ are real, and the equations (2.13) define the usual deflection function, which typically has the shape (at energies above the resonance region, where the potential "pocket" has filled in) shown in Fig. 9, together with its corresponding nuclear phase shift $\delta(\ell)$.

Incidentally, the sign convention employed in such figures is *not* that used in eqn. (2.13). The near amplitude is generated by reflection, generally from a repulsive interaction whose phase shift is negative but increasing with ℓ, making $\theta = 2\delta'(\ell)$ positive, as shown. The far side, if generated by a real potential, must be due to an attractive interaction, whose phase shift is positive but *decreasing* with ℓ, $2\delta'(\ell) < 0$. Since the physical θ is positive, (2.13b) correctly describes a saddle point ℓ_0 at which $\delta'(\ell_0) < 0$, leading via this equation to $\theta > 0$. However, in drawing Fig. 9, one uses the convention $\theta(\ell) = 2\delta'(\ell)$ for *both* N and F, meaning that the positive-angle part of Fig. 8 describes $f_N(\theta)$, while its negative angle part describes $f_F(\theta)$.

The two angular extrema θ_{CR} and θ_{NR}, the Coulomb and nuclear rainbow angles, define
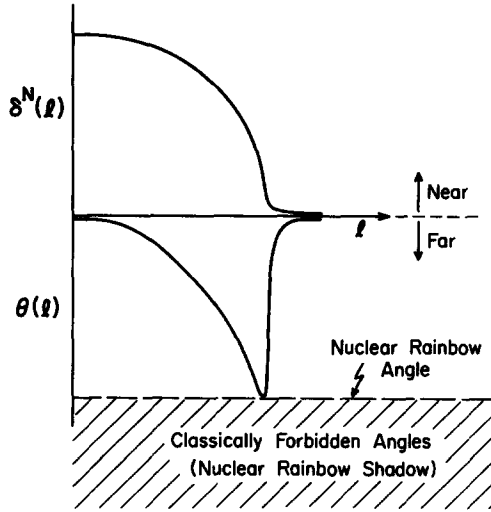
Fig. 9. Schematic indication of the nuclear phase shift and its corresponding deflection function. The "Near" and "Far" labels both apply to the $\theta(\ell)$ graph only.

an angular range,

$$\theta_{\text{NR}} < 0 < \theta_{\text{CR}}, \tag{2.16}$$

within which the equation $2\delta'(\ell) = \theta$ has the real-ℓ solutions indicated by this $\theta(\ell)$ [or $\ell(\theta)$] curve. $\ell(\theta)$ in this real-potential case has *two* solutions for each θ, whose interference produce the familiar "Airy oscillations" on the bright sides of the respective rainbows in the range of eqn. (2.16). However, the equation $2\delta'(\ell) = \theta$ can still be solved for ℓ even outside this range; this is the classically-forbidden angular range, on the *dark* sides of the rainbows. The ℓ-solutions here are complex; for $\theta > \theta_{\text{CR}}$ they lie in the *lower* half of the ℓ-plane, $\text{Im}(\ell) < 0$, and for $\theta < \theta_{\text{NR}}$ they are in the *upper* half of the ℓ-plane. Thus in general they produce amplitudes which *decay in angle* as θ penetrates into the forbidden or shadow region,

$$|f_{\text{N,F}}(\theta)|^2 \simeq e^{-|2\text{Im}\ell_0^{\text{N,F}}|\theta}. \tag{2.17}$$

In general $\text{Im}(\ell_0)$ will itself depend on θ, giving a non-simple decay curve; the classic Airy approximation, e.g., gives $\exp(-\theta^{3/2})$.

The magic feature of nuclei, however, is their thin skin: $a \ll R$. As the argument of eqn. (1.7) suggests, for an "edge scatterer" in this sense, $\ell_0(\theta)$ is *nearly constant* (at least for angles in the deep-shadow region). Hence the important theorem: "3-dimensional leptodermous scatterers have exponential shadows". This appears to be the physical origin of the exponential $\sigma_{\text{N}}(\theta)$ and $\sigma_{\text{F}}(\theta)$ seen so frequently for high-energy scattering by W-S potentials: the running waves $\exp(\pm \ell\theta)$ do their running at a fixed (surface) ℓ-value in shadow regions, leading to *exponential* damping in angle. As we explain more fully below, the *existence* of exponential damping arises from an "orbiting" phenomenon,* while the magnitude of the damping constant, $2\text{Im}(\ell_0)$, is determined by a combination of diffraction

---

* And *not*, e.g., from the fact that the optical potential has an exponential tail!

and refraction, demonstrating how thoroughly refraction and diffraction become inter-mingled at complex ℓ-values.

2.2.2.5. *Absorption and diffractive shadows.* A customary optical shadow is caused by an absorber intercepting the beam, and the illumination which does reach the shadow-region arrives there by diffraction, having been channelled around the absorbing surface by damped running waves. These are thus again described by complex ℓ-values, arising from solving the trajectory equations (2.13) for complex potentials and complex phase shifts. Strong absorption dominates heavy-ion scattering at energies well above the Coulomb barrier; it is this, of course, which makes almost *all* angles except $\theta = 0$ classically forbidden, and is responsible for so many of the near and far angular dependences being simple exponentials. In most heavy-ion cases, $f_N(\theta)$ and $f_F(\theta)$ simply describe the diffraction pattern of a peripheral ℓ-window or "slit" defined by the surface region in which $V(r)$ is changing most rapidly.

2.2.3. The correct mathematics, à la Fuller

The seminal work on the N/F decomposition of elastic amplitudes was done by Fuller,[16] who pointed out that the correct definition of running waves in θ is given by

$$Q_\ell^{(\pm)} = \frac{1}{2}\left[P_\ell(\cos\theta) \pm \frac{2i}{\pi} Q_\ell(\cos\theta) \right] \underset{\ell\to\infty}{\to} \left(\frac{1}{2\pi\ell\sin\theta} \right)^{1/2} \exp\left\{ \pm i\left[\left(\ell+\frac{1}{2}\right)\theta - \pi/4 \right] \right\},$$
(2.18)

which possess the important symmetry

$$Q_\ell^{(-)}[\cos(-\theta)] = Q_\ell^{(+)}[\cos\theta],$$
(2.19)

with $-\theta$ a negative real angle arrived at from θ via a path in the upper half θ-plane. The correct decomposition of P_ℓ into running waves is thus

$$P_\ell(\cos\theta) = Q_\ell^{(-)}(\cos\theta) + Q_\ell^{(+)}(\cos\theta),$$
(2.20)

and, given any amplitude

$$f(\theta) = \frac{1}{2ik}\sum_\ell (2\ell+1)S(\ell)P_\ell(\cos\theta),$$

we have its near and far amplitudes in the form

$$f_{N,F}(\theta) = \frac{1}{2ik}\sum (2\ell+1)S(\ell)Q_\ell^{(\mp)}(\cos\theta),$$
(2.21)

with the properties

$$f(\theta) = f_N(\theta) + f_F(\theta)$$
(2.22)

and

$$f_N(-\theta) = f_F(\theta).$$
(2.23)

Actually, the difficult part of the elastic amplitude is the Coulomb part, which cannot be written in partial-wave form. By a careful consideration of its analytic properties, however, Fuller[16] obtained its N/F separation in closed form. It is his decomposition which has been employed in the computer code used for all calculations shown here, whose f_N and f_F *include* the point-Coulomb contributions. It is this, of course, which makes $f_N(\theta)$ diverge like θ^{-2} for small θ, and also gives $|f_N(\theta)|^2 \gg |f_F(\theta)|^2$ at small θ.

Because $f_N(\theta)$ and $f_F(\theta)$ for the nuclear amplitude are defined only in partial-wave form, we remind the reader that they can only be obtained from the phase shifts. No way is as yet known for decomposing angular distributions in N/F form without going through a partial-wave analysis.

3. A FEW ESSENTIAL PROPERTIES OF HEAVY-ION ANGULAR DISTRIBUTIONS

The essential features which characterize heavy-ion optics at high energy are:
1. $L \simeq kR \gg 1$ (many partial waves); $E > |V|$.
2. Strong Absorption and Weak Refraction
3. Edge scattering or peripheral ℓ-window: $R \gg a$, $ka > 1$.

That is, from an optician's viewpoint, what we are considering here is short wavelength edge-scattering (diffraction) by a strong absorber. All angles beyond $\simeq \theta_{1/4}$ are classically forbidden, and in 3 dimensions all angular distributions fall off exponentially in angle. Put another way, even in the case of scattering by a purely real potential, all angular distributions "shrink toward forward angles" as kR increases. In particular, rainbow angles decrease like $1/E$, so at sufficiently high energies, *all* angles will be "beyond the rainbow", and again one can expect angular distributions which fall exponentially over wide angular ranges.

Such angular distributions depend on a few relatively simple optical phenomena: Diffraction (absorptive shadows, edge diffraction), Refraction (orbiting, Coulomb-prism effect) and Interference. Before attempting to analyze observed angular distributions (which involve all these phenomena simultaneously) in detail in Section 4, we devote the present section to a catalog of these effects separately.

3.1. Exponential shadow tails from peripheral ℓ-windows

Equations (2.8) and (3.10) show that (aside from the $\sin^{-1/2}\theta$ phase-space factor) $f_F(\theta)$ can be written as the Fourier-transform of the S-matrix elements $S(\ell)$,

$$f_F(\theta) \simeq \int_0^\infty [1 - S(\ell)]\, e^{i\ell\theta}\, d\ell. \tag{3.1}$$

Consider the limit of *pure absorption*, customarily defined by the requirement that $S(\ell)$ be real, or $\delta(\ell)$ be pure imaginary. As an example, first, of *non*-exponential shadows, we recall the case of proton–proton scattering in the few GeV range, for which $[1 - S(\ell)]$ is nearly real and is successfully approximated by a Gaussian function of ℓ, $1 - S(\ell) \simeq \exp(-\ell^2/4L^2)$, giving

$$f_F(\theta) \simeq e^{-L^2\theta^2} \simeq e^{-q^2R^2} \tag{3.2a}$$

at small angles, which does *not* carry a phase factor of the form $\exp(iL\theta)$, because this integral does not come from the surface region, i.e., is not an edge-wave. $f_N(\theta)$ thus differs from $f_F(\theta)$ only by a constant (i.e., θ-independent) phase factor, so their sum also gives

$$f(\theta) \simeq e^{-q^2R^2}, \tag{3.2b}$$

the familiar empirical Gaussian dependence. Physically this parametrization says that a proton is "all surface", i.e., its "edge" is so soft that it extends to the center of the proton, and the scattering is not edge-dominated at all. Indeed, doing the integral by steepest descents

yields $\ell_0 = \ell_0(\theta) = 2iL^2\theta$, i.e., the ℓ-value at which the running wave runs is not only imaginary but *increases with* θ, giving the Gaussian angular falloff: the shadow-falloff for a thick-skinned absorber is *faster* than exponential.

At the opposite extreme, we know that a sharp-cutoff ℓ-distribution, $S(\ell) = 0$, $\ell < L = kR$, $S(\ell) = 1$, $\ell > L$, gives the familiar black-disc angular distribution,

$$f(\theta) = iRJ_1(kR\theta)/\theta \simeq -\frac{R}{(2k\sin\theta)^{1/2}}[e^{-i(L\theta-\pi/4)} - e^{i(L\theta-\pi/4)}], \quad L\theta > 1. \tag{3.3}$$

Since $L = kR$ is real, $\sin\theta|f_F(\theta)|^2$ is constant: taking the skin thickness of the absorber to zero makes the shadow-falloff distance infinite (i.e., *uniform* illumination of shadows).

Finally, recalling that the Fourier-transform of an exponential is a pole, it is clear that if we wish exponential shadows, we must start from an $S(\ell)$ which has poles (at complex ℓ). The most familiar such parametrization is the Fermi-function shape employed by Frahn,[1] Rowley and Marty[6] and others,[9]

$$1 - S(\ell) = \frac{1}{1 + \exp[(\ell - L)/\Delta]}, \tag{3.4}$$

which has poles at $\ell = L \pm i\pi n\Delta$. Doing the integral in (3.1) by contours, the arguments employed in connection with (1.7) yield, in the $\Delta \ll L$ limit,

$$f_{F,N}(\theta) \simeq e^{\pm i(L \pm i\pi\Delta)\theta} = e^{-\pi\Delta\theta}e^{\pm iL\theta}, \quad \theta > 0, \tag{3.5}$$

which indeed has an exponential shadow tail [and reduces, in the $\Delta \to 0$ limit, to (3.3)]. As pointed out in connection with eqn. (1.8), this is really just an exponential 1-slit diffraction pattern, whose envelope at both positive and negative angles is $\exp(-\pi\Delta|\theta|)$.

Thus our conclusion is that exponential shadows are cast by spherical absorbers whose surface thickness is small compared to their radius, but not zero. Note, incidentally, that for absorbers the shadows "begin" at $\theta = 0$: the entire (forward-peaked) angular distribution (i.e., diffraction pattern) is classically forbidden.

3.2. Babinet symmetry for pure absorbers

The pure-absorber limit, $\text{Im}[S(\ell)] = 0$, is an important one for heavy ions, whose optical potentials *are* strongly absorptive. As an approximation to it (not exact because even an imaginary potential reflects), Fig. 10a shows the angular distribution for a purely imaginary *potential*, with neither nuclear nor Coulomb refraction. Its obvious feature is that $\sigma_N(\theta)$ and $\sigma_F(\theta)$ are essentially identical. This is in fact a theorem, which follows immediately from (2.18) and (2.21), if $S(\ell)$ is real for real ℓ:

Theorem

$$S(\ell)^* = S(\ell) \Rightarrow f_F(\theta) = -f_N^*(\theta), \tag{3.6}$$

so that

$$\sigma_N(\theta) = \sigma_F(\theta), \tag{3.7}$$

and in general the N/F interference minima are zeros, as in the black-disc example.

The theorem also has a useful corollary: If $\ell_0^N(\theta)$ is the (complex) solution of the trajectory equation (2.13a) for a pure absorber, the corresponding Far-side solution for the same angle is its complex conjugate, $\ell_0^F(\theta) = \ell_0^{N*}(\theta)$.

This follows directly from the assumption that $\delta(\ell)$ is an analytic function, and is pure

1/4-THETA- 0.0, K*AI- 5.23, THETA(NR)--180. AT L(NR)-190

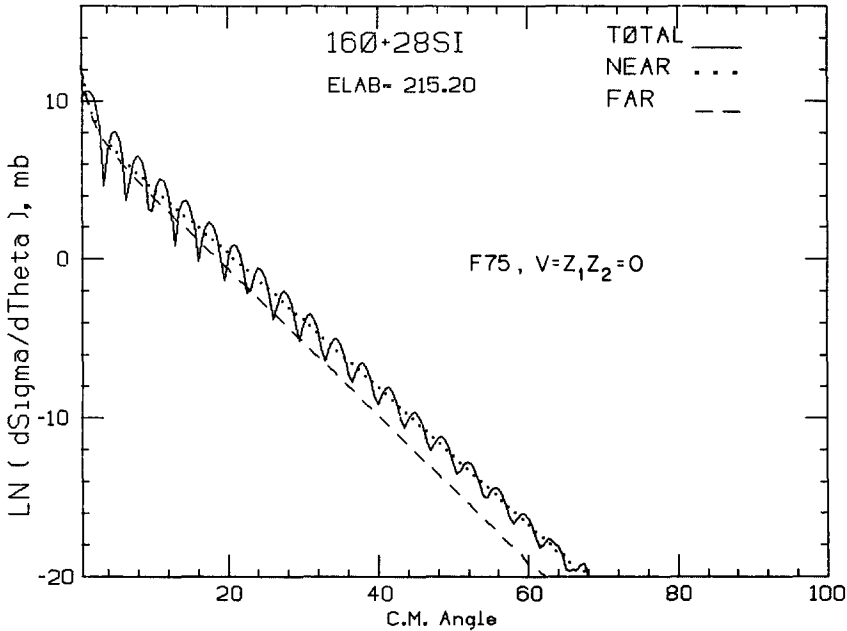V- 0.00, R- 5.89, A-0.640, VI- 42.00, RI- 5.89, AI-0.640

Fig. 10a. Scattering by a purely imaginary potential, with neither nuclear nor Coulomb refraction.

imaginary at real ℓ for a pure absorber. If $2\delta'(\ell_0^N) = \theta = $ real, this implies that $-2\delta'^*(\ell_0^{N*}) = \theta$, but this is just (2.13b), q.e.d.

3.3. The single-slit edge wave of an absorber

Figure 10a shows only the $\theta > 0$ parts of the above diffraction pattern, but the properties

$$-f_N^*(\theta) = f_F(\theta) = f_N(-\theta), \tag{3.8}$$

valid for a pure absorber, show that $\sigma_N(\theta)$ and $\sigma_F(\theta)$ are actually symmetric about $\theta = 0$, as Fig. 10b illustrates. We call this a Babinet symmetry because it is a simple example of the Babinet principle for the diffraction patterns of absorbers. That is, considering one limb of the absorber alone,* Babinet guarantees that the *scattered* (diffracted) wave generated by a beam intercepted by the absorber is the same whether the absorber is to the right or left of the edge position, i.e., its diffraction pattern must be symmetric about $\theta = 0$.

The symmetry theorem (3.7) is true for any pure absorber, but it takes on very concrete physical meaning for an edge-wave diffraction pattern. Consider doing the ℓ-integral of (3.1),

$$f_F(\theta) \simeq \int_0^\infty [1 - S(\ell)]\, e^{i\ell\theta}\, d\ell,$$

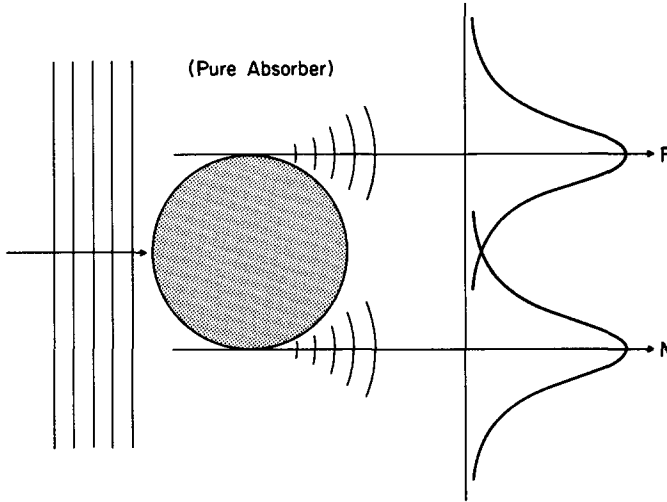* Which we are free to do if $R \gg a$.

Fig. 10b. Schematic indication of the N and F single-slit diffraction patterns, which are identical for a pure absorber.

by steepest descents. For an edge-scatterer, in which $1 - S(\ell)$ is nearly constant throughout the internal region, any internal ℓ can only contribute to straight-ahead $(\theta = 0)$ propagation (a plane-parallel slab of glass produces no deflection). Hence the *only* ℓ-region which can produce deflected rays is the peripheral or surface region, where $S(\ell)$ *does* change with ℓ and so can counteract the oscillations of the exponential factor. This is the reason such a scatterer generates its deflected rays primarily from its edge region (ℓ-window), with an expanding scattered-wave packet emerging from each "slit", as illustrated in Fig. 1a. If the scatterer is a pure absorber ($[1 - S(\ell)]$real), the symmetry theorem (3.7) guarantees that these identical peripheral diffraction-fans will each be *symmetric* about $\theta = 0$; their exact angular shape will depend on $S(\ell)$, but this symmetry is guaranteed for any surface-shape of $S(\ell)$.

Incidentally, eqn. (3.1) provides a simple explanation of the fact that the scattering amplitude of a spherical absorber is edge-dominated, while that of a spherical refractor is not. The point is simply that $f(\ell) = [1 - S(\ell)]$ "saturates" at $f = 1$ for $\ell < L$ in the strong absorption case, and so contributes nothing to deflected rays $(\theta \neq 0)$ from its internal, $\ell < L$, region. For a spherical refractor, however, which is simply a spherical "lens", the phase shift (proportional to the chord distance $[R^2 - b^2]^{1/2}$ at impact parameter $b = \ell/k$, in Glauber approximation) has a shape like that of Fig. 8. It varies with ℓ everywhere except at the very center, so all parts of its interior contribute deflected rays, i.e., its amplitude is not edge-dominated.*

3.4. Slopes of exponential shadows: Orbiting at complex ℓ

The above arguments indicate that a thin-skinned absorber will produce identical exponential diffraction patterns for $\sigma_N(\theta)$ and $\sigma_F(\theta)$, both symmetric about $\theta = 0$. What happens if nuclear refraction is added? Figure 11 shows the cross-sections for the absorber

---

* For further details on lenses viewed as phase-shifters, see Appendix A.

1/4-THETA- 0.0, K*AI- 5.23, THETA(NR)--180. AT L(NR)-190

V-100.00, R- 5.89, A-0.640, VI- 42.00, RI- 5.89, AI-0.640

160+28SI

ELAB- 215.20

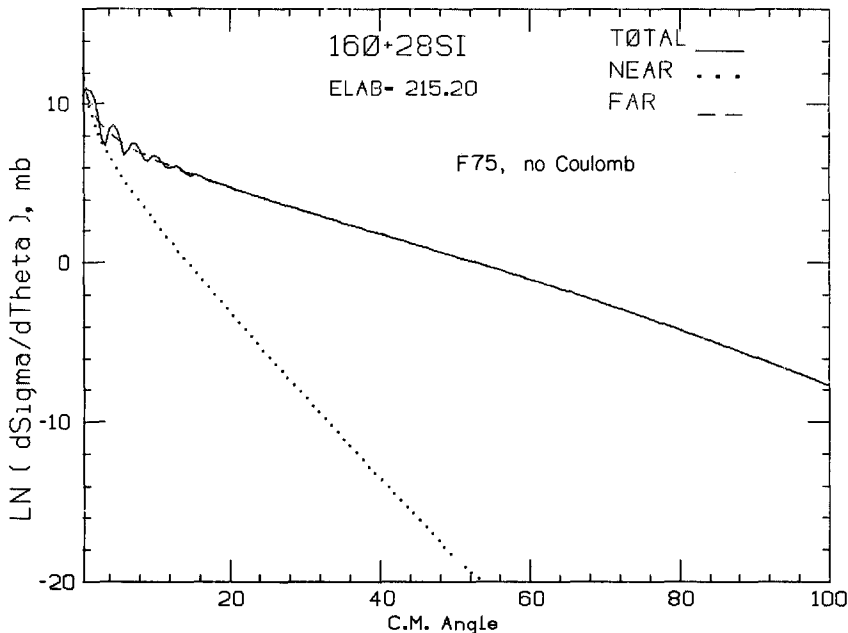TØTAL ___
NEAR ...
FAR __ __

F75, no Coulomb

Fig. 11. Repeat of Fig. 9, with nuclear refraction ($V = W = 42\,\text{MeV}$) added, thus increasing N-slope and decreasing F-slope.

of Fig. 10a ($W = 42\,\text{MeV}$), but with an equal amount of refraction ($V = 42\,\text{MeV}$) added, with the same geometry (and no Coulomb potential). The result is to enhance the far side over the near side (as is certainly to be expected, for an attractive potential), *by changing their slopes*. The fact that the effect of V is simply to change the slopes can be implied immediately from the fact that, in the absence of the Coulomb potential, the system is entirely symmetric in N and F at $\theta = 0$, so that, whatever potential is present, we must have $\sigma_N(0) = \sigma_F(0)$.* That is, adding V can do nothing but "pivot" the $\sigma_N(\theta)$ and $\sigma_F(\theta)$ lines about the same $\theta = 0$ point.

To avoid misinterpretation, we emphasize that this is a change in the *symmetry* of each single-slit diffraction pattern, not a shift in its central direction (such a shift *is* accomplished by the Coulomb field); the maximum of each single-slit pattern is still at $\theta = 0$, as indicated schematically in Fig. 12. Optically speaking, this alteration of the symmetry of a diffraction pattern has been accomplished by adding refractive material *internally*, within a diffraction slit (as opposed to the use of an external focussing lens), in a situation where the width of the slit is comparable to the wavelength of the radiation. It is consequently quite esoteric from the optics point of view, and we know of no simple optical analog.

The full details of the way in which V and W affect the N and F shadow slopes is quite complex and will be published elsewhere. We give here only a brief summary of the results.

---

* Actually $Q_\ell^{(\pm)} (\cos\theta)$ are logarithmically singular at $\theta = 0$, but the singularity is so mild that it has no visible effect beyond $1°$.
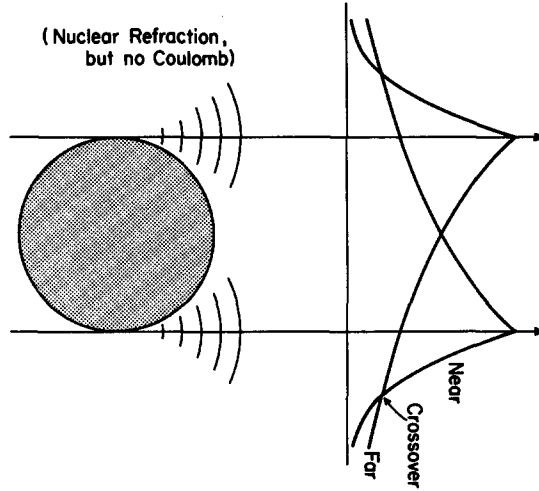
Fig. 12. Repeat of Fig. 10, with nuclear refraction added. Note asymmetry of the single-slit patterns. The "right-hand half" of each pattern is shown in Fig. 11.

The near-side amplitude can be thought of as arising from reflections off the front of the potential, at distances of closest approach, r_0, which in general change with a θ (or impact parameter b) and are determined by the trajectory equation (2.13a). At energies below the Coulomb barrier, $r_0(\theta)$ will be in the "external" region, and will have its minimum value at $\ell = b = 0$ as indicated in Fig. 13, where $\theta = \pi$; i.e., for $E < E_B$ all angles are classically allowed. Since $\ell = 0$, this important value of r_0 is determined by the condition

$$V[r_0(\pi)] = E, \tag{3.9}$$

where $V(r)$ includes both the nuclear and Coulomb potentials. If $V(r)$ is real and $E < E_B$,
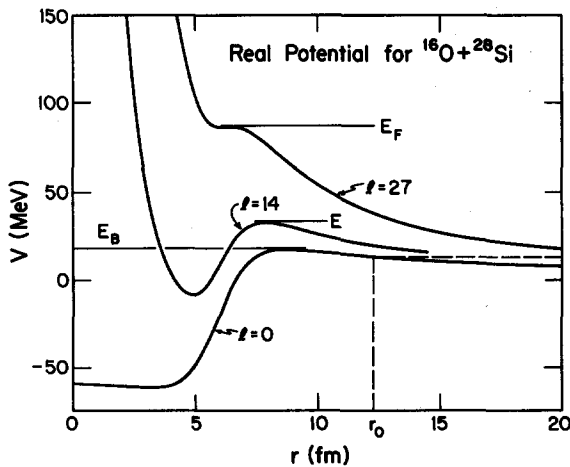

Fig. 13. A typical $V_\ell(r)$, for 3 ℓ-values. E_B is the Coulomb barrier energy, and E_F is the "Fill-in" energy, at which the potential pocket disappears with increasing ℓ; it occurs in this case at $\ell = 27$.

$r_0(\pi)$ will be real. It is complex if $E > E_B$, or at every energy if the nuclear potential is complex. Its importance derives from the fact that $r_0(\theta)$ has a minimum at $\theta = \pi$,

$$\frac{dr_0}{d\theta} = \frac{d\ell}{d\theta} = 0 \quad \text{at} \quad \theta = \pi. \tag{3.10}$$

The importance of this, in turn, is that $f_N(\theta) \simeq \exp[-i\ell_0(\theta)]$ will in general not be exponential in θ if $\ell_0(\theta) = kr_0n(r_0)$ is changing with θ. Equation (3.10) guarantees that it does *not* change with θ at large angles, which are deep within the Coulomb-shadow region at high energy. (The Coulomb-rainbow angle decreases below π as E increases through E_B and continues decreasing like $1/E$.) In fact, the classic work of Knoll and Schaeffer[5] indicates that $\ell_0(\theta)$ moves very slowly with θ for most angles beyond the Coulomb rainbow angle, which is close to the quarter-point angle. This implies that, once $d\sigma/d\sigma_R$ begins to drop below unity, the descent of $d\sigma/d\theta$ is nearly exponential, with a slope determined by the r_0 obtained from (3.9). This slope is given by

$$2\text{Im}\ell_0 = 2\text{Im}(kb_0) = 2k\text{Im}[r_0 n(r_0)], \tag{3.10}$$

where

$$n(r_0) = [1 - V(r_0)/E]^{1/2}. \tag{3.11}$$

If we neglect the Coulomb potential, and assume a $W - S$ nuclear potential, this gives the simple result* for the near side,

$$\text{Im}r_0^N(\pi) = a\{\pi - \tan^{-1}[W/(V + E_{cm})]\} \qquad (W > 0, \quad V > 0)$$
$$\text{(near side, equal geometry)} \quad (3.12)$$

showing that, as a function of W, the slope of the near-side shadow is a *maximum* when $W = 0$: increasing W actually makes $\sigma_N(\theta)$ decay *less* steeply, as Knoll and Schaeffer also noted. Increasing E (or V), on the other hand, steepens the near-side slope by increasing $|\text{Im}(r_0)|$ toward its maximum value of πa. This is the nearest pole of the Woods–Saxon pole in the lower r_0-plane, to which r_0 is clearly expected to tend as $E \to \infty$, according to (3.9).

What about the slope of the far side? Again we must seek an r_0 at which $dr_0/d\theta = 0$, and this time it is given by the "orbiting" condition that the radial kinetic energy vanish exactly where $V(r_0) + \hbar^2\ell_0^2/2\mu r_0^2$ has a maximum, as is also indicated in Fig. 13. That is, $\ell_0 = \ell_0(\theta)$, so as θ changes, ℓ_0 changes, and when ℓ_0 satisfies

$$V(r_0) + \frac{\hbar^2\ell_0^2}{2\mu r_0^2} = E, \tag{3.13a}$$

$$\text{(orbiting)}$$

where

$$\frac{d}{dr}\left[V(r) + \frac{\hbar^2\ell_0^2}{2\mu r^2}\right] = 0, \tag{3.13b}$$

this defines the $\ell_0 \equiv \ell_B = \ell_B(E)$ for which E is tangent to the top of the barrier — as shown for $\ell = 14$ in Fig. 13. This is precisely the "orbiting" condition, and (for this E), ℓ_B is the ℓ-value at which the WKB deflection function $\theta(\ell)$ has a logarithmic singularity, $\theta(\ell) \simeq \ln(\ell - \ell_B)$. Hence $d\theta/d\ell \to \infty$ and $d\theta/dr_0 \to \infty$ at $\ell = \ell_B$, or equivalently $d\ell/d\theta = dr_0/d\theta = 0$ at $\ell = \ell_B$: the (far side) $\ell(\theta)$ moves very slowly as a function of θ when it is close

---

* Neglecting the Coulomb potential of course loses the Coulomb-rainbow-phenomenon: there are no classically-allowed positive angles in this case, even if $W = 0$.

to ℓ_B—which is exactly the condition necessary to give $\exp(i\ell\theta)$ an exponential dependence on θ. This can only happen, at real r_0, if $V(r)$ is real and $E < E_F$ (Fig. 13), where E_F is the energy* at which the potential $V_\ell(r)$ loses its pocket with increasing ℓ. r_0 becomes complex (a) if $E > E_F$ when $W = 0$, or (b) at *any* energy, if $W \neq 0$, but it is still determined by the orbiting conditions (3.13).

Again neglecting the Coulomb potential, assuming a W-S nuclear potential, and neglecting terms of order a/R, $\mathrm{Im}r_0$ is found to be given by

$$\cos^2[\mathrm{Im}(r_0^F/2a)] = \tfrac{1}{2}(1+\gamma) - \tfrac{1}{2}[(1+\gamma)^2 - 4\gamma\cos^2\phi/2]^{1/2},$$

where

$$\gamma = \frac{1}{8}\frac{(V^2 + W^2)^{1/2}}{E_{cm}}\frac{R}{a},$$

$$\phi = \tan^{-1}(W/V), \qquad \text{(Far side, equal geometry)} \quad (3.14)$$

and this root of the quadratic must be used when $W \neq 0$. The $E \to \infty$ limit gives $\cos[\mathrm{Im}r_0^F/a] = 0$, implying $\mathrm{Im}r_0^F = +\pi a$, again because $r_0^F \to R + i\pi a$, the first upper-plane pole of the W-S potential, as demanded by (3.11). Also, increasing V decreases $\mathrm{Im}r_0^F$ (though not obviously), thus *decreasing* the slope of the Far side, opposite to the effect of V on the Near side.

We remark in passing that adding *any* attractive real potential to a pure absorber will make the N-slope steeper than the F-slope. The effect is *not* due to the fact that the Coulomb rainbow is "wider in ℓ" than the nuclear rainbow, as often conjectured. As Fig. 11 indicates, it occurs when there is no Coulomb rainbow at all.

In summary, the qualitative effect of adding an attractive refractor to the peripheral ℓ-windows of an absorber is to pull the N-diffraction pattern *toward* the forward direction ($\theta = 0$) and the F-pattern further *away* from $\theta = 0$ (attractive forces *aid* Far-side diffraction), in agreement with one's intuition. The remarkable aspect of the example shown in Fig. 11 is that it is accomplished by leaving both $\sigma_N(\theta)$ and $\sigma_F(\theta)$ as *exponential* curves, merely changing their slopes appropriately. This is, in fact, a result of the use of equal geometries for the real and imaginary parts of the potential; a close examination of $\sigma_N(\theta)$ for the E 18 potential of Fig. 6 shows it to have *two* slopes, in different angular regions. They are related to the different values of a for $V(r)$ and $W(r)$, as we explain below.

3.5. External refractors: The Coulomb prism

The final topic in this section is the effect of the Coulomb force on the single-slit diffraction patterns of the nuclear absorber, which is very different from the effect of the nuclear refraction. The reason is simply that the Coulomb field is a very "soft" refractor, i.e., its phase shift $\sigma(\ell)$ has no singularities near $\ell \simeq kR$. With a Coulomb field present, the total phase shift is, as usual, $\delta(\ell) + \sigma(\ell)$, with $\delta(\ell)$ the "nuclear" phase shift calculated by an optical code. The trajectory equation is then

$$\mp\theta_{F,N} = 2\frac{d}{d\ell}[\delta(\ell) + \sigma(\ell)] = 2\delta'(\ell_0) + \theta_c(\ell_0), \qquad (3.15)$$

where $\theta_c(\ell)$ is the Coulomb deflection angle at the (generally complex) $\ell = \ell_0$. However,

---

* It is also the energy at which the *nuclear* rainbow angle becomes less negative than $-\pi$, and is given roughly by[5] $E_F = \tfrac{1}{2}V_{coul}(R) + (a/8R)V$.

because, as we have seen, $\ell_0 \simeq k(R \pm i\beta a)$, with $\beta < \pi$, ℓ_0 differs from kR by less than πka. This is typically less than 10 units in ℓ, and since $\theta_c(\ell)$ changes little over this range, at high energies, we may approximate it by its value at $\ell \simeq kR$, which in the high-energy limit is

$$\theta_c(kR) = 2\tan^{-1}(\eta/kR) \simeq 2\eta/kR = \frac{V_c(R)}{E_{cm}} \equiv \theta_{1/4}, \qquad (3.16)$$

the high-energy approximation to the customary quarter-point angle.*

Approximating $\theta_c(\ell)$ as constant across the ℓ-window is optically equivalent to approximating the curved Coulomb "lens" by a flat "prism" in this ℓ-range, and gives the trajectory equations

$$\theta_F + \theta_{1/4} = 2\delta'(\ell_F), \qquad \theta_N - \theta_{1/4} = 2\delta'(\ell_N), \qquad (3.17)$$

which are of exactly the same form as the original equations, except for a constant shift by $\theta_{1/4}$. Thus if

$$f_N^0(\theta) \simeq e^{-\beta_N ka\theta}\, e^{-ikR\theta}, \qquad f_F^0(\theta) \simeq e^{-\beta_F ka\theta}\, e^{+ikR\theta} \qquad (3.18)$$

without the Coulomb potential, they become

$$f_N(\theta) \simeq e^{-\beta_N ka(\theta - \theta_{1/4})}\, e^{-ikR(\theta - \theta_{1/4})},$$
$$f_F(\theta) \simeq e^{-\beta_F ka(\theta + \theta_{1/4})}\, e^{ikR(\theta + \theta_{1/4})} \qquad (3.19)$$

with the Coulomb potential. β_N and β_F can be estimated from eqns. (3.12) and (3.14) as

$$\beta_N = \mathrm{Im}(r_0^N/a), \qquad \beta_F = \mathrm{Im}(r_0^F/a). \qquad (3.20)$$

Unlike the "internal" nuclear refractor, which is singular, the "Coulomb prism" does *not* change the slopes of $\sigma_N(\theta)$ and $\sigma_F(\theta)$, but merely *shifts* them in angle, to the right (larger θ) for σ_N and to the left (smaller positive θ) for σ_F, exactly as seen in Fig. 3c, and in accord with one's intuition ($\sigma_N(\theta)$ shifted away from $\theta = 0$, $\sigma_F(\theta)$ shifted toward $\theta = 0$ by a diverging lens.)

Actually, shifting a straight line (like $\sigma_{N,F}(\theta)$ on a logarithmic plot) horizontally is equivalent to shifting it vertically, and (3.19) can also be interpreted as a vertical shift,

$$\ln\frac{\sigma_N}{\sigma_F} = 2(\beta_N + \beta_F)ka\theta_{1/4}. \qquad (3.21)$$

This is in fact a preferable interpretation, for, although the maximum in the $\sigma_F(\theta)$ single-slit diffraction pattern can correctly be thought of as being shifted "out of sight" at negative angles, $\sigma_N(\theta)$ has the θ^{-2} Coulomb divergence at $\theta = 0$ which keeps its "maximum" fixed at $\theta = 0$. For $\theta \gtrsim \frac{1}{2}\theta_{1/4}$, $\sigma_N(\theta)$ is dominated by the point-Coulomb amplitude and cannot be given this "shift" interpretation, but for larger angles, (3.19) accurately reflects the effect of the Coulomb potential.

Figure 14 attempts to represent this schematically. The figure at the right shows $\sigma_N(\theta)$ and $\sigma_F(\theta)$ for a *pure absorber plus Coulomb*: σ_N is shifted up relative to σ_F by the factor represented by eqn. (3.19), but they remain parallel—i.e., the single-slit pattern is left symmetric by the Coulomb shift. Adding nuclear refraction makes the single-slit pattern asymmetric by making the slope of $\sigma_N(\theta)$ greater and that of $\sigma_F(\theta)$ less, thus producing a Fraunhofer cross over, as shown in the center part of Fig. 14.

---

*This value of $\theta_{1/4}$ has been included in the figure legends for convenience, as well as the nuclear rainbow angle and (ka_I). A more accurate estimate would replace k by $kn(R)$.
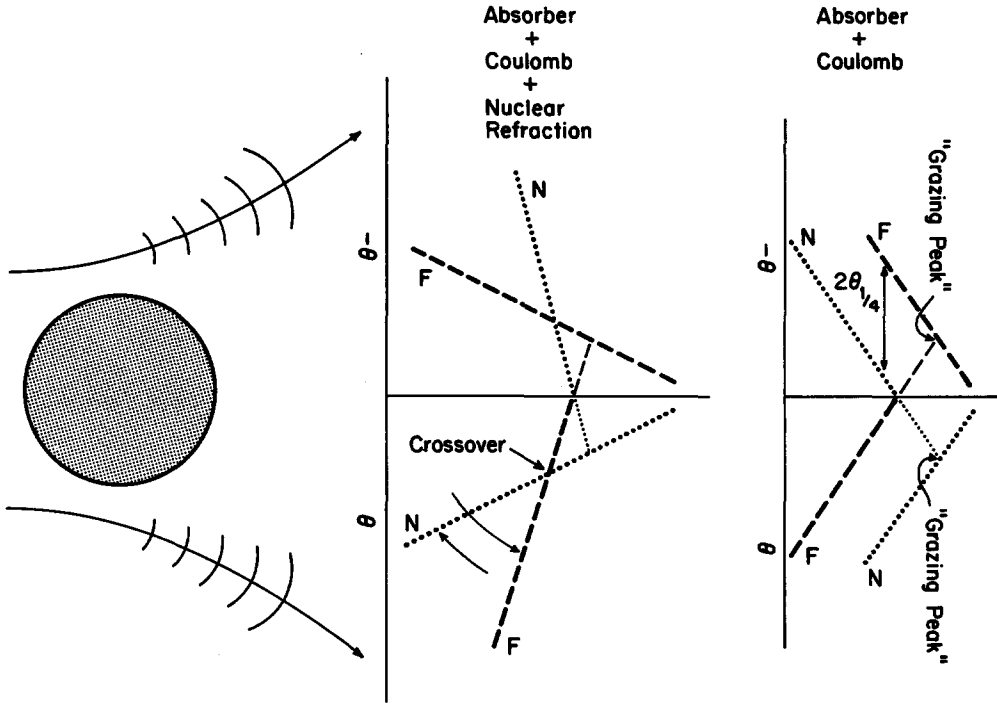
Fig. 14. Schematic representation of $\sigma_N(\theta)$ and $\sigma_F(\theta)$. The right-hand figure shows symmetric but shifted single-slit or "grazing-peak" patterns which occur (as in Fig. 3c) if $V = 0$. The center figure indicates how the addition of V makes the single-slit patterns asymmetric by increasing the slope of σ_N and decreasing that of σ_F (i.e., each N or F combination "pivots" about the crossing-point at $\theta = 0$), thus producing the Fraunhofer crossover.

4. PRACTICAL APPLICATIONS AND EXAMPLES

4.1. Summary of Sections 2 and 3

The pieces of the puzzle are at last all in hand. To summarize the results of the previous two sections, the scattering amplitude for a typical (strongly absorbing) heavy-ion optical potential can be written as a sum of two single-slit (peripheral ℓ-window) diffraction patterns, as suggested by Fig. 14. The angles of the centers of these patterns are "flared out" by the diverging-lens effect of the Coulomb field, and each pattern is exponential about its center, but made *asymmetric* (in the manner indicated by Fig. 12), by the nuclear refraction. The parts of these single-slit patterns seen at positive angles are the Near-side and Far-side amplitude, and the Near side is the steeper of the two. At low energies (roughly $E < |V|$) the Near side, enhanced by Coulomb repulsion, dominates over the Far, and $d\sigma/d\Omega$ shows no Fraunhofer diffraction oscillations, i.e., no N/F interference. For $E > |V|$, the Near side is still dominant at small angles (large impact parameters), but at larger angles the trajectories penetrate the nucleus and the smaller slope of $\sigma_F(\theta)$ (caused by nuclear refraction) causes it to cross through $\sigma_N(\theta)$, producing a *localized* range of N/F Fraunhofer oscillations, beyond which it is dominated by the "structureless falloff" of the exponential decay of $\sigma_F(\theta)$. In the equal-geometry case, $f_N(\theta)$ and $f_F(\theta)$ are well approximated by the very simple expressions of eqns. (3.19) and (3.20).

Put in simplest terms, the Near side and Far side cross-sections $\sigma_N(\theta)$ and $\sigma_F(\theta)$ describe, for a strong absorber, the "outside" and "inside" edges of the peripheral single-slit diffraction pattern. Both are nearly straight lines on a logarithmic plot, with relative *slopes* (steeper for N) determined by the real part of the nuclear potential, and relative *normalization* determined by the Coulomb potential. If $E > |V| > E_{\text{barrier}}$ they cross at some finite angle, producing localized Fraunhofer oscillations of peak-to-peak period $\Delta\theta = \pi/L$.

Incidentally, three other types of interference patterns are also sometimes observed (see examples below):

1. Near–Near Interference. These are the familiar forward-angle oscillations (best seen in $d\sigma/d\sigma_R$ for $\theta < \theta_{1/4}$), describable as either Fresnel diffraction (if absorption is strong) or the "Airy maxima" of the bright side of the Coulomb rainbow (if absorption is weak).

2. Far–Far Interference. The "Airy maxima" of the bright side of the nuclear rainbow.

3. N/F Interference Near 180°. By symmetry, scattering at $\theta = 180°$ must equal that at $\theta = -180°$, meaning $\sigma_N(\theta)$ and $\sigma_F(\theta)$ must be equal at back angles. Depending on their slopes there, they may produce a sequence of oscillations known as the (backward) glory effect.

With this background in hand, we turn to an analysis of interesting examples from recent heavy-ion experiments.

4.2. Influence of nuclear refraction

Figure 15c shows the N/F decomposition for an optical potential which fits recent ^{9}Be and ^{16}O data of Fulmer *et al.*[17] The radius of its imaginary part is larger (by about $2a$) than

1/4-THETA- 5.5, K·AI- 4.96, THETA(NR)--177. AT L(NR)- 55
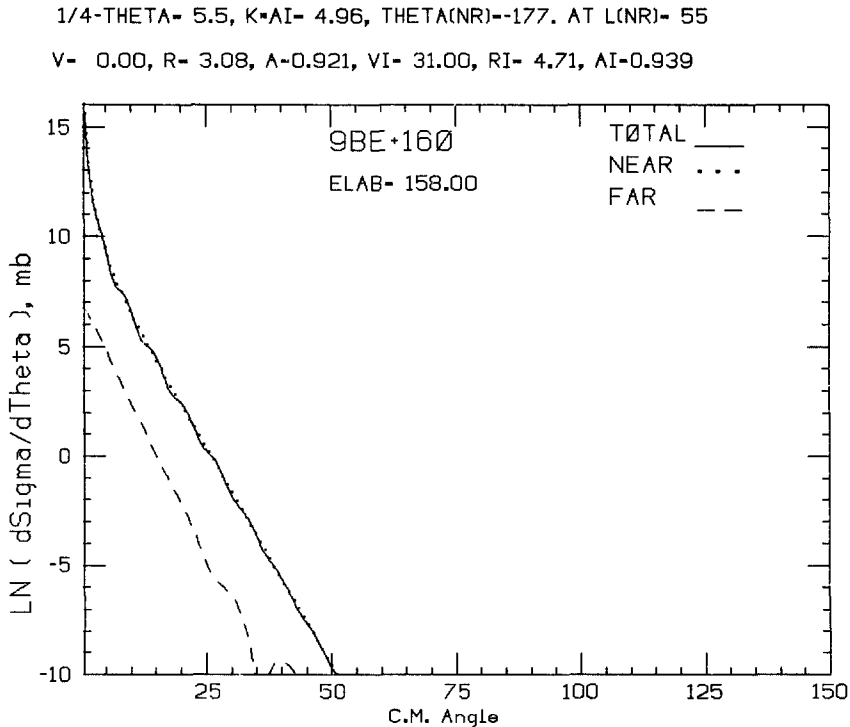
V- 0.00, R- 3.08, A-0.921, VI- 31.00, RI- 4.71, AI-0.939

Fig. 15a. ^{9}Be + ^{16}O, with $V = 0$; no crossover.

1/4-THETA- 5.5, K=AI- 4.96, THETA(NR)--179. AT L(NR)-131
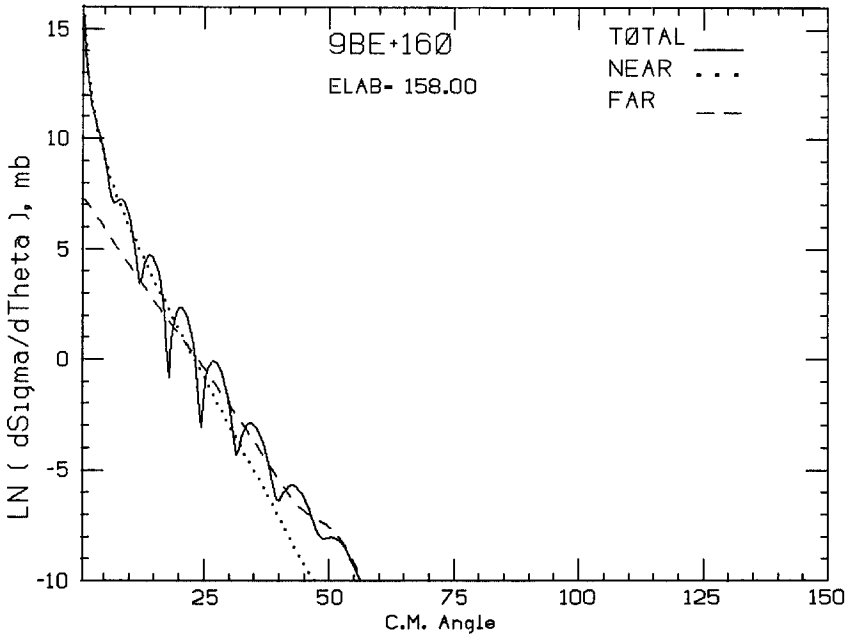V-100.00, R- 3.08, A-0.921, VI- 31.00, RI- 4.71, AI-0.939

Fig. 15b. Same as 15a, with $V = 100$ MeV; slow crossover.

1/4-THETA- 5.5, K=AI- 4.96, THETA(NR)--179. AT L(NR)-131
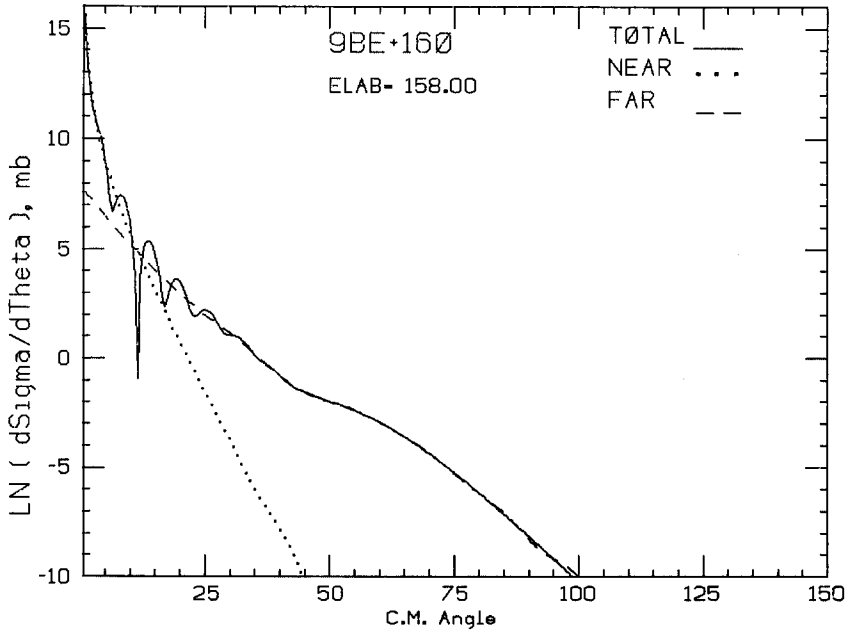V-184.80, R- 3.08, A-0.921, VI- 31.00, RI- 4.71, AI-0.939

Fig. 15c. Same as 15a, with $V = 184.8$, to fit the data of Satchler *et al.*, Ref. 17. Note the "quicker" crossover and the hint of a nuclear-rainbow "Airy maximum" at 60°.

1/4-THETA- 5.5, K*AI- 4.96, THETA(NR)--209. AT L(NR)- 27
V-400.00, R- 3.08, A-0.921, VI- 31.00, RI- 4.71, AI-0.939

9BE+16Ø
ELAB- 158.00

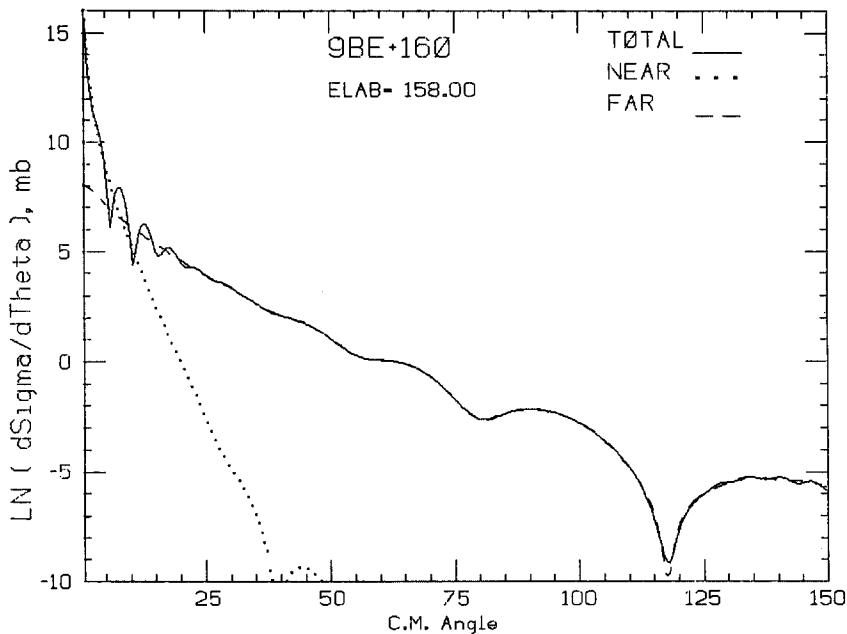TØTAL ____
NEAR . . .
FAR   _ _

Fig. 15d. Same as 15a, with V artificially increased to 400 MeV. Note the well-developed nuclear rainbow, whose rainbow angle has moved beyond $-180°$.

1/4-THETA- 5.5, K*AI- 4.96, THETA(NR)--177. AT L(NR)- 55
V- 0.00, R- 3.08, A-0.921, VI- 31.00, RI- 4.71, AI-0.939

9BE+16Ø·
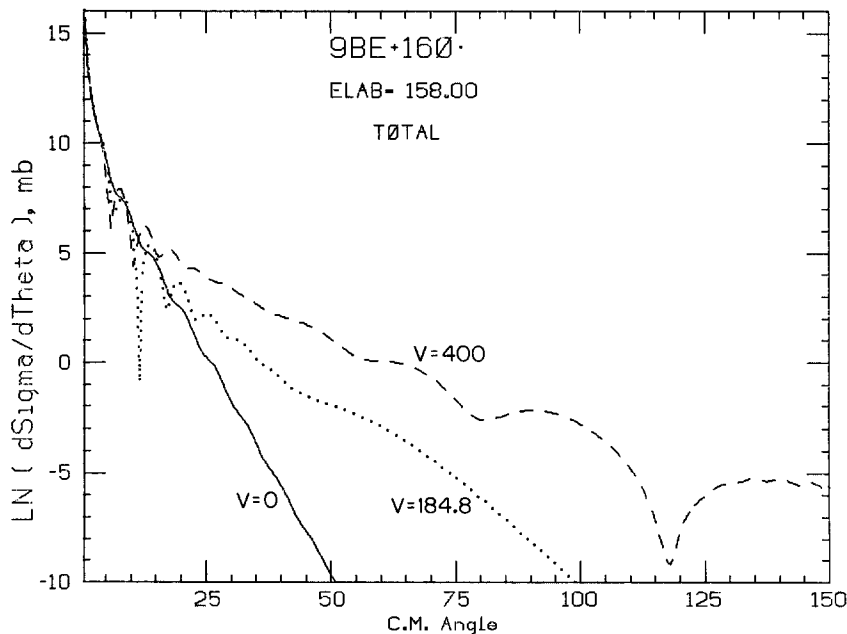ELAB- 158.00
TØTAL

V=400

V=0   V=184.8

Fig. 15e. Repeat of cross sections for Figs. 15a, c and d. N.B.: In this figure, as well as in all others which compare 3 Near, 3 Far or 3 Total cross-sections, the top legend refers to *solid* curve only.

that of its real potential, but the real potential is 6 times deeper (184/31) than the imaginary one, producing a localized N/F crossover around 12°. Figure 15a shows how the angular distribution is changed by removing V altogether: it of course becomes Near-dominated, $\sigma_N(\theta)$ and $\sigma_F(\theta)$ are parallel, and there are only very weak Fraunhofer oscillations. Increasing V to 100 MeV (about half that needed to fit the data) with the original geometry (Fig. 15b) causes $\sigma_F(\theta)$ to "pivot" about its $\theta = 0$ value (which is very nearly independent of V), *decreasing* its slope as predicted above.* The slope of $\sigma_N(\theta)$ *increases* (though not by nearly as much), producing a "slow" crossover whose oscillations extend from 10° to 40°. Finally, increasing V to 400 MeV (Fig. 15d) causes $\sigma_N(\theta)$ and $\sigma_F(\theta)$ to pivot farther still, but also brings in a new refractive phenomenon—the nuclear rainbow (the rainbow angle is $-209°$ in this case). This very strong refraction is able to channel waves through the center of the nucleus, and the far side is, in this case, *not* edge-dominated. Rather, low-ℓ contributions to $f_F(\theta)$ become strong enough to interfere with the edge wave, producing the very broad ($\simeq 40°$) Far-side oscillations—i.e., the Far-Far interference of the nuclear rainbow, which we examine more closely in the next section. This evolution of the Fraunhofer pattern with increasing V is recapitulated in Fig. 15e.

In summary, these examples show how the difference between the N and F slopes is increased by increasing the depth of the real potential, thus causing the number of oscillations in the Fraunhofer crossover to decrease.

4.3. Nuclear rainbows?

There has been considerable discussion recently[18–20] of the possibility that elastic $^{12}C + ^{12}C$ scattering at $E_L > 300$ MeV may show evidence for a nuclear rainbow. The practical importance of such an occurrence is perhaps best seen in the context of the familiar "$V_0 a^2$ ambiguity" of the real part of the optical potential. Some years back, elastic data was available, for such projectiles as α's, only in the angular region forward of the Fraunhofer crossover (as is presently the case for heavy-ion projectiles on heavy targets), and it was noted that, in this N-dominated region, equally good fits could be obtained for a variety of different potentials if V_0 and a^2 were varied inversely. Something like this is surely true if one recalls from the estimates given in eqns. (3.10)–(3.14) (which really only apply for equal-geometry potentials, but indicate trends in general) that the slope of $\sigma_N(\theta)$ can be increased by increasing *either* V_0 or a. Of course, these changes have *opposite* effects on the slope of $\sigma_F(\theta)$, so such potentials are "ambiguous" only if the Far-side component, visible beyond the crossover, is not experimentally available. Goldberg *et al.*[21] pointed out this large-angle sensitivity to V_0 in the context of the nuclear rainbow, noting that, if the absorption is sufficiently small, it is reasonable to associate the falloff in $d\sigma/d\Omega$ (really in $\sigma_F(\theta)$) with the "tail" or dark side of the nuclear rainbow.

Figure 16a shows the cross-sections for three heavy ion combinations which are conceivable candidates for such a description: $^9Be + ^{16}O$ ($E_L = 158$ MeV),[17] $^6Li + ^{28}Si$ ($E_L = 135$ MeV)[22] and $^{12}C + ^{12}C$ ($E_L = 300$ MeV).[19] Note that we have not symmetrized the C + C amplitude about 90°, in order to facilitate the comparison; this has no significant effect for $\theta < 70°$, where the data stop. Without seeing the Far-side cross-sections, there is little hope of knowing how to interpret these data in the $\theta > 20°$ region, beyond the crossover. The Far-side cross-sections are given in Fig. 16b and, unfortunately, show almost

---

* We note that the effect is very similar to that of increasing the energy, as was shown in Fig. 5.
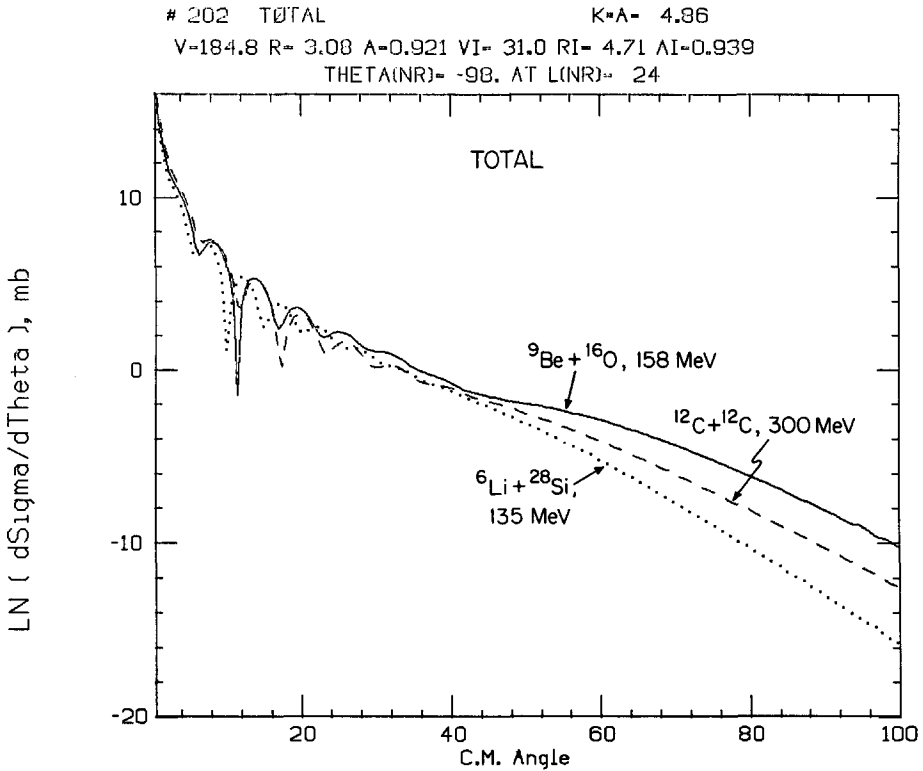
Fig. 16a. $d\sigma/d\theta$ for three recently-measured angular distributions.

no indication at all of the "Airy minima" one would expect on the bright side of the nuclear "rainbow angle" [which we estimate as $\simeq 90$–$100°$ from the simple-minded approximation $\theta(\ell) \simeq 2\mathrm{Re}\,(d\delta/d\ell)$]. As a means of understanding this a bit better, Fig. 17b shows the cross-section given by one of the potentials obtained by Brandan[18] for the 288.6 MeV data of Cole et al.[20] for $^{12}\mathrm{C} + {}^{12}\mathrm{C}$, and Figs. 17a and 17c show how it changes if either its real or its imaginary part is removed. Removing V of course steepens $\sigma_F(\theta)$ so much that the crossover is removed altogether, while removing W makes the entire cross-section Far-side dominated, and shows a spectacular nuclear rainbow, with a nuclear rainbow angle around $-64°$.* Its bright side oscillations are due, as usual, to the interference of two ℓ-values which send flux into the same (negative-angle) direction. Since they are closer together in ℓ ("shorter baseline") than the diametrically-opposed limb-points responsible for N/F interference, their maxima are spaced farther apart in angle, in accord with the peak-to-peak angular separation formula

$$\Delta\theta = \frac{2\pi}{\Delta\ell}. \tag{4.1}$$

Figure 17d compares these three cross sections on the same graph.

---

* We note the interesting confirmation of the prediction of eqn. (3.11) that reducing W *increases* the slope of $\sigma_N(\theta)$. It is this which "exposes" the rainbow oscillation in $\sigma_F(\theta)$, which would otherwise remain hidden beneath $\sigma_N(\theta)$.

202 FAR   K*A= 4.86

V=184.8 R= 3.08 A=0.921 VI= 31.0 RI= 4.71 AI=0.939

THETA(NR)= -98. AT L(NR)= 24

FAR SIDES ONLY

^{9}Be+^{16}O , 158 MeV

^{12}C+^{12}C, 300 MeV

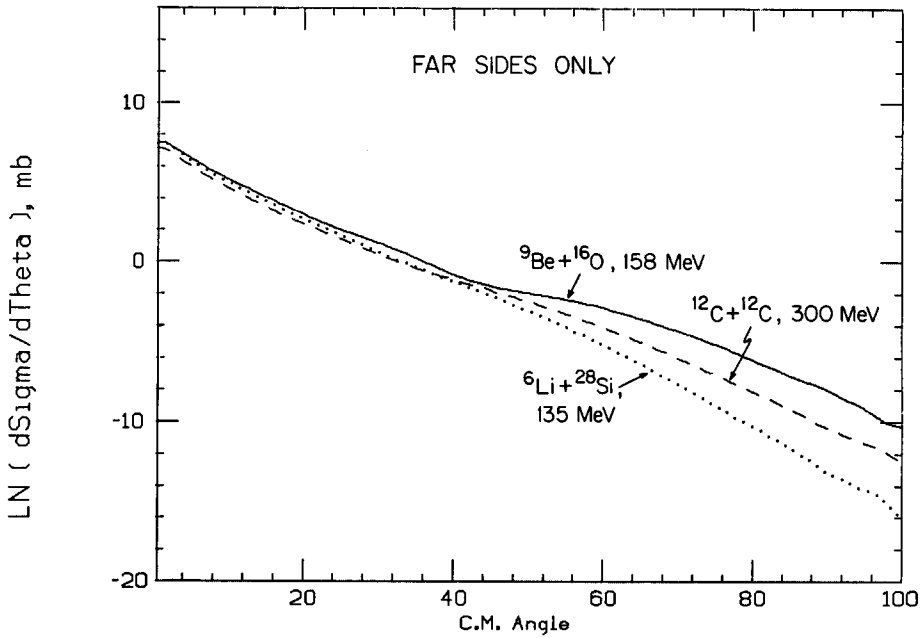^{6}Li+^{28}Si,
135 MeV

LN (dSigma/dTheta), mb

C.M. Angle

Fig. 16b. Far sides for the cross-sections of Fig. 16a.

1/4-THETA= 4.7, K*AI= 4.44, THETA(NR)=-178. AT L(NR)= 54

V= 0.00, R= 3.21, A=0.870, VI= 68.00, RI= 4.40, AI=0.690
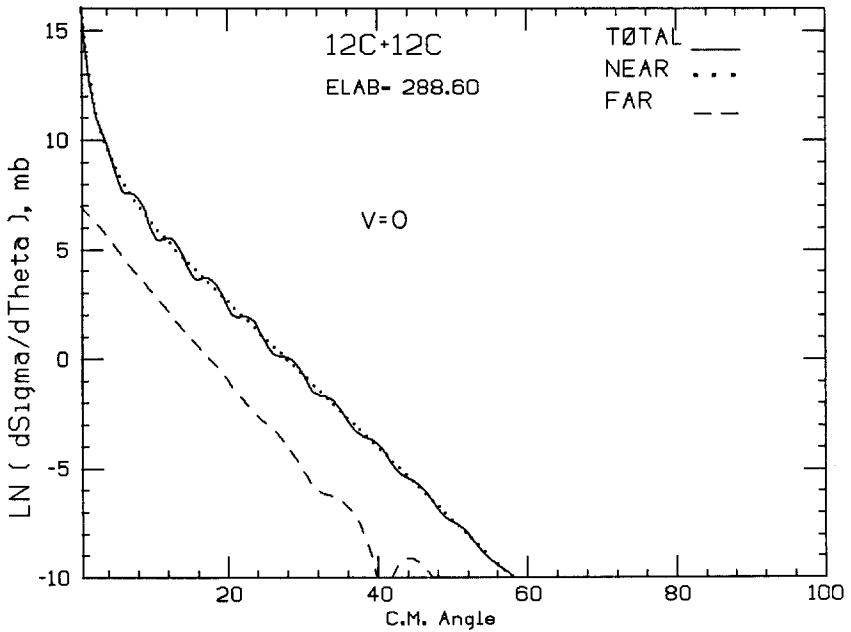
12C+12C

ELAB= 288.60

TØTAL ____
NEAR . . .
FAR   _ _

V=0

LN (dSigma/dTheta), mb

C.M. Angle

Fig. 17a. ^{12}C+^{12}C angular distribution (not symmetrized about 90°) for the potential of Brandan, Ref. 18, with
$V = 0$.

1/4-THETA- 4.7, K·AI- 4.44, THETA(NR)- -88. AT L(NR)- 26
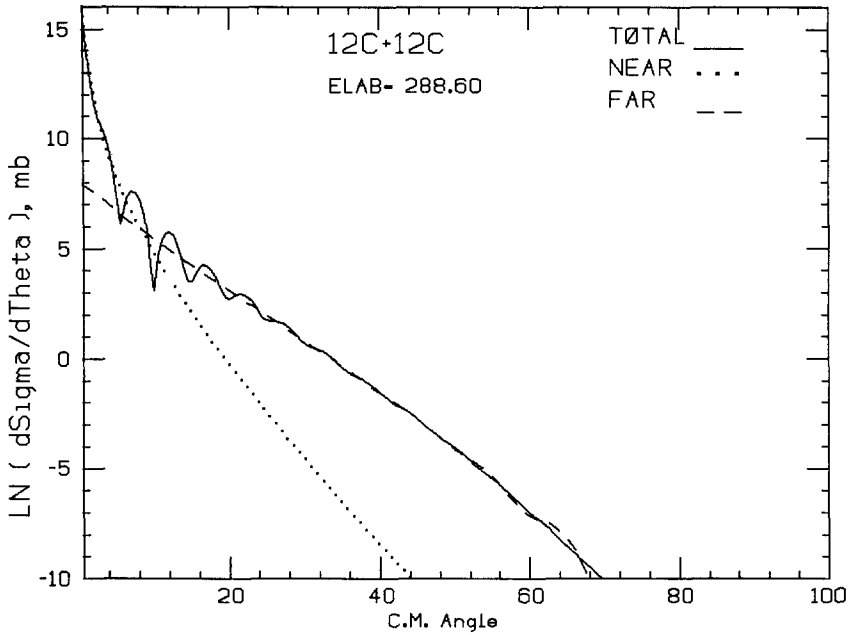V-200.00, R- 3.21, A-0.870, VI- 68.00, RI- 4.40, AI-0.690

Fig. 17b. $^{12}C + {}^{12}C$ with the potential of Ref. 18.

1/4-THETA- 0.0, K·AI- 4.44, THETA(NR)--179. AT L(NR)-161
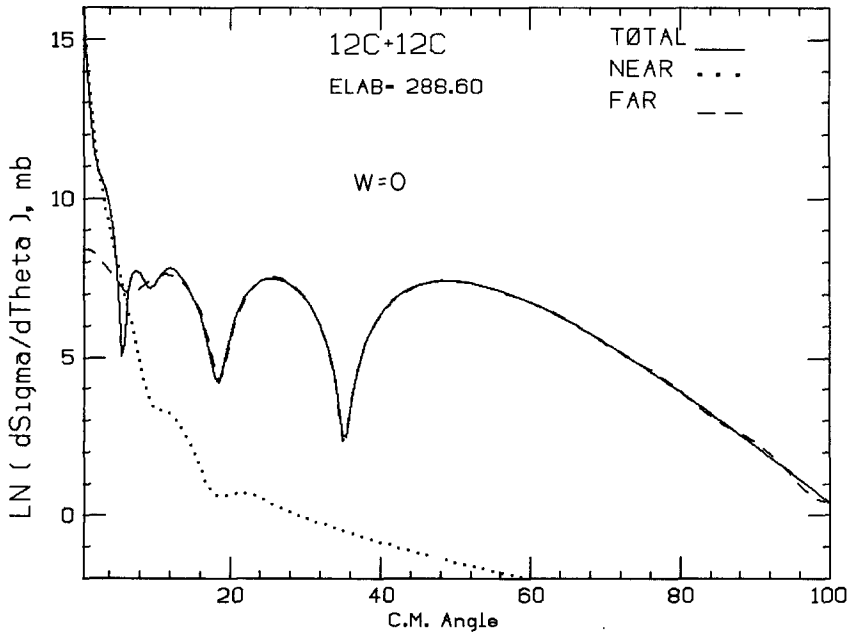V-200.00, R- 3.21, A-0.870, VI- 0.00, RI-·····-, AI-0.690

Fig. 17c. Same as Fig. 17b, with $W = 0$. Note the strong "Airy maxima" of a nuclear rainbow in $\sigma_F(\theta)$.

1/4-THETA- 4.7, K·AI- 4.44, THETA(NR)--178. AT L(NR)- 54
V- 0.00, R- 3.21, A-0.870, VI- 68.00, RI- 4.40, AI-0.690
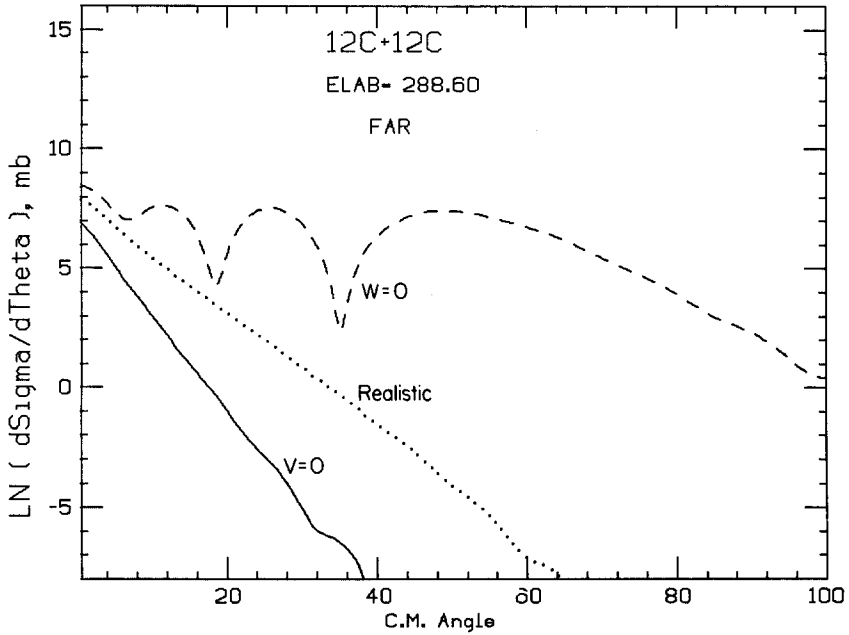
Fig. 17d. The Far-side curves of Figs. 17 a, b and c.

1/4-THETA- 2.3, K·AI- 4.44, THETA(NR)--234. AT L(NR)- 36
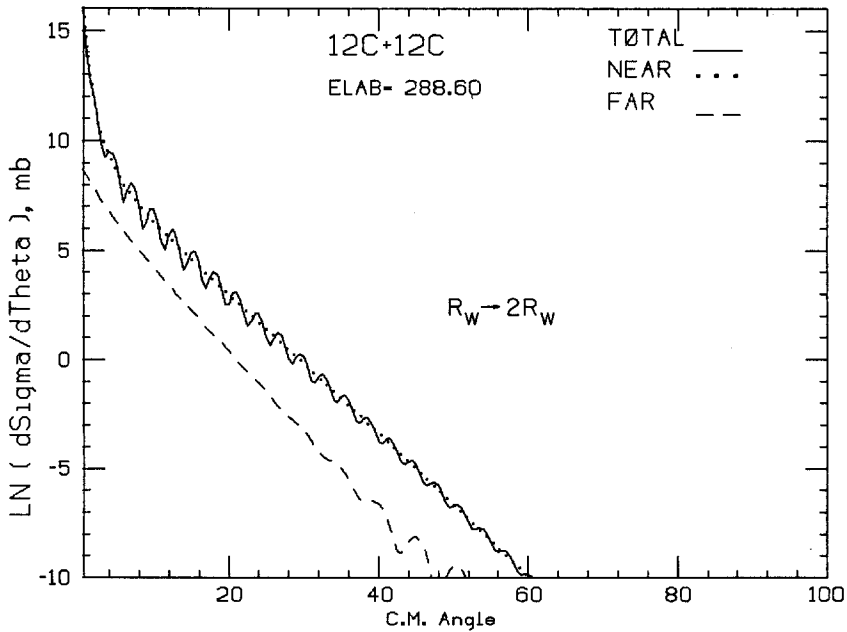V-200.00, R- 3.21, A-0.870, VI- 68.00, RI- 8.79, AI-0.690

Fig. 18a. ^{12}C + ^{12}C. Same as Fig. 17b, but with the radius of $W(r)$ doubled, producing a "diffractive" angular distribution, with $\sigma_N(\theta)$ and $\sigma_F(\theta)$ nearly parallel.
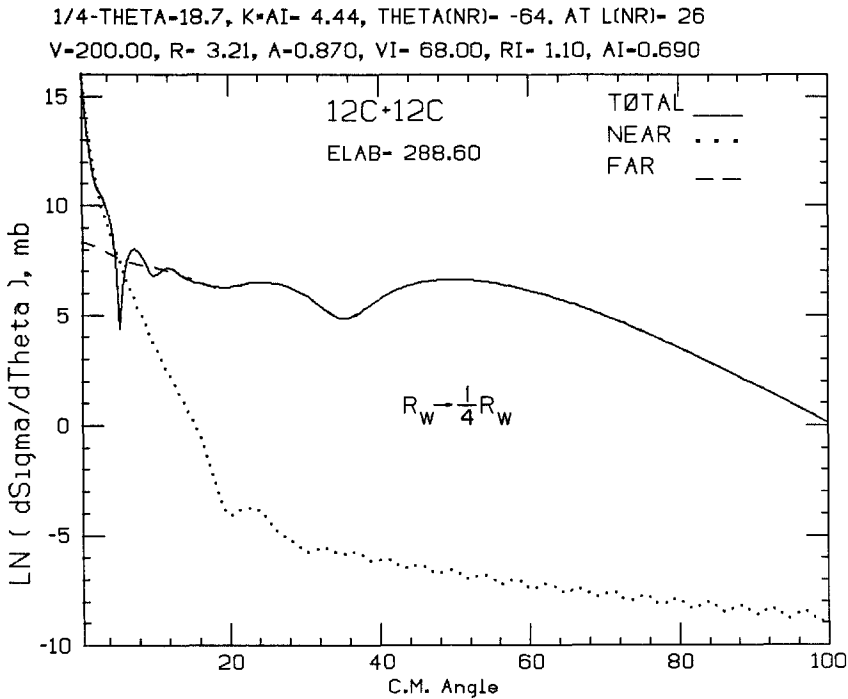
1/4-THETA-18.7, K*AI- 4.44, THETA(NR)- -64. AT L(NR)- 26
V-200.00, R- 3.21, A-0.870, VI- 68.00, RI- 1.10, AI-0.690

Fig. 18b. Same as Fig. 17b, but with the radius of $W(r)$ reduced by a factor of 4. Note the nuclear rainbow beginning to emerge as its inner-ℓ contribution is "freed" from absorption.

Figure 18 provides further information by exploring the effect of changing the radius of the imaginary potential. Doubling R_W essentially removes the effect of V altogether, making the cross section N-dominant (Coulomb effect), with $\sigma_N(\theta)$ and $\sigma_F(\theta)$ parallel. Reducing R_W to $R_w/4$, on the other hand, "frees" the inner ℓ of the nascent rainbow, which was previously suppressed by absorption, thus permitting a bit of the Airy pattern to develop; note that it begins with the *largest*-angle minimum, whose "inner ℓ" is nearest the surface and so the first to be "freed" as R_W decreases. Finally, reducing R_W to zero (Fig. 17c) frees more of the inner ℓ's, permitting more of the bright-side pattern to emerge.

Can the original curve, Fig. 17b, be appropriately labelled evidence for a nuclear rainbow? That depends entirely on what one understands by a rainbow. If one requires the full Airy-type pattern, with bright-side "supernumerary bows", then clearly this is not a rainbow. Various experimental groups[18,19,22] have adopted the "rainbow" terminology for any "structureless falloff" at angles beyond the Fraunhofer crossover, intuitively sensing, perhaps, that the difference in slope before and after the crossover is an indication of different amplitudes. In the present context, it seems to us that it is the crossover *itself* which is most significant, not the exact shape of $\sigma_F(\theta)$ beyond the crossover. It is the crossover which signals the influence of the nuclear refraction, by measuring the F-slope against the N-slope. From what we have seen of amplitudes for any projectiles heavier than α-particles, it seems likely that they will experience sufficient absorption to make their Far-sides "structureless" at *all* angles, "bright" or "dark". The term rainbow seems to us rather inappropriate in this case; "Far-side shadow", "Far-side falloff" or some such noncommittal term would appear preferable.
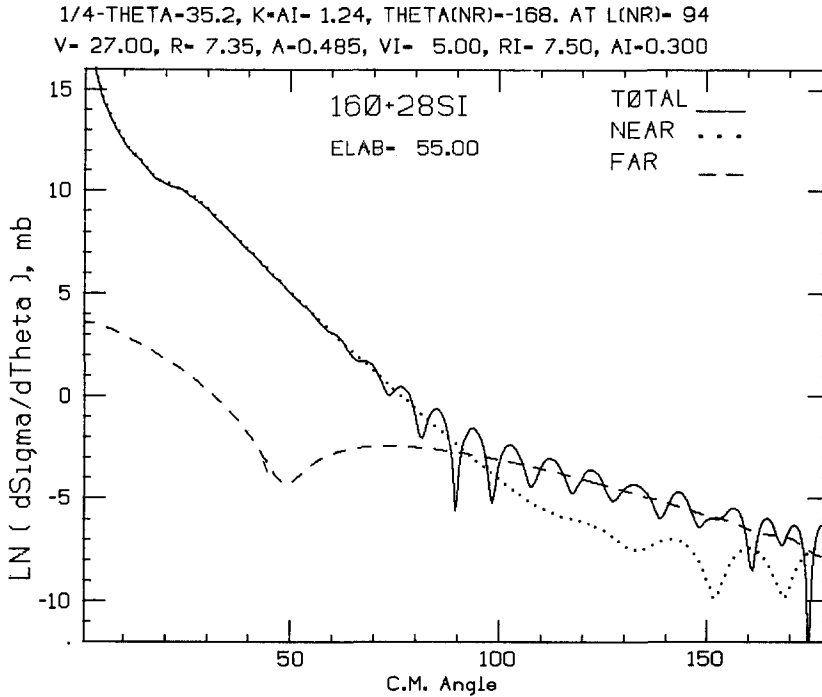
1/4-THETA-35.2, K*AI- 1.24, THETA(NR)--168. AT L(NR)- 94
V- 27.00, R- 7.35, A-0.485, VI- 5.00, RI- 7.50, AI-0.300

Fig. 19. $^{16}O + ^{28}Si$. Modification of a potential employed by Dehnhard et al., Ref. 23. Note the "hidden rainbow" in $\sigma_F(\theta)$, not visible in the cross-section itself.

4.4. A hidden rainbow

The Fig. 7 referred to in Section 1.5 is the best example we have yet seen of what appears to be a true nuclear rainbow, in the sense that the broad minimum around 90° is a purely Far-side phenomenon for which we see no other explanation than Far–Far interference. The next-best case we know of is the "Near miss" of Fig. 19. This comes from a highly refractive "equal geometry" potential $(V \simeq 5W)$ employed by Dehnhardt[23] to fit the 55 MeV scattering of ^{16}O on ^{28}Si. He employed a "parity-dependent" term $(-1)^\ell$ in the partial-wave expansion, which enhanced the back angles to fit the data. Since this primarily "lifted" the back-angle cross-section ("anomalous large-angle scattering") without changing its oscillatory pattern, we have left it out for simplicity. The resulting Far-side amplitude shows a clear rainbow dip at 45°—which unfortunately is invisible in the full cross-section, because of the total N-dominance in this region. It is interesting that in this particular case, at least, the oscillations in the backward hemisphere arise from the interference of the Near-side amplitude with the rainbow tail of the Far side.

4.5. The Case of the transparent surface

The "E18" potential of Cramer et al.[24] for $^{16}O + ^{28}Si$ scattering has acquired a certain notoriety as a classic example of an "absorptive" potential. It may consequently come as something of a surprise that it has distinctly "refractive" characteristics at forward angles. Its WS parameters, as shown in Fig. 6 and repeated in Fig. 20a, are (in MeV and Fm) $V = 10$, $R = 7.5$, $a = 0.618$, $W = 23.4$, $R_I = 6.83$ and $a_I = 0.552$. Since $R > R_I$ (by about $2a$), it is

1/4-THETA- 9.9, K*AI- 4.51, THETA(NR)--177. AT L(NR)-200
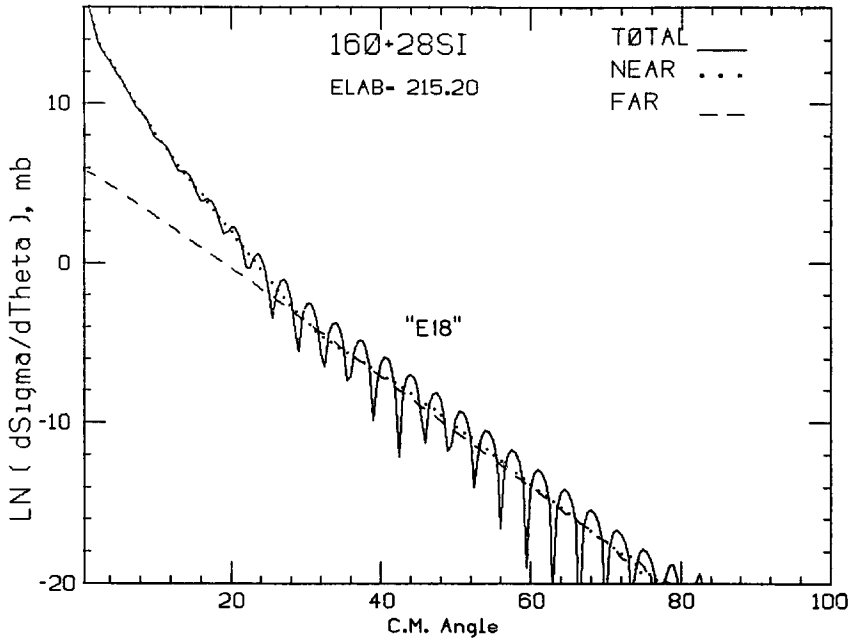V- 10.00, R- 7.50, A-0.618, VI- 23.40, RI- 6.83, AI-0.552

Fig. 20a. $^{16}O + ^{28}Si$. Repeat of Fig. 6, for the diffractive potential, $E18$, of Cramer *et al.*, Ref. 11.

173   NEAR   K*A- 5.05
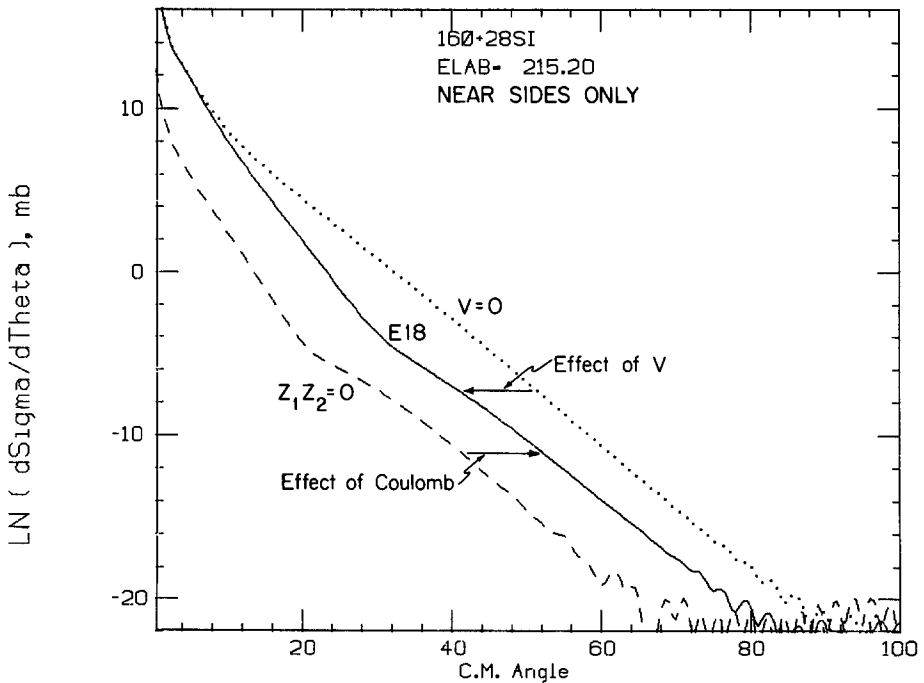V- 10. R- 7.500 A-0.618 VI- 23. RI- 6.830 AI-0.552

Fig. 20b. $\sigma_N(\theta)$ for the $E18$ potential, indicating how it changes if either the Coulomb or the nuclear refraction is removed.

# 173   NEAR   K=A= 5.05
V= 10. R= 7.500 A=0.618 VI= 23. RI= 6.830 AI=0.552

160+28SI
ELAB= 215.20
NEAR SIDES ONLY

$a_I \rightarrow a_I/2$

$W \rightarrow W/5$

E18

LN (dSigma/dThetα), mb

C.M. Angle
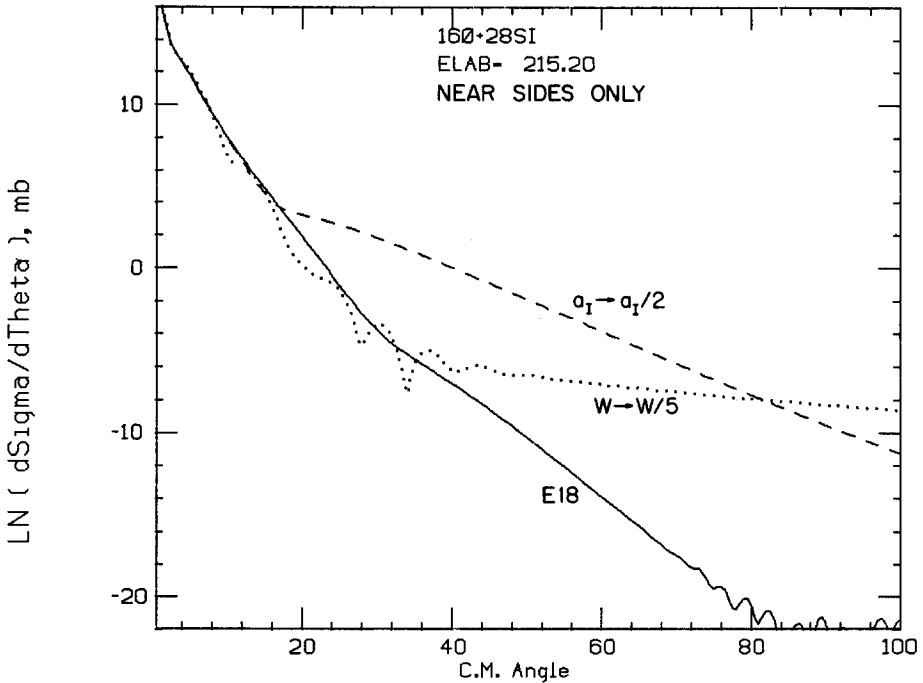
Fig. 20c. $\sigma_N(\theta)$ for the $E18$ potential, showing how it is modified by (a) decreasing the surface-thickness of $W(r)$, or (b) decreasing the depth of $W(r)$.

1/4-THETA= 9.9, K=AI= 4.51, THETA(NR)=-177. AT L(NR)=186
V= 10.00, R= 6.83, A=0.618, VI= 23.40, RI= 6.83, AI=0.552

160+28SI   TØTAL ____
ELAB= 215.20   NEAR . . .
                           FAR ___ ___

LN (dSigma/dThetα), mb

C.M. Angle

Fig. 20d. The $E18$ potential modified by reducing R_V to equal R_W, thus removing the "kink" at 30° which is present in Figs. 20a and b.

technically a surface-transparent potential, but $V \simeq W/2$, so actually $W(r)$ is deeper than $V(r)$ in the critical range between R and R_I; $V(r)$ is deeper than $W(r)$ for $r > R$.

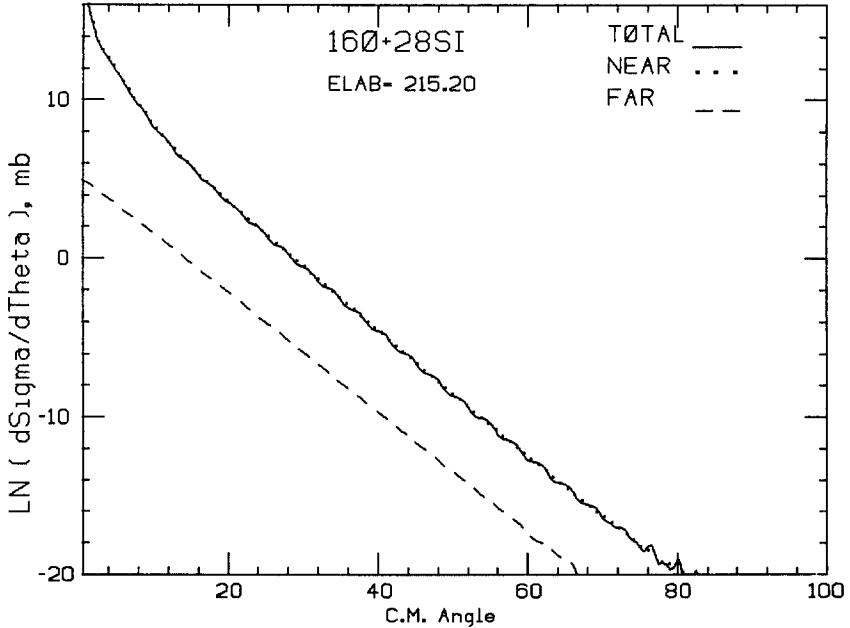The remarkable property of its forward-hemisphere angular distribution is the long sequence of N/F interference oscillations extending from 20° to 80°, together with the *absence* of such oscillations forward of 20°. This is accomplished by making $\sigma_N(\theta)$ and $\sigma_F(\theta)$ *parallel and equal* over the 20–80° range (no crossover!), together with a "kink" in $\sigma_N(\theta)$, whose steep slope for $\theta < 30°$ is reduced at that point to the lower value necessary to keep it "tangent" to $\sigma_F(\theta)$ for the larger angles.

This is an example of the type of subtle interplay of refraction and absorption which is distinctly beyond the reach of any of the simple $S(\ell)$-parametrizations so far[1] proposed. It should also be remembered, however, that the experimental data[24] only extend out to about 30°, just where the interesting region starts; it would clearly be of considerable interest to know what happens beyond that, especially in connection with the other potentials discussed in the following section.

The ingenious device the computer-search found for achieving this angular distribution is a "black ball enclosed in a glass casing", i.e., an inner absorber, with a refractive (though weak) real potential extending beyond it as shown in Fig. 21. An examination of $d\sigma/d\sigma_R$ shows that the angles forward of 5° are pure point-Coulomb scattering, but the $5° < \theta < 20°$ range is distinctly a *Coulomb-rainbow tail* in this case, i.e., these impact parameters are large enough that the scattering is reflection (Near-side) from the glass shell only. It is only for $\theta > 30°$ that the Near-side trajectories penetrate deeply enough to encounter the strong inner absorption—and thereafter $\sigma_N(\theta) = \sigma_F(\theta)$ in exactly the manner of a pure absorber: in this region, the *external* nuclear refraction has exactly cancelled the "angular shift" of the Coulomb field.

This can be seen very directly in Fig. 20b. Removing V removes the 30° N-side kink (by decreasing the N-side slope, as usual), giving a pure-absorber-plus-Coulomb $\sigma_N(\theta)$ all the way forward to the pure Coulomb range, $\theta < 5°$; it is parallel to the $E18$ $\sigma_N(\theta)$ for $\theta > 30°$, showing that the *external* nuclear refraction merely *shifted* that exponential decay, rather than changing its slope. Removing the Coulomb potential, on the other hand, shifts $\sigma_N(\theta)$ the other way, to smaller angles; in the range $\theta > 30°$, the two shifts are seen to be essentially equal and opposite.

E18 Potential

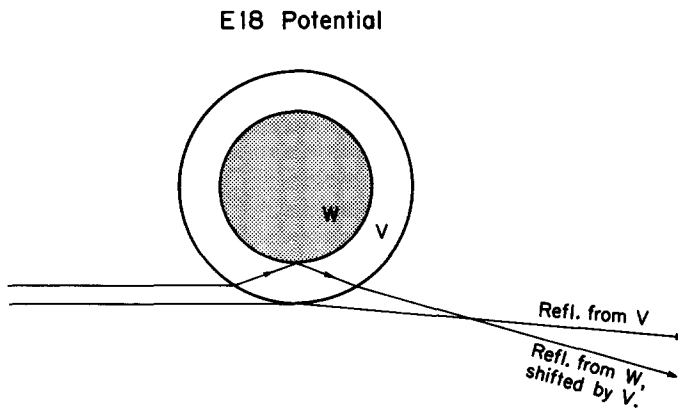

Fig. 21. Schematic representation of the $E18$ potential, with inner absorption and outer refraction. For $5° < \theta < 30°$, $\sigma_N(\theta)$ results from reflection from $V(r)$, while for $\theta > 30°$ it comes from reflection from $W(r)$.

The $5° < \theta < 30°$ range, on the other hand, is shown by Fig. 20c to be due to the external refractor alone. As a test, one of the curves in Fig. 20c results from decreasing a_I by a factor of 2; this is seen to decrease the slope of $\sigma_N(\theta)$ in the "absorptive region" by just a factor of 2, while leaving the slope in the forward-angle "refractive region" unchanged. Alternatively, decreasing V_I by a factor of 5 also leaves the $\theta < 30°$ slope unchanged—though it does introduce oscillations at larger angles due to a contribution from waves which have entirely circumnavigated the target, and so interfere with the "direct" reflection; these are normally suppressed by the larger V_I.

As a final comment on this system, Fig. 20d shows the cross-sections which result if the original $E18$ potential is changed by simply reducing R from 7.5 to 6.83 Fm, to make it equal to R_I. This provides another verification that the "kink" in $\sigma_N(\theta)$, together with is steeper slope for $\theta < 30°$, were produced by that portion of $V(r)$ which extended outside $W(r)$, for removing this portion by reducing R to equal R_I removes both the kink and the steep forward slope of $\sigma_N(\theta)$ altogether.

In summary, the way in which this "surface-transparent" $E18$ potential functions optically to produce the 2-slope $\sigma_N(\theta)$ of Fig. 20a is indicated in Fig. 21. For $5° < \theta < 30°$, the impact parameters are small enough to produce reflection from the external portion of $V(r)$, but too large to "see" the internal absorber. For larger angles the rays do penetrate far enough to reflect from the absorber (thus decreasing the N-slope), but the external nuclear refraction re-directs them in such a way that the "external" scattering angle, observed asymptotically, is *smaller* than the "internal" angle of reflection from the surface of the absorber. The effect of the external attractive nuclear potential is thus to pull the Near angular distribution $\sigma_N(\theta)$ forward (relative to Fig. 20d) in all cases; at small angles it does so by *steepening* its slope (in accord with eqn. (3.12)) and at larger angles it does so by *shifting* the "pure-absorber" $\sigma_N(\theta)$ forward, without change in slope, in the manner of an external prism.

4.6. Potential ambiguities

It is particularly interesting to examine the N/F analysis of *different* amplitudes which provide equally good fits to a given experimental angular distribution. The $^{16}O + ^{28}Si$ system is a case in point, since Satchler[25] has shown that potentials can be found which are of a very different type from the $E18$ potential just discussed, yet fit the data equally well.

DeVries et al.[22] have drawn a distinction between "refractive" and "diffractive" optical potentials. A "refractive" potential in their classification is a W-S potential with $V > 4W$ (but $R_V < R_W$); operationally, it is one which produces a prominent Fraunhofer crossover ("nuclear rainbow", in their terminology), as is seen for projectiles lighter than, say, ^{16}O. A "diffractive" potential, in their terms, has $V < W$ and engenders no crossover, at least in the angular range investigated.

Their $E18$ potential is the classic example of a "diffractive" potential, and has the merit of fitting the $^{16}O + ^{28}Si$ elastic data over the bombarding energy range from 38 MeV to 215 MeV; the data extend out to 100° at 38 MeV and to 30° at 215 MeV. As we have seen above, none of these angular distributions extend beyond the crossover, if indeed there is one at all; the 143 MeV and 215 MeV data show strong Fraunhofer oscillations "beginning" (as a function of θ), but the data stop before the oscillations do.

What Satchler discovered[25] was that "refractive" potentials could also be found, which fit the available data equally well, provided the imaginary diffuseness was allowed to increase with bombarding energy (by 30% over the above energy range). Figures 22a–c compare the $E18$ N/F decomposition at 215.2 MeV with those for two of Satchler's

1/4-THETA- 9.9, K*AI- 4.51, THETA(NR)--177. AT L(NR)-200
V- 10.00, R- 7.50, A-0.618, VI- 23.40, RI- 6.83, AI-0.552

16Ø+28SI

ELAB- 215.20

TØTAL

$(WS)^2$ (Refractive)

"A-type" (Refractive)

E18 (Diffractive)

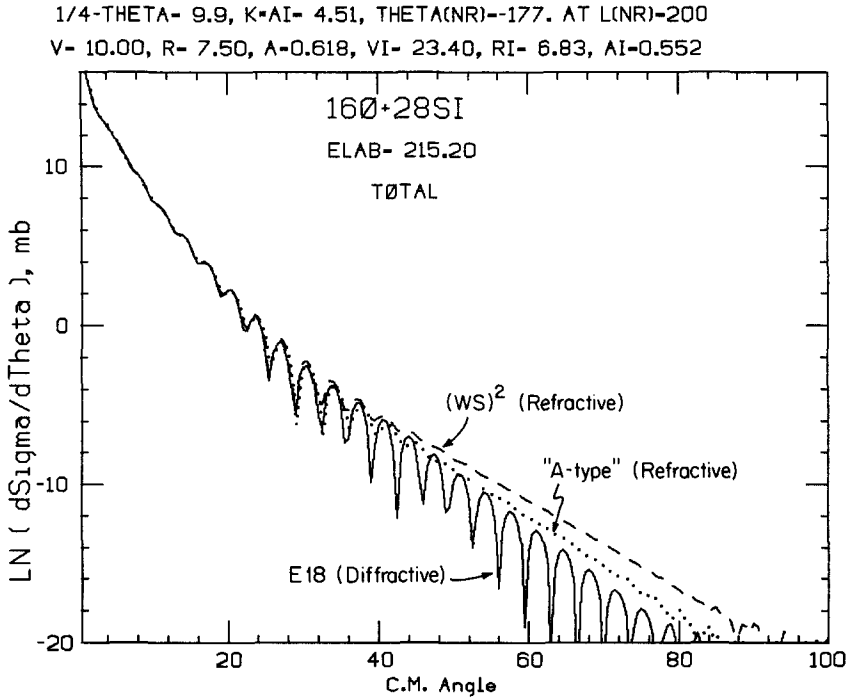Fig. 22a. A comparison of angular distributions for three potentials which fit the $^{16}O + {}^{28}Si$ data equally well; the data points do not extend beyond 30°.

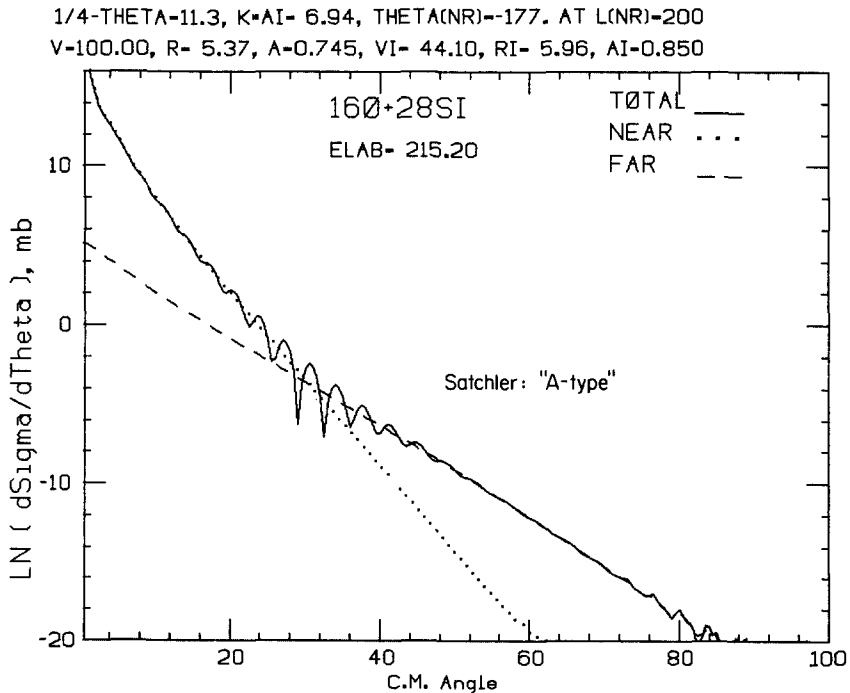1/4-THETA-11.3, K*AI- 6.94, THETA(NR)--177. AT L(NR)-200
V-100.00, R- 5.37, A-0.745, VI- 44.10, RI- 5.96, AI-0.850

16Ø+28SI

ELAB- 215.20

TØTAL ___
NEAR ...
FAR ___

Satchler: "A-type"

Fig. 22b. One of Satchler's potentials from Fig. 22a.

1/4-THETA-13.5, K·AI- 7.84, THETA(NR)--204. AT L(NR)- 40
V-149.00, R- 5.80, A-1.180, VI- 90.00, RI- 5.00, AI-0.960

16Ø+28SI

ELAB- 215.20

TØTAL ——
NEAR · · ·
FAR — —

Satchler,
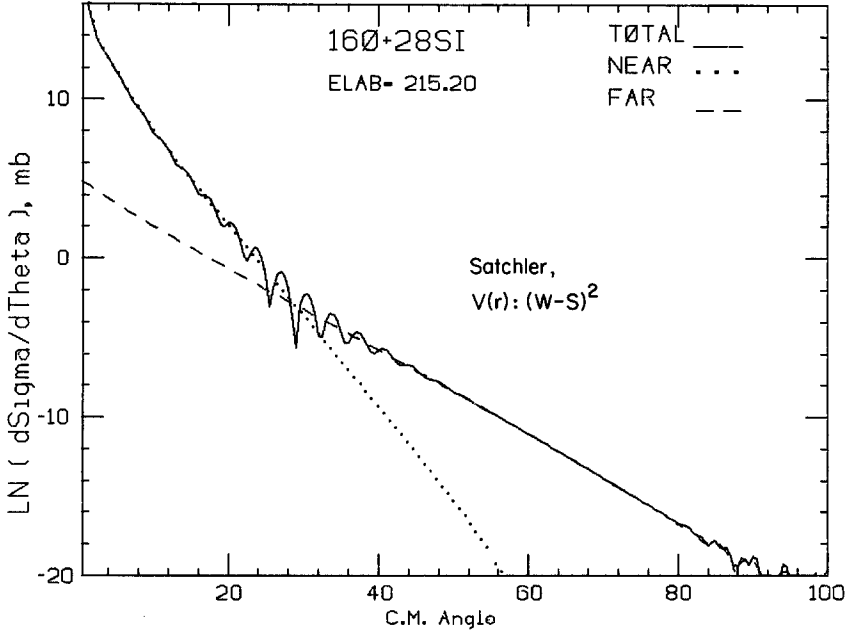$V(r): (W-S)^2$

LN (dSigma/dTheta), mb

C.M. Angle

Fig. 22c. The other of Satchler's potentials from Fig. 22a.

1/4-THETA- 9.9, K·AI- 4.51, THETA(NR)--177. AT L(NR)-200
V- 10.00, R- 7.50, A-0.618, VI- 23.40, RI- 6.83, AI-0.552

16Ø+28SI

ELAB- 215.20

NEAR

E18

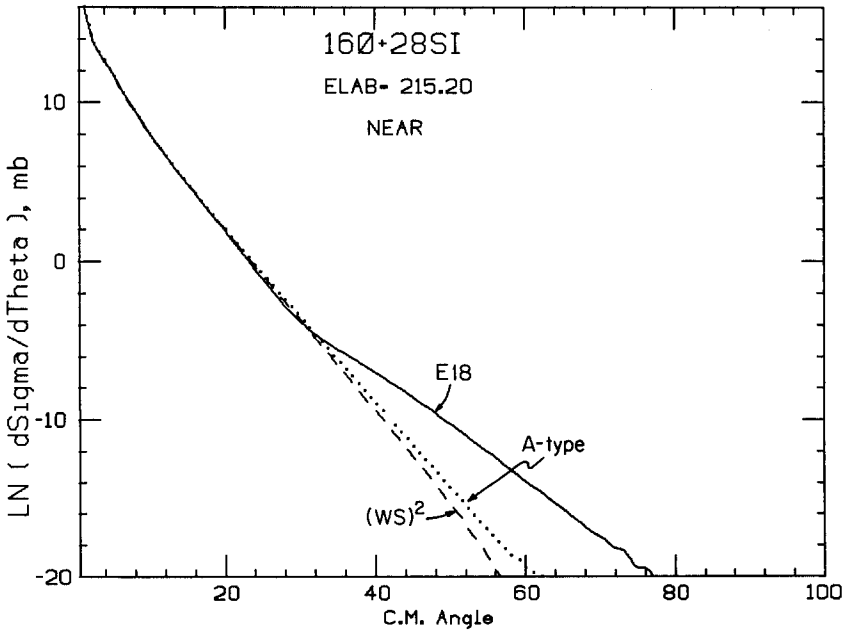A-type

$(WS)^2$

LN (dSigma/dTheta), mb

C.M. Angle

Fig. 22d. Same as Fig. 22a: Near sides.

1/4-THETA- 9.9, K*AI- 4.51, THETA(NR)--177. AT L(NR)-200
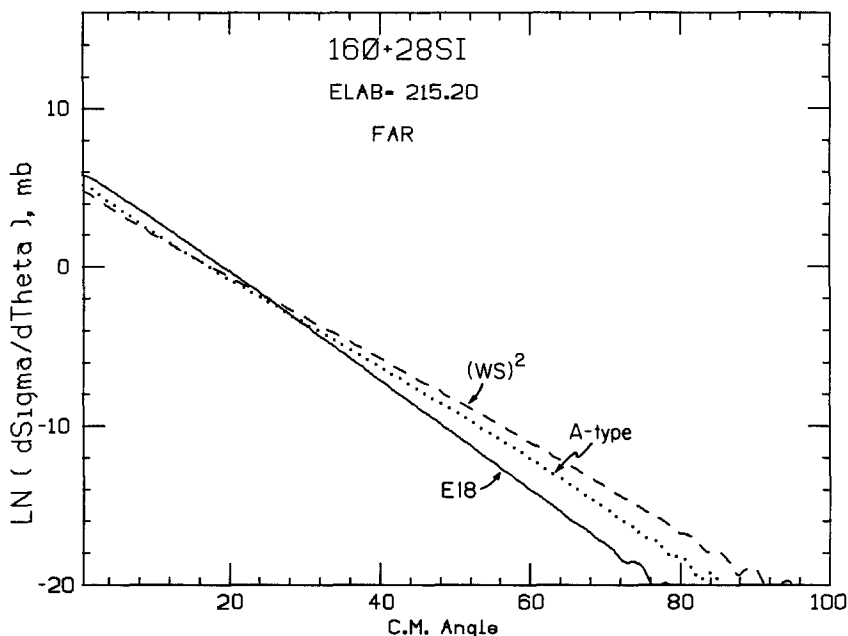V- 10.00, R- 7.50, A-0.618, VI- 23.40, RI- 6.83, AI-0.552

Fig. 22e. Same as Fig. 22a: Far sides, which agree at the crossover of 22b and 22c, the only angular range where the available data see $\sigma_F(\theta)$.

potentials. Although they do agree closely for $\theta < 30°$, they are clearly not phase-equivalent potentials, for they predict distinctly different angular distributions beyond 30°, in accord with their diffractive and refractive natures. $E18$, as mentioned, has no real crossover, while the two refractive potentials exhibit more-or-less "slow" crossovers, occurring just about where the available data end.

To attempt to explain their agreement for $\theta < 30°$, we note that in all cases the angular distributions are clearly N-dominated over much of the range covered by the data, so that getting $\sigma_N(\theta)$ right, at all energies, is essential. We know that $E18$ accomplishes this, in the $\theta < 30°$ range, by reflection from $V(r)$ alone (i.e., the Coulomb rainbow tail). According to eqn. (3.12), this means that its N-slope is just $2\pi ka$, which indeed is confirmed by Fig. 22a. Its energy dependence consequently is just that given by the k-factor.

Satchler's refractive potentials, on the other hand, are not "surface-transparent", i.e., their R_V does not substantially exceed R_W (and their $\sigma_N(\theta)$ does not show the "kink" of $E18$). Consequently their $\sigma_N(\theta)$ will not be determined by $V(r)$ alone. Again using eqn. (3.12) as a qualitative guide, this surface-strength of $W(r)$ will *decrease* their N-slopes below $2\pi ka$. It was evidently in order to increase this slope back to the $E18$ value that Satchler was forced to increase a_I (and thus the "average a" to which the slope must be proportional). Figures 22d and e compare the N and F components of the three angular distributions.

Figure 23 compares the $E18$ *potentials* with those for Satchler's A-type potential, whose $W(r)$ is energy-dependent. At large r (between 8 and 11 Fm), $V(r)/W(r)$ is nearly the same for the two potentials, using the 38 MeV $W(r)$. However, as E increases, the important r-range decreases, and the $V(r)/W(r)$ for A-type deviates from that for $E18$. In particular, e.g.,
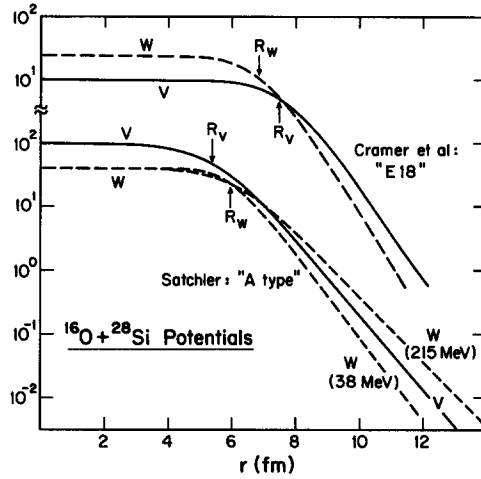
Fig. 23. A comparison of two of the potentials from Fig. 22a.

$V(r) > W(r)$ for the low-energy A-type potential at *all* r-values, while $V(r)$ and $W(r)$ cross, for $E18$, at 7.5 Fm. This $r \simeq R$ behavior is better approximated by the high-energy A-type potential, for which $V(r)$ and $W(r)$ do cross, at 7 Fm. It is evidently by allowing a_I to increase with E that Satchler is able to maintain the correct N-slope, and so to reproduce the $E18$ angular distribution at forward angles; with this insight available, it would seem that allowing W to increase with E might have done the job at least as well.

Fig. 24. N/F decomposition for the angular distribution of Fig. 2.

4.7. Just for fun

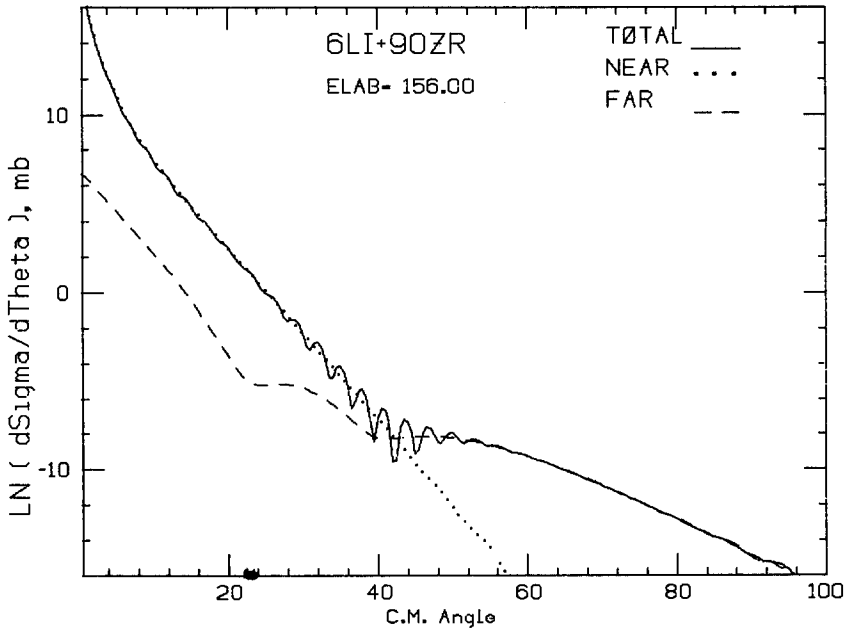As a fitting close to this list of applications of the N/F decomposition we site a few interesting curiosities, as something of an indication of the range of angular distributions which can be produced by judicious variations in the refractive and absorptive parameters of the optical potential.

4.7.1. *Another hidden rainbow?*

Figure 24 shows the N/F decomposition of the $^6Li + ^{90}Zr$ angular distribution of Fig. 2. The potential is a typical "refractive" one, $V \simeq 5W$, but $R_I \simeq R + 2.5a$. At forward angles the trajectories evidently do not penetrate deeply enough to encounter this refraction, and $\sigma_N(\theta)$ and $\sigma_F(\theta)$ show the customary parallel lines of a strong absorber, shifted by $2\theta_{1/4}$. However, around 22° and 40°, dips reminiscent of the bright side of a nuclear rainbow occur in $\sigma_F(\theta)$, changing its slope drastically and producing the N/F crossover, beyond which $\sigma_F(\theta)$ dominates. This would seem to provide a strong argument for viewing the "hump" in $\sigma_F(\theta)$ (obscured in $d\sigma/d\theta$ itself by the crossover) at $\simeq 55°$ as the main maximum of a nuclear rainbow.

4.7.2. *A bizarre α-dip*

α-particle scattering from ^{40}Ca is one of the classic examples of "anomalous large-angle scattering", and Fig. 25 shows one of the fits which Delbar *et al.*[26] obtained to their

V-181.0 R- 4.69 A-1.290 VI- 17.3 RI- 5.99 AI-1.000
THETA(NR)--114. AT L(NR)- 13

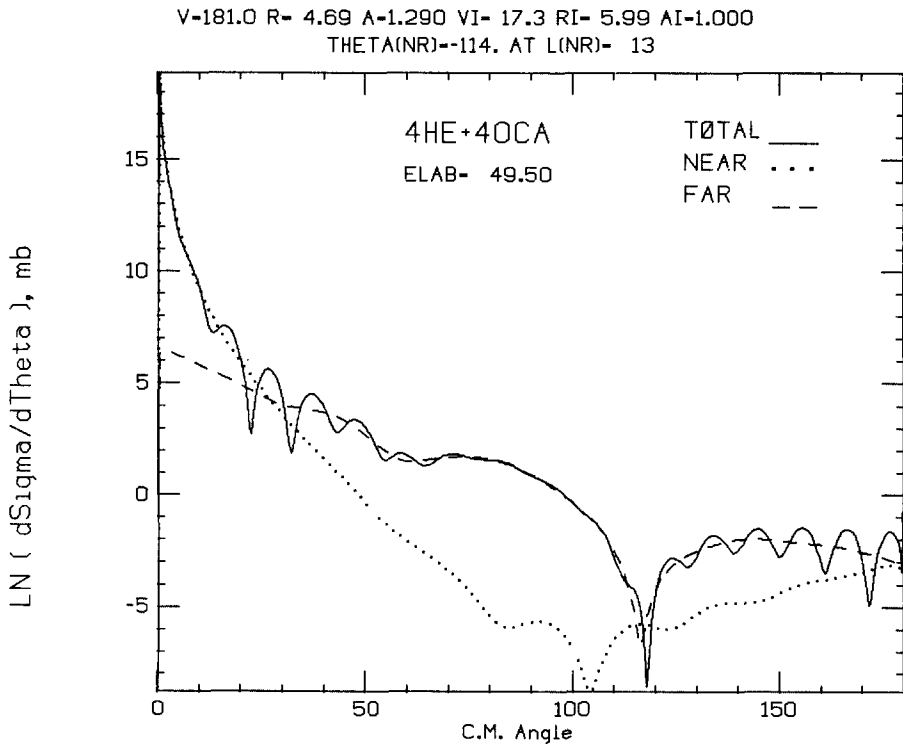4HE+40CA   TØTAL ____
ELAB- 49.50   NEAR ...
                 FAR ___

Fig. 25. The anomalous large-scale scattering of $\alpha + {}^{40}Ca$. Note the deep minimum at 120°, which occurs in the Far-side amplitude.

experimental data by the use of $(WS)^2$ potentials. It displays a quite normal crossover at 25°, and a good backward glory, but its unusual feature is the very sharp dip, distinctly in the Far-side amplitude, at 120°. It is highly unlikely that this is a nuclear-rainbow dip, especially since it *fills in* if $W \rightarrow 0$. As yet we have no simple explanation for it, though Delbar *et al.*[25] found that, in the alternative (and very different) Internal/Barrier Amplitude decomposition of Brink and Takigawa,[27] it arises from destructive interference between the internal and barrier terms. The Fraunhofer diffraction minima, on the other hand, are always a "barrier" phenomenon, in agreement with our description in terms of peripheral ℓ-windows.

4.7.3. *A pure Coulomb rainbow*

Figure 26 shows an example of when *not* to use the N/F decomposition. It is a case of purely electromagnetic scattering, with no nuclear potential at all, $V = W = 0$. The electrostatic potential, however, is not point-Coulomb, but that of the customary uniform charge distribution. This is "more attractive" (i.e., less repulsive) than a point-Coulomb field, and produces the impressive forward-angle oscillations of a "pure" Coulomb rainbow, in which "Fresnel diffraction" clearly plays no role whatever.

Even more curiously, however, the smoothly-falling tail of this rainbow is seen to "change character" at 40°; forward of 40° it is, as expected, purely Near-sided, but beyond 40° it is represented as a strong and smooth destructive interference between the Near and Far amplitudes. This serves as a useful warning that for a non-absorptive potential, which allows flux to pass through its center, the distinction between N and F becomes quite meaningless for central (small-ℓ) trajectories. When they dominate, the N/F representation, though "true" by definition, may not be enlightening.

1/4-THETA-20.1, K*AI- 6.20, THETA(NR)-   8. AT L(NR)-139

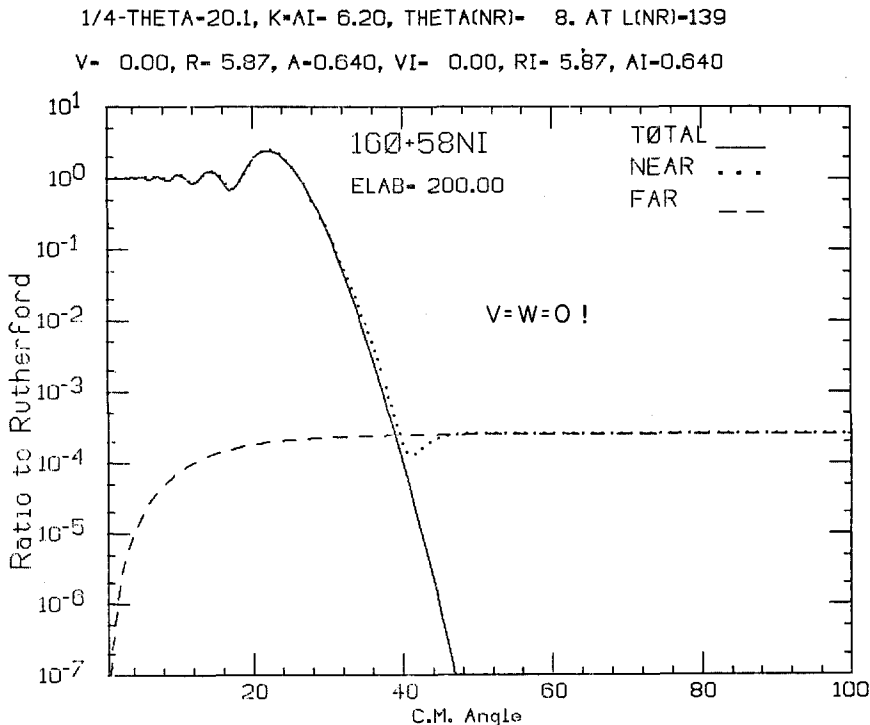V- 0.00, R- 5.87, A-0.640, VI- 0.00, RI- 5.87, AI-0.640

Fig. 26. Scattering by a uniform distribution of charge, with no nuclear potential. Note the fine Coulomb rainbow.

1/4-THETA- 0.0, K*AI- 5.23, THETA(NR)--180. AT L(NR)-216

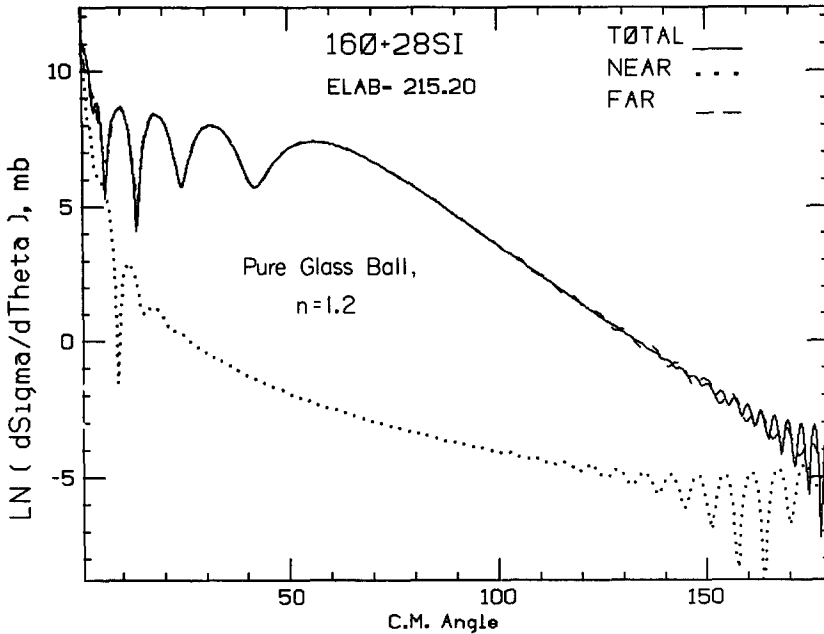V-100.00, R- 5.89, A-0.640, VI- 0.00, RI- 5.89, AI-0.640

Fig. 27. Scattering by a pure glass ball (no absorption, no Coulomb) of refractive index $n = 1.2$; $kR = 50$.

4.7.4. *Pure glass*

Finally, Fig. 27 shows an example from "classical optics": the scattering pattern by a pure glass ball (index of refraction $= (1 + V/E)^{1/2} = 1.2$), with neither absorption nor Coulomb field. It produces a fine Far-side rainbow as well as back-angle "glory" oscillations, and is not substantially different from the refraction pattern of Fig. 17c, which differs only in the inclusion of Coulomb scattering.

5. NUCLEAR FORWARD GLORY SCATTERING

Formally, whenever the deflection function $\theta(\ell)$ passes through zero, $d\sigma/d\Omega$ should contain a "forward glory" enhancement.[4] It will, of course, be completely masked by Coulomb scattering, but the suggestion has recently been made[28] that a careful application of the optical theorem to heavy ion scattering may unambiguously reveal the forward glory contribution.

The optical theorem, as usually stated for charged particle scattering, is

$$\int d\Omega \left[\frac{d\sigma}{d\Omega} - \frac{d\sigma_{\text{Ruth}}}{d\Omega} \right] + \sigma_R = \frac{4\pi}{k} \text{Im}[f(0) - f_{\text{Ruth}}(0)], \qquad (5.1)$$

where $d\sigma/d\Omega \equiv |f(\theta)|^2$ is the elastic scattering cross section $d\sigma_{\text{Ruth}}/dr \equiv |f_{\text{Ruth}}(\theta)|^2$ the Rutherford (point Coulomb) cross-section, and σ_R is the total reaction cross-section. Special care should be taken when evaluating the integral in eqn. (5.1). Usually the lower limit is

replaced by a small angle θ_0 and the contribution from the region $0 < \theta < \theta_0$ is found to be oscillatory and small as long as the angle θ_0 is chosen small enough.

In the presence of a forward glory (real stationary phase in $f_N(\theta)$ at $\theta = 0$ and $\ell_{fg\ell}$), the amplitude $f(0) - f_{Ruth}(0)$ may be approximately evaluated by the method of stationary phase, as was done originally by Ford and Wheeler.[4] The result is

$$f(0) - f_{Ruth}(0) \simeq k^{-1}(\ell_{g\ell} + 1/2)\left(\frac{2\pi}{|d\theta/d\ell|_{\ell_{g\ell}}}\right)^{1/2}|S^n_{\ell_{g\ell}}| \exp\left[2i(\sigma_{\ell_{g\ell}} + \delta_{\ell_{g\ell}}) - \frac{\pi}{4}\right], \quad (5.2)$$

where $\ell_{g\ell}$ is the glory angular momentum, $\theta \equiv 2(d/d\ell)(\sigma_\ell + \delta_\ell)$ is the total deflection function and σ_ℓ and δ_ℓ are the point Coulomb and nuclear phase shifts respectively. $|S^n|$ is the nuclear reflection coefficient evaluated at $\ell_{g\ell}$.

Substituting (2) in (1), we finally obtain

$$\Delta\sigma_R \simeq \sigma_R + \int dr\left[\frac{d\sigma}{d\Omega} - \frac{d\sigma_{Ruth}}{d\Omega}\right]$$

$$\simeq \frac{4\pi}{k^2}(\ell_{g\ell} + 1/2)\left(\frac{2\pi}{|d\theta/d\ell|_{\ell_{g\ell}}}\right)^{1/2}|S^n_{\ell_{g\ell}}| \sin\left[2(\sigma_{\ell_{g\ell}} + \delta_{\ell_{g\ell}}) - \frac{\pi}{4}\right]. \quad (5.3)$$

Equation (5.3) clearly shows that $\Delta\sigma_R$ should oscillate as a function of energy, with a local period given approximately by

$$P_E \simeq \frac{\pi}{|\partial/\partial E(\sigma_{\ell_{g\ell}} + \delta_{\ell_{g\ell}})|} \simeq 2\pi\hbar/\tau_{\ell_{g\ell}}, \quad (5.4)$$

where τ is the collision time associated with the forward glory trajectory. Under semi-classical conditions, this time may be related to the interaction potential through the usual classical relation.

We should stress that $\Delta\sigma_R$ has an oscillatory behavior as a function of energy, even in the absence of a real stationary phase point corresponding to $\theta = 0$.[30] The presence of a forward glory enhances these oscillations to an extent that renders $\Delta\sigma_R$ amenable to unambiguous measurement.

It is clear from eqn. (5.3) that $\Delta\sigma_R$ is very sensitive to the details of θ near the glory angular momentum. This sensitivity should be exploited fully in order to determine the details of the interaction potential at distances smaller than the strong absorption radius. It was clearly demonstrated in Ref. 28 that two different optical potentials, both accounting well for the ratio σ/σ_{Ruth} in the forward angle region, generate quite different $\Delta\sigma_R$'s.

To exhibit fully the dependence of $\Delta\sigma_R$ on the underlying optical potential parameters, we work out below its form at high energies, $E > V_n + V_c$. Both $\sigma(\ell)$ and $\delta(\ell)$ simplify at high energies[31] (see Appendix on deflection functions),

$$\sigma(\ell) \simeq -C\eta + \eta \ln(\ell + 1/2) \quad (5.5)$$

and

$$\delta(\ell) = \left(\frac{\pi\mu ab}{E}\right)^{1/2}\frac{V_0}{2\hbar}\exp[-(b - R)/a], \quad (5.6)$$

where C is Euler's constant, $C = 0.5772156659$, η the Sommerfeld parameter, V_0 the strength of the nuclear interaction and $(\ell + 1/2) = b(2E/h)^{1/2}$.

Given σ and δ, all other physical quantities appearing in $\Delta\sigma_R$, eqn. (5.2) may be calculated. We obtain[31]

$$\Delta\sigma_R \simeq AE^{1/4}\exp[-B_3/E^{1/2}]\sin\left[\frac{2}{E^{1/2}}(B_1 + B_2 \ln E) - \frac{\pi}{4}\right], \quad (5.7)$$

where

$$A = \left[\frac{32\pi^3 \hbar b_{g\ell}^4 a}{\sqrt{2\mu} Z_1 Z_2 e^2 (b_{g\ell} - a)} \right]^{1/2}, \tag{5.8}$$

$$B_1 = \frac{Z_1 Z_2 e^2}{\hbar (2/\mu)^{1/2}} \left[-C + \tfrac{1}{2}\ln\left(\frac{2\mu}{\hbar^2}\right) \right] + (\pi \mu m a b_{g\ell})^{1/2} \frac{V_0}{2\hbar} \exp\left[\frac{-(b_n - R)}{a} \right], \tag{5.9}$$

$$B_2 = \frac{Z_1 Z_2 e^2}{2(2/\mu)^{1/2}\hbar}, \tag{5.10}$$

$$B_3 = (\pi \mu a b_{g\ell})^{1/2} \frac{W_0}{\hbar} \exp\left[-(b_{g\ell} - R)/a \right], \tag{5.11}$$

and $b_{g\ell}$ is obtained from $d/d\ell (\sigma_\ell + \delta_\ell)]_{b_{g\ell}} = 0$

$$b_{g\ell} = R \left\{ 1 + \frac{a}{2R - 3a} \left(3\ln R - \ln\left[\frac{2a}{\pi} \left(\frac{Z_1 Z_2 e^2}{V_0} \right)^2 \right] \right) \right\}. \tag{5.12}$$

In calculating eqn. (5.7) we have assumed equal geometry for the real and imaginary parts of the optical potential. This restriction may easily be removed by using for a and R that appear in B_3 (eqn. (5.11)) the relevant imaginary part parameters.

Equation (5.7) demonstrates clearly that at higher energies the amplitude of the glory oscillation increases with energy like $E^{1/4} \exp[-B_3/E^{1/2}]$. Further, the local period of oscillation, P_E, is[31]

$$P_E = \frac{\pi}{(\partial/\partial E)(\sigma_{g\ell} + \delta_{g\ell})} = \frac{2\pi E^{3/2}}{B_1 + (\ln E - 2)B_2}, \tag{5.13}$$

and increases with E like $E^{3/2}/\ln E$ at higher energies. This is to be expected, since the collision time, $\tau \propto 1/P_E$, must decrease with increasing center of mass energy.

It should be clear that the amplitude of oscillation, though an increasing function of energy eventually must saturate. The limiting value of $\Delta\sigma_R$ may be easily obtained[30] as simply $-2\pi R_{ab}^2$, where R_{ab} is the characteristic strong absorption radius that also defines the limiting geometrical value of the total reaction cross-section $\sigma_R \to \pi R_{ab}^2$.

To obtain an idea of the value of $\Delta\sigma_R$, we present in Table 1 the result of a calculation obtained with the Christensen–Winther empirical potential[32]

$$V_n(r) = -50 \frac{R_1 R_2}{R_1 + R_2} \exp\left[-(r - R_1 - R_2)/a \right] \text{[MeV]}$$

$$R_i = 1.233 A_i^{1/3} - 0.978 A_i^{-1/3} \text{[fm]}$$

$$a = 0.63 \text{[fm]}. \tag{5.14}$$

Table 1.

System	A [fm² MeV$^{-1/4}$]	B_1 [MeV$^{-1/2}$]	B_2 [MeV$^{-1/2}$]	B_3 [MeV$^{-1/2}$]	$\Delta\sigma_R$ (mb)	P_E (MeV)
$^{12}C + ^{13}C$	77.46	13.93	7.10	4.66	1701.98	257.84
$^{16}O + ^{12}C$	67.80	20.27	9.91	5.92	1366.82	205.03
$^{12}C + ^{24}Mg$	58.17	35.97	16.06	8.28	−940.17	148.98
$^{16}O + ^{28}Si$	47.95	71.31	28.18	12.5	−705.61	110.82
$^{16}O + ^{40}Ca$	42.33	115.34	42.65	16.57	499.58	82.97

In the calculation of B_3, we have used for W_0 the value $V_0/2$, where $V_0 = 50(R_1 R_2)/(R_1 + R_2)$ (see eqn. 5.14), and have assumed equal geometries. Five heavy-ion systems have been considered, $^{12}C + ^{13}C$, $^{16}O + ^{12}C$, $^{12}C + ^{24}Mg$, $^{16}O + ^{28}Si$ and $^{16}O + ^{40}Ca$ at a laboratory energy corresponding to 20 MeV/Nucleon.

It is clear from the table that the forward glory effect is most effective in light heavy ion systems. This fact is also clear from eqn. (5.8). The period of the energy oscillation, exhibited in the last column of Table 1, is quite large, indicating clearly that the physical process we are discussing is very fast. It is worthwhile mentioning that our expression for the local period, eqn. (5.13) is quite accurate, even at lower energies. Evaluating P_E for the system $^{16}O + ^{12}C$ at $E = 40$ MeV, a case investigated in Ref. 28, gives a value of $\simeq 30$ MeV, very close to the value obtained through an exact optical model calculation (see Fig. 2 of Ref. 28). The experiment planned at Saclay ($^{16}O + ^{12}C$ elastic scattering at 20 MeV/Nucleon)[33] should shed some light on some of the questions discussed above.

6. DEVIATIONS FROM OPTICAL BEHAVIOR

6.1. Anomalous back-angle scattering

In the previous sections we have emphasized at length the wave optical behavior of the heavy ion system. This behavior comes about as a result of several gross properties of the system. Its relatively large size (Near-Far interference), the strong absorption present (diffraction), strong Coulomb repulsion and nuclear attraction (refraction and rainbow) and a well-defined surface region (determining the fall-off of $d\sigma/d\theta$ in the shadow region). These features, quite common in most heavy-ion systems, constitute a convenient and useful "language" with which the elastic scattering may be described and analyzed as we have shown previously. Nuclei clearly exhibit other features besides the gross ones mentioned above. These other properties are more closely related to specific nuclear structure aspects, e.g., deformation. Therefore one would expect several important deviations from the optical behavior, which we discuss in this section. A well-known case usually cited as exhibiting these deviations is that referring to systems behaving anomalously at back angles (α-scattering, $^{16}O + ^{28}Si$, etc.). What one usually discovers in these systems is a large increase in $\sigma/\sigma_{\text{Ruth}}(\theta)$ at back angles accompanied by a rather regular angular structure. Further, the excitation function $\sigma/\sigma_{\text{Ruth}}(\pi, E)$ at $\theta = \pi$ exhibits quite a conspicuous intermediate structure with an average width of about 1 MeV. To put the situation into perspective we show in Fig. 28 a plot of the experimental excitation function $d\sigma_{el}/d\Omega(E, \pi)$ for $^{16}O + ^{28}Si$ and $^{16}O + ^{30}Si$. One sees clearly that the data sit at a mid-point between a pure Rutherford (no nuclear structure whatsoever) and a pure strong absorption, $E18$ (nuclear structure manifested purely optically).

Several interpretations have been advanced in the quest for a consistent description of the data. For a detailed discussion we refer the reader to the recent review by Braun-Munzinger and Barrette.[34] These interpretations range from a pure resonance, intermediate structure, picture affecting both the angular distributions and the excitation functions, to a pure-direct picture involving basically coupled channels feed-back-type effects. Neither of these extreme pictures seems to account for all facts of the data. Although recent measurements of angular distributions of α-transfer reactions, as well as inelastic scattering, of systems such as $^{16}O + ^{28}Si$ indicate that a pure, isolated resonance generated, intermediate structure interpretation of the gross structure of the anomalous back angle elastic scattering is not viable,
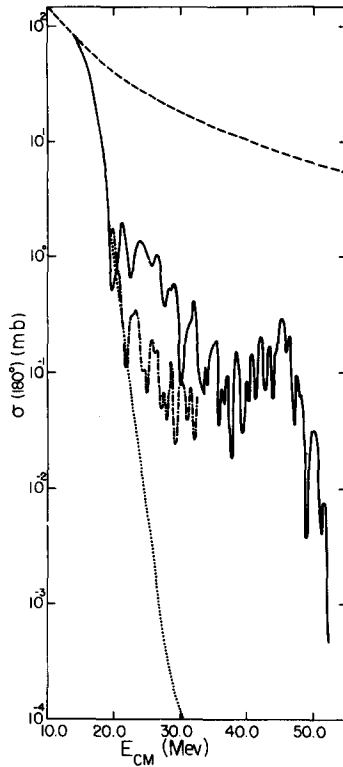
Fig. 28. 180°—Excitation functions for $^{16}O + {}^{28}Si$ (solid curve) and $^{16}O + {}^{30}Si$ (dash-dot curve). The dashed curve is pure Rutherford scattering and the dotted curve was calculated with the $E18$ potential of Ref. 11.

owing to the lack of clear channel correlations, some type of resonance-based phenomenon is, however, certainly taking place and generating the fine structure seen in most excitation functions.

Simple "direct" models have also been proposed for the purpose of explaining the gross features of the cross section at back angles. These range from simple changes in the "normal" optical potentials to simple changes in the "normal" elastic S-matrix. The necessity for invoking these changes in the normal "$E18$" type description arose from two important observations; (a) the quite conspicuous rise in σ/σ_{Ruth} (180°) to a value, at $E_{cm} = 35$ MeV, almost four orders of magnitude bigger than the corresponding "$E18$" value, and (b) the period of the angle oscillations, $\Delta\theta$, supplies a value of the contributing angular momentum $\ell_\theta(E)$ through $\Delta\theta \simeq \pi/\ell_\theta(E)$, which is twice as large as the angular momentum, $\ell_E(E)$ that determines the period, ΔE, of the energy oscillation in the 180°-excitation function, $\Delta E \simeq 1/[\partial\ell_E(E)/\partial E]$.

The first anomaly has been accounted for through the use of the so-called surface transparent potentials. These optical potentials are characterized by an imaginary part with very small diffuseness which results in an increased reflection. However, these potentials, though quite adequate in describing the angular distributions, fail dramatically in describing the second anomaly associated with the excitation function. This clearly points to the need for a second important modification of the normal optical $E18$ potential, namely the addition of a small, albeit important parity-dependent component (proportional to

$(-)^{\ell}$), which would not modify the angular distribution since it contributes mostly at back-angles. The 180° excitation function would then behave approximately $\sim \sin^2\{[\ell_E(E)/2]\pi\}$, thus giving rise to a local period $\Delta E = 2/[\partial \ell_E(E)/\partial]$, permitting the identification $\ell_\theta(E) = \ell_E(E)$. Ref. 35 exhibits the type of fit to the E-oscillations obtained by the Minnesota group with the above-mentioned two modifications in the optical potential describing $^{16}O + ^{28}Si$. A fit of a similar quality to the E-oscillations in the 180° excitation function was obtained in Ref. 36 using, as a starting point, an S-matrix description. The elastic S-matrix used contains a normal optical E18 type contribution, a parity-independent "window-like" contribution that peaks at an ℓ, slightly lower than the grazing one, and a small parity-dependent "window". The elastic S-element without the parity-dependent window was found to resemble very much the one generated from the surface transparent optical potential. The findings of Ref. 36 clearly support the conclusions reached by the Minnesota group concerning the need for a surface-transparent, parity-dependent optical potential.

We shall not attempt to discuss the microscopic origin of the above deviations from the optical behavior, as this would take us beyond the scope of the present review. For discussions on these and other points, we refer the reader to Ref. 34. We might just mention that the window-like deviations discussed above might be connected to the feedback onto the elastic channel from the coupling to an α-transfer channel. The fact that the anomaly at back angles is much enhanced when the two partners are α-nuclei lends some support to the above idea.

6.2. Static and dynamic deformation effects: Long range absorption

Another important case showing a clear deviation from optical behavior involves the scattering of deformed targets and/or projectiles at energies close to the Coulomb barrier. As a result of the strong Coulomb excitation of collective states, one expects a gradual depopulation of the elastic channel, even at sub-barrier energies. A nice example showing this effect is presented[37] in Fig. 29 involving the system $^{20}Ne + ^{19}Sm$, $A = 148$, 150 and 152. The strength of the coupling of the elastic O^+ channel to the 2^+ state increases gradually from vibrational (^{148}Sm) to rotational (^{152}Sm), as is clearly seen in the ^{20}Ne spectrum (Ref. 37). Consequently the depopulation (absorption) in the $^{20}Ne + ^{152}Sm$ is much stronger than either the $^{20}Ne + ^{150}Sm$ and $^{20}Ne + ^{148}Sm$. The cross-section ratio $\sigma(Ne + ^{152}Sm)/\sigma(Ne + ^{148}Sm)$ reaches its smallest value of ~ 0.2 at back angles.
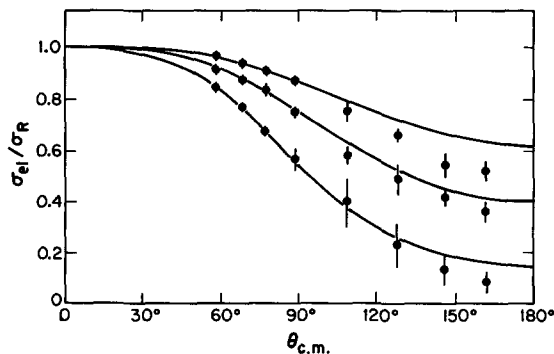

Fig. 29. Elastic scattering of ^{20}Ne on ^{19}Sm at 70 MeV, showing the effects of long-range absorption.

The trend of the data clearly points to the presence of *long-range* absorption to be contrasted with the nuclear short-range absorption responsible for the diffractive behavior discussed earlier. Actually the short-range nuclear absorption, at the sub-barrier energies involved in the ^{20}Ne-^{4}Sm system under discussion, would give rise to a minor deviation from the Rutherford scattering, concentrated at angles very close to 180°. We shall return to this point later.

The long-range nature of the absorption referred to above cannot, certainly, be accounted for by a change in the optical potential, and one has to resort to coupled channels calculations. A more drastic departure from the optical behavior arising from the same coupled channels effect is shown in Ref. 38. The *c.m.* energy at which the data were taken is slightly above the Coulomb barrier of ^{18}O + ^{184}W, and then one would expect a "Fresnel" form of $\sigma/\sigma_{\text{Ruth}}$ in the forward hemisphere. As one can clearly see the long-range absorption is quite strong even in this higher-energy case, resulting in a drastic modification of the "Fresnel" shape. Similar features are seen in the ^{12}C + ^{184}W system at $E_{\text{lab}} = 70$ MeV.

A way of simplifying the analysis of data such as the above one is through the construction of a component in the optical potential that represents the feed-back of the inelastic 2 + channel into the elastic channel. This may easily be done through Feshbach's theory of the optical potential, which gives, in the particle case of two channels, the following form of the polarization potential

$$V_{\text{pol}}(\mathbf{r},\mathbf{r}') = V_{02}(\mathbf{r})G_2^{(+)}(\mathbf{r},\mathbf{r}')V_{20}(\mathbf{r}'), \tag{6.1}$$

where $V_{02}(\mathbf{r})$ is the coupling potential and $G_2^{(+)}(\mathbf{r},\mathbf{r}')$ is the 2^+-channel Coulomb-modified Green's function.

When expanded in partial waves, the radial part of V_{pol}, would necessarily be angular momentum dependent and non-local. However, a locally-equivalent potential may be obtained approximately through the identification

$$\int V_{\text{pol}}(\mathbf{r},\mathbf{r}')\psi_\ell(kr')\,\mathrm{d}r' = V_{\text{pol}}(r)\psi_\ell(kr), \tag{6.2}$$

where $\psi_\ell(k,r)$ represents the radial wave function in the elastic channel. At subbarrier energies, $\psi_\ell(k,r)$ may be approximated by the regular Coulomb wave function $F_\ell(kr)$, which makes possible the construction of $V_{\text{pol}}(r)$. The resulting expression for $V_{\text{pol}}(r)$ may be written as, ignoring the energy loss involved in the excitation process,

$$V_{\text{pol}}(r) = -i\frac{2\pi}{25}\frac{E}{\eta}\frac{k^4}{\eta^2}\frac{B_T(E2)\uparrow}{Z_T^2 e^2}\left|\frac{3\bar{\ell}^2+1}{\bar{\ell}^2(\bar{\ell}^2+1)^2} - \bar{\ell}^{-3}\tan^{-1}\bar{\ell}\right.$$
$$\left. + \frac{4\bar{\ell}^2}{(\bar{\ell}^2+1)^2}\frac{a}{r} + \frac{2\bar{\ell}^4}{(\bar{\ell}^2+1)^2}\left(\frac{a}{r}\right)^2\right|\left(\frac{a}{r}\right)^3 \equiv iV_{\text{pol}}(r). \tag{6.3}$$

As a result of the assumption that the energy loss is zero $V_{\text{pol}}(r)$ comes out to be purely negative imaginary. The situation is reversed in the case of large energy losses, as $V_{\text{pol}}(r)$ becomes predominantly real. The reason is that in the former case the vibrational period is much larger than the collision time (sudden limit), therefore the system simply does not have enough time to react during the collision process and accordingly no modifications are inflicted on the real interaction. In the large-energy-loss case (virtual excitation of giant resonances), the system manages to execute several vibrations during the collision process, thus resulting in a change in the effective real ion–ion interaction, without inflicting much change in the absorptive component. For a detailed discussion on this point, see Ref. 39.

The above long-ranged potential is a rather smooth function of both ℓ and r. This feature

permits the inclusion in $\sigma/\sigma_{\text{Ruth}}$ of the effect arising from the polarization potential in a simple manner. At energies below the Coulomb barrier the elastic scattering amplitude is dominated by the Near-sided Coulomb part. Accordingly only one turning will contribute. Since the phase shift arising from $V_{\text{pol}}(r)$ is purely imaginary owing to the weakness of the perturbation, the total phase becomes

$$\delta_\ell = \sigma_\ell + i\frac{\mu}{\hbar^2}\int_{r_0}^{\infty}\frac{\hat{V}_{\text{pol}}(r)}{k_c(r)}\,dr, \tag{6.4}$$

and therefore the ratio of the elastic scattering cross section to the Rutherford one becomes

$$\frac{\sigma}{\sigma_{\text{Ruth}}} = \exp\left[-\frac{2\mu}{\hbar^2}\int^{\infty}\frac{\hat{V}_{\text{pol}}(r)}{k_c(r)}\,dr\right]. \tag{6.5}$$

Note that the above quantity is a function of angle since the ℓ that appears in r_0^c, $k_c(r)$ and $V_{\text{pol}}(r)$ is just the Coulomb stationary point, related to the angle through the Rutherford relation $(\ell+\frac{1}{2})/\eta = \cot\theta/2$. The integral in the exponent of eqn. (6.5) can be evaluated in closed form giving the final result, for a pure quadrupole excitation

$$\frac{\sigma}{\sigma_{\text{Ruth}}} = \exp\left[-\frac{16}{45}q^2 g(\theta)\right], \tag{6.6}$$

where

$$q^2 \equiv \frac{\pi}{5}\frac{k^4}{\eta^2}\left[\frac{B_T(E2)g_T(\xi_T)}{Z_T^2 e^2} + \frac{B_P(E2)g_P(\xi_P)}{Z_P^2 e^2}\right] \tag{6.7}$$

and

$$g(\theta) = \frac{9}{4}\left[\frac{1}{3}\left(\sin\frac{\theta}{2}\right)^4 + \left(\tan\frac{\theta}{2}\right)^4\left(1 - \left(\tan\frac{\theta}{2}\right)\frac{1}{2}(\pi-\theta)\right)^2\right] \tag{6.8}$$

where T and p refer to target and projectile. The angular function $g(\theta)$ attains its maximum value of unity at $\theta = \pi$, and it vanishes at $\theta = 0$. The solid lines in Fig. 29 are simply the $\sigma/\sigma_{\text{Ruth}}$ of eqn. (6.6) calculated after approximately accounting for the small energy-loss encountered in ^{20}Ne+Sm, through the quantities $g_T(\xi_T)$ and $g_P(\xi_P)$ with $\xi = \frac{1}{2}\eta(\Delta E/E)$. These quantities are tabulated in Ref. 39b.

The simple treatment of the feed-back problem involving the 0^+ and 2^+ channels, may easily be extended to include higher order processes (reorientation, 4^+ excitation, etc.). For more details we refer the reader to Ref. 40.

We turn now to energies slightly above the Coulomb barrier, Ref. 38 and 39. At such energies one would expect the Near-side amplitude to be still dominant. However, at least two complex stationary points will contribute. Accordingly, the amplitude becomes

$$f_{\text{N}}(\theta) = \frac{1}{k\sqrt{\sin\theta}}\sum_{i=1,2}\left|\frac{\lambda_i}{\theta'(\lambda_i)}\right|\exp\left[2i\delta(\lambda_i)-i\lambda_i\theta\right]\left|\exp\left[-\frac{\mu}{\hbar^2}\int_{r_0(\lambda_i)}^{\infty}\frac{V_{\text{pol}}^{(\lambda_i)}(r)}{k_{c,\lambda}(r)}\,dr\right]\right. \tag{6.9}$$

where $\delta(\lambda_i)$ and $\theta'(\lambda_i)$ are, respectively, the total complex phase shift and the derivative of the classical deflection function corresponding to the Coulomb plus the short-ranged nuclear interaction, evaluated at the complex λ_i.

The differential elastic cross section corresponding to $f_{\text{N}}(\theta)$ above would then show a marked deviation from the pure "Fresnel" shape. Actually the fit shown in Ref. 41 was obtained by adding a somewhat slightly different polarization potential (from that of eqn. (3)) obtained by Love et al. to a complex Saxon–Woods potential. The dashed curve shows

the cross section without the polarization potential. A similar quality fit was obtained by Baltz *et al.*[39] using the form of $f_N(\theta)$ given above, eqn. (6.9). Owing to the slow dependence of

$$\exp\left[-\frac{\mu}{\hbar^2}\int_{r_0(\lambda)}^{\infty}\frac{V_{\text{pol}}^{(\lambda)}(r)\,\mathrm{d}r}{k_{c,\lambda}(r)}\right]$$

on λ, one may, for the purpose of obtaining a simple qualitative description of the phenomenon, factor out the above exponential from the ℓ-sum and evaluate it at an average value of λ, $\bar{\lambda}=(\lambda_1+\lambda_2)/2$. This should be a reasonable prescription for the calculation of $\sigma/\sigma_{\text{Ruth}}$ at angles close to the big "Fresnel" peak. The result of such a calculation is shown in Ref. 41 (the dashed-dotted line).

7. SUMMARY

Elastic heavy-ion angular distributions result from a complex interplay of refractive, diffractive and interference phenomena, which must be understood in some detail if useful physical information is to be extracted from the art of fitting such angular distributions with optical potentials. Because these potentials are strongly absorbing, diffraction plays a central role in their angular distributions. The traditional Kirchoff (short-wavelength) approximation to the scattering amplitude for diffraction by a "distribution of absorbers" $\rho(\mathbf{r})$ has the Born-approximation form

$$f(\theta)\simeq\int e^{i\mathbf{q}\cdot\mathbf{r}}\rho(\mathbf{r})\,\mathrm{d}^3r, \tag{7.1}$$

in which the exponential or "retardation" factor assures that the contributions from the various points $\mathbf{r}$ of the absorber are weighted with phases proportional to their optical path-lengths from the observer. Although this Kirchoff formulation describes $f(\theta)$ as the coherent sum of contributions from all "internal" points of the *area* of the absorber (in the simple case of a thin planar absorber), an alternative but equivalent interpretation can be obtained by transforming this area integral into a line integral around the *boundary* of the absorber, as Born and Wolf[3] discuss for the case of a sharp-edged absorber. Physically this boundary integral describes the "edge wave" or "boundary diffraction wave", which is simply an alternative description of the scattered wave for a strong absorber.

This edge-wave formulation (see Fig. 1a) seems to us to offer exactly the insight needed to understand heavy-ion angular distributions, provided it is generalized to (a) permit the edge-thickness (the diffuseness a of the optical potential) to be nonzero, and (b) include nuclear and Coulomb refractive effects. In addition, in the $kR\gg 1$ limit, the only points of
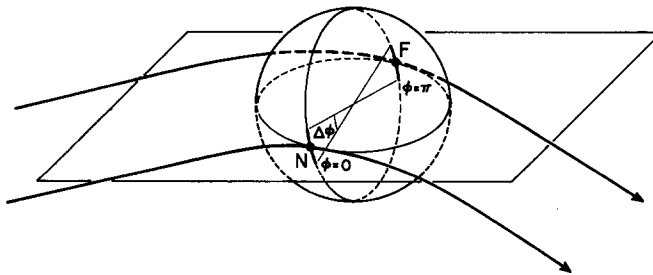

Fig. 30. Repeat of Fig. 8, showing origin of edge waves from regions of azimuthal width $\Delta\phi\simeq(\ell\theta)^{-1/2}$ near the scattering plane.

the integral (7.1) which contribute to $f(\theta)$ are those *in the scattering plane*. The boundary integral then shrinks to just two diametrically-opposed limb points, one Near and one Far, as indicated in Fig. 30. They will, of course, be modified by refraction, but it is this "natural" decomposition of $f(\theta)$ into two edge-point or edge-slit contributions which leads to the 2-slit representation of the amplitude for a strong absorber. Similarly, the N/F decomposition of the amplitude, although entirely general, acquires particular cogence in this strong-absorption case, when $f_N(\theta)$ and $f_F(\theta)$ have the physical significance of single-slit diffraction patterns. The exponential shapes of these patterns are approximated [for equal geometries of $V(r) + W(r)$] by eqn. (1.10), whose slope parameters β are

$$\beta_N = -\mathrm{Im}(r_0^N/a), \qquad \beta_F = \mathrm{Im}(r_0^F/a), \tag{7.2}$$

with $\mathrm{Im}\, r_0^N$ and $\mathrm{Im}\, r_0^F$ given by eqns. (3.12) and (3.14).

Figure 31 (which repeats Fig. 3c) provides a caricature of $\sigma_N(\theta)$ and $\sigma_F(\theta)$, showing that at energies high enough above the Coulomb barrier for the trajectories to feel the nuclear potential, a sufficiently strong real part (nuclear refractor) can make the F-slope steeper than the N-slope, producing a Fraunhofer crossover and a localized angular region of N/F interference oscillations. If the refraction is weak, $\sigma_N(\theta)$ and $\sigma_F(\theta)$ may only have roughly equal slopes, giving the pattern an extended region of Fraunhofer oscillations, of the type more familiar for simple "black disc" absorbers.

Finally, it is of considerable practical importance to recognize that the Near and Far slits (which can of course move (in r) with angle) may well occur at different distances of closest approach, and so explore different regions of the optical potential. A full understanding of how different parts of the optical potential affect different parts of the angular distribution can only be achieved by examining *both* $\sigma_N(\theta)$ and $\sigma_F(\theta)$, as the examples of Section 4 make abundantly clear.

In closing, we remark again that all N/F decompositions were done with a modified version of the elastic-scattering part of PTOLEMY.[42] It is available upon request, in a VAX version, from KWM at the University of Wisconsin.
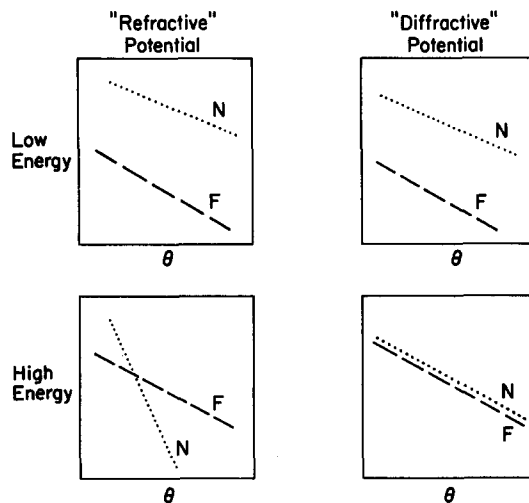

Fig. 31. Repeat of Fig. 3d.

REFERENCES

1. W. E. FRAHN, in: *Heavy-Ion Science*, Vol. 1 (ed. D. A. BROMLEY), Plenum Press, 1982; *Heavy Ion, High Spin States and Nuclear Structure*, ICTP, Trieste (1973); (IAEA, Vienna, 1975).
2. G. R. SATCHLER, *Direct Nuclear Reactions*, Oxford University Press, 1983.
3. This transformation of the usual Kirchoff integral over the *area* of the absorber into the form of contributions from its *perimeter* is due in part to Sommerfeld, and is described briefly (for a sharp-edged absorber) in: M. BORN and E. WOLF, *Principles of Optics*, 3rd Revised Edition, Pergamon Press, Oxford, p. 449, 1965. They refer to the edge wave as a "boundary diffraction wave".
4. K. W. FORD and J. A. WHEELER, *Ann. Phys. (NY)* 7, 259 (1959).
5. J. KNOLL and R. SCHAEFFER, *Ann. Phys. (NY)* 97, 307 (1976); R. SCHAEFFER (with the assistance of M. C. LEMAIRE) in: *Theoretical Methods in Medium-Energy and Heavy-Ion Physics* (eds. K. W. MCVOY and W. A. FRIEDMAN) Plenum Press, N.Y. 1978.
6. N. ROWLEY and C. MARTY, *Nucl. Phys.* A266, 494 (1976); C. MARTY, *Lecture Notes on Analysis of Heavy-Ion Scattering Amplitudes* (Orsay internal report IPNO/TH 79-3, 19/8).
7. K. W. MCVOY, Semiclassical Methods and Surface Creep Waves in Heavy Ion Reactions, *Notas de Fisica* 1, No. 4 (UNAM, Mexico 20, DF, 1978).
8. J. COOK *et al.*, *Nucl. Phys.* A388, 173 (1982).
9. R. D. AMADO, J. P. DEDONDER and F. LENZ, *Phys. Rev.* C21, 647 (1980).
10. T. E. O. ERICSON, in: *Preludes in Theoretical Physics* (A. DE SHALIT, H. FESHBACH and L. VAN HOVE, eds.) p. 321, North Holland, Amsterdam, 1965.
11. J. G. CRAMER, R. M. DEVRIES, D. A. GOLDBERG, M. S. ZISMAN and C. F. MACGUIRE, *Phys. Rev.* C14, 2158 (1976).
12. L. W. PUT and A. M. J. PAANS, *Phys. Lett.* 49B, 266 (1974).
13. W. E. FRAHN and R. H. VENTER, *Nucl. Phys.* 59, 651 (1964).
14. V. M. STRUTINSKY, *Soviet Phys. JETP* 19, 1401 (1964).
15. R. C. FULLER and K. W. MCVOY, *Phys. Lett.* 55B, 121 (1975).
16. R. C. FULLER, *Phys. Rev.* C12, 1561 (1975); R. C. FULLER and P. J. MOFFA, *Phys. Rev.* C15, 266 (1977).
17. G. R. SATCHLER, C. B. FULMER, R. L. AUBLE, J. B. BALL, F. E. BERTRAND, K. A. ERB, E. E. GROSS and D. C. HENSLEY, to be published.
18. M. E. BRANDAN, *Phys. Rev. Lett.* 49, 1132 (1982).
19. H. G. BOHLEN *et al.*, *Zeitschr. Phys.* A308, 121 (1982).
20. A. J. COLE *et al.*, *Phys. Rev. Lett.* 47, 1705 (1981).
21. D. A. GOLDBERG, S. M. SMITH and G. F. BURDZICK, *Phys. Rev.* C10, 1362 (1974).
22. R. M. DEVRIES, D. A. GOLDBERG, J. M. WATSON, M. S. ZISMAN and J. G. CRAMER, *Phys. Rev. Lett.* 39, 450 (1977).
23. D. DEHNHARD, V. SHKOLNIK and M. A. FRANEY, *Phys. Rev. Lett.* 40, 1549 (1978); erratum *Phys. Rev. Lett.* 42, 1574 (1979).
24. J. G. CRAMER, R. M. DEVRIES, D. A. GOLDBERG, M. S. ZISMAN and C. F. MACGUIRE, *Phys. Rev.* C14, 2158 (1976).
25. G. R. SATCHLER, *Nucl. Phys.* A279, 493 (1977).
26. Th. DELBAR, Gh. GREGOIRE *et al.*, *Phys. Rev.* C18, 1237 (1978).
27. D. M. BRINK and N. TAKIGAWA, *Nucl. Phys.* A279, 159 (1977).
28. M. S. HUSSEIN, H. M. NUSSENSVEIG, A. C. C. VILLARI and J. L. CARDOSO, Jr., *Phys. Lett.* 114B, 1 (1982); For an earlier discussion of the optical theorem in the context of heavy-ion scattering, see A. Z. SCHWARZCHILD, E. H. AUERBACH, R. C. FULLER and S. KAHANA, *Proc. Symp. on Macroscopic features of heavy-ion collisions*, p. 753, ANL/PHY-76-2 (1976).
29. M. C. COOPER and M. B. JOHNSON, *Nucl. Phys.* A260, 352 (1976); H. WOJCIECKOWSKI, D. E. GUSTAFSON, L. R. MEDSKER and R. H. DAVIS, *Phys. Lett.* 63B, 413 (1976).
30. W. A. FRIEDMAN, *Phys. Lett.* 126B, 13 (1983).
31. M. S. HUSSEIN, *Phys. Lett.* 127B, 165 (1983).
32. P. R. CHRISTENSEN and A. WINTHER, *Phys. Lett.* 65B, 19 (1976).
33. S. KAHANA, private communication 299 (1976).
34. For a recent review on the subject, see P. BRAUN-MUNZINGER and J. BARRETTE, *Phys. Rep.* 87, 209 (1982).
35. D. DENHARD, V. SHKOLNIK and M. A. FRANEY, *Phys. Rev. Lett.* 40, 1549 (1978).
36. W. E. FRAHN, M. S. HUSSEIN, L. F. CANTO and R. DONANGELO, *Nucl. Phys.* 369A 166 (1981).
37. P. DOLL, M. BINI, D. L. HENDIE, S. K. KAUFFMANN, J. MAHONEY, A. MENCHACA-ROCHA, D. K. SCOTT, T. J. M. SYMONS, K. VAN BIBBER, M. P. VIYOGI, H. WIEMAR and A. J. BALTZ, *Phys. Lett.* 76B, 566 (1978).

38. C. E. Thorn, M. J. Levine, J. J. Kolata, C. Flaum, P. D. Bond and J. C. Sens, *Phys. Rev. Lett.* **38**, 384 (1977).
39. A. J. Baltz, S. K. Kauffmann, N. K. Glendenning and K. Pruess, *Phys. Rev. Lett.* **40**, 20 (1978); *Nucl. Phys.* **327A**, 221 (1979); R. Donangelo, L. F. Canto and M. S. Hussein, *Nucl. Phys.* **320A**, 422 (1979).
40. M. S. Hussein, *Phys. Lett.* **88B**, 31 (1979); B. V. Carlson, M. S. Hussein and A. J. Baltz, *Phys. Lett.* **98B**, 409 (1981); *Ann. Phys.* (*NY*) **138**, 215 (1982).
41. W. G. Love, T. Terasawa and G. R. Satchler, *Phys. Rev. Lett.* **39**, 6 (1977); *Nucl. Phys.* **291A**, 183 (1977).
42. D. H. Gloeckner, M. H. Macfarlane and S. C. Pieper, Argonne National Laboratory, Rep. No. ANL-76-11 (unpublished) and *Comput. Phys. Comm.* **11**, 299 (1976).

NOTES ADDED IN PROOF

(1) We are indebted to C. Marty [private communication and *Z. Phys.* **A309**, 261 (1983)] for pointing out that eqns. (5.1) and (5.2) should be generalized, because the integral of (5.1) is, in the $\theta_0 \rightarrow 0$ limit, oscillatory and thus ill-defined. The imaginary part of $f(0) - f_{\text{Ruth}}(0)$ should be replaced by a linear combination of its imaginary *and* real parts, as Marty points out. In fact, Jeppesen *et al.* [*Phys. Rev.* **C27**, 697 (1982)] note that the resulting expression involves both real and imaginary parts of the "nuclear" amplitude (both of which contain the glory oscillation of Section 5), and describe a method of analysis which may permit the extraction of both of them from experimental data; Marty points out that this may be very difficult for heavy ion scattering.

(2) We are equally indebted to G.R. Satchler, who observes that our characterization of optical potentials as "refractive" or "diffractive", according to whether the Woods–Saxon parameter W/V is smaller or larger than unity, can be quite misleading. As Satchler points out, it is the value of $W(r)/V(r)$ in the *surface* region that counts, and this depends not only on W/V but also on the geometries of the two potentials. Dr. Satchler also informs us that our conjecture just above Fig. 24 is incorrect; a fit to the data does require that it is a_I rather than W which is varied with E.

We thank our colleagues for their interest, and happily stand corrected.

APPENDIX A

FERMAT AND THE DEFLECTION FUNCTION: LENSES AS PHASE-SHIFTERS

In Section 2.2 we obtained a high-energy approximation to $f_N(\theta)$, eqn. (2.10),

$$f_N(\theta) \approx \frac{1}{ik}\left(\frac{i}{2\pi\sin\theta}\right)^{1/2}\int_0^\infty e^{i[2\delta(\ell)-\ell\theta]}\ell^{1/2}\,d\ell, \tag{A.1}$$

by writing[4] the standing-wave $P_\ell(\cos\theta)$ as a sum of two running waves, $\exp[\pm i\ell\theta]$. It is more fundamental, however, to recognize (see, e.g., Schaeffer, Ref. 5b, eqn. 2.35) that $[2\delta(\ell)-\ell\theta] = S(\ell,\theta)$ is the classical-mechanics action, $\int \mathbf{k}(\mathbf{r})\cdot d\mathbf{r}$, integrated along the trajectory with impact parameter $b = \ell/k$ and scattering-angle θ. It then becomes clear that the stationary-phase approximation to eqn. (A.1) is nothing but Fermat's principle of least action or least time: starting with a plane wave incident on an "optical device" (scattering center or potential), the geometrical ray which exists with a deflection angle θ does so by choosing that impact parameter which minimizes its action:

$$\frac{d}{d\ell}[2\delta(\ell)-\ell\theta] = 0. \tag{A.2}$$

This nicely justifies the identification of $\theta = 2\delta'(\ell)$ as a "trajectory equation".

In the Glauber or small-θ approximation, e.g., the action is simply

$$S = S(\ell) = 2\delta(\ell) = \int_{-\infty}^\infty [k(z)-k]\,dz. \tag{A.3}$$

That is, the phase shift is the difference in phase accumulation (optical path length) between trajectories followed with and without the optical potential. The trajectory equation then asserts that the deflection angle θ depends on how rapidly this phase difference *changes* with impact parameter. In optical terms, e.g., a plane-parallel slab of glass shifts a ray "sideways", but does not change its direction because $\delta'(b) = 0$. A prism *can* bend rays, but since for it $\delta'(b) = $ const., it bends them all through the same angle. It can thus not bring parallel rays to a focus, but a lens can, by giving $\delta(b)$ a *non*-linear dependence on b. Since this provides a particularly simple example of a deflection function in a familiar context, we briefly work out the details in the thin-lens (small-θ) approximation. If, in Fig. A-1, the thickness of glass (of refractive index n) traversed at impact parameter b is $t(b)$, then the phase of a ray entering with this impact parameter is shifted relative to the $n = 1$ case by the optical path length

$$2\delta(b) = (n-1)kt(b). \tag{A.4}$$

From the figure, $t(b) = (R^2-b^2)^{1/2} - (R-T) \simeq T - b^2/2R$ for a plano-convex spherical lens, with $b \ll R$. Consequently

$$\frac{dt}{db} \simeq -\frac{b}{R},$$

and

$$2\frac{d\delta}{d\ell} = (n-1)k\left[\frac{1}{k}\frac{dt}{db}\right] = -\frac{(n-1)}{R}b. \tag{A.5}$$
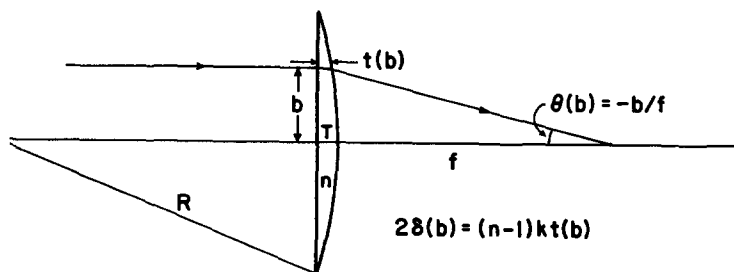

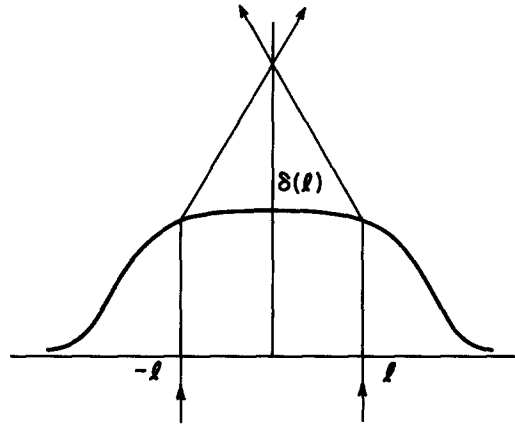Fig. A-1. Application of the deflection-function equation, $\theta(b) = 2d\delta/d\ell$, to a thin lens.

Fig. A-2. $\delta(\ell)$ for a real nuclear potential, viewed as a spherical lens.

However, recalling the "lensmaker's equation", which gives the focal length of this lens as $f = R/(n-1)$, we see that our deflection function for this Far-side ray is simply

$$\theta(\ell) = -b/f, \tag{A.6}$$

exactly the angle required to send all parallel rays through the focal point.

Looked at this way, a curve of δ vs. b for any spherically-symmetric potential is nothing but a cross section of the equivalent lens. Fig. A-2 shows a typical example for a Woods–Saxon type real potential with $a \ll R$. The equivalent "lens" is nearly a spherical ball of glass, with a thin "equatorial ridge" coming from the tail of the potential. In the WKB approximation, $\delta(b)$ has a *vertical* slope for $b \gtrsim R$ for such a potential, provided $E < E_F$ (Fig. 9). This corresponds to a logarithmic singularity in $\theta(b)$, which is the "orbiting" phenomenon that makes the slope of $\sigma_F(\theta)$ steeper than that of $\sigma_N(\theta)$, and so leads to the entire Fraunhofer crossover phenomenon.

For the Coulomb potential, on the other hand,

$$\theta(\ell) = 2\tan^{-1}\eta/\ell \approx 2\eta/\ell \tag{A.7}$$

for large ℓ, implying that

$$2\delta(\ell) \approx 2\eta \ln(\ell), \tag{A.8}$$

i.e., $\delta(\ell)$ *increases* with ℓ. The equivalent lens is thus *diverging*; because its curvature is small, we approximated it in Section 3.5 as a prism, whose effect is to *shift* $\sigma_N(\theta)$ relative to $\sigma_F(\theta)$, rather than to change their slopes, as Fig. 14 illustrates.

APPENDIX B

THE KNOLL–SCHAEFFER–GLAUBER–BORN APPROXIMATION
TO THE DEFLECTION FUNCTION IN THE $E \gg V$ LIMIT

Knoll and Schaeffer[5] obtained a simple approximation to $\theta(\ell)$ by expanding the WKB $\theta(\ell)$ to first order in V/E. We show that this Born approximation is equivalent to using the Glauber approximation to the phase shift, and point out a very simple interpretation of it.

In the high-energy, small-θ limit Glauber approximates the phase shift by an integral along a straight-line trajectory,

$$2\delta(b) = -\frac{k}{2E} \int_{-\infty}^{\infty} V[(b^2 + z^2)^{1/2}]\,dz. \qquad (B.1)$$

In this approximation the deflection function is

$$\theta(b) = 2(d\delta/db)/k$$

$$= -\frac{1}{2E} \int_{-\infty}^{\infty} \frac{b}{\sqrt{b^2 + z^2}} V'[(b^2 + z^2)^{1/2}]\,dz$$

$$= -\frac{1}{E} \int_{0}^{\infty} \frac{b}{r} V'(r)\,dz$$

$$= -\frac{1}{E} \int_{b}^{\infty} \frac{b}{\sqrt{r^2 - b^2}} V'(r)\,dr, \qquad (B.2)\,(B.3)$$

using $r^2 = b^2 + z^2$. This is exactly eqn. (4.32) of Knoll and Schaeffer;[5] they replace b by r_0, but since, according to our eqn. (2.15), $b = r_0[1 - V(r_0)/E]^{1/2}$, $b \approx r_0$ to lowest order in V/E.

Written in the form

$$\theta(b) = \frac{1}{2E} \int_{-\infty}^{\infty} \frac{b}{r} V'(r)\,dz, \qquad (B.4)$$

this small-angle approximation to $\theta(b)$ has a very simple physical interpretation, for $-V'(r) = F_r(r)$, the radial component of the force on the particle at a distance r from the center of the potential. But b/r is just the cosine factor necessary to project out the component of this force transverse to the straight-line trajectory, $-(b/r)V'(r) = F_\perp(r)$. The Glauber approximation neglects momentum transfer *along* this line (which is second-order in θ), so $v_\parallel$ is
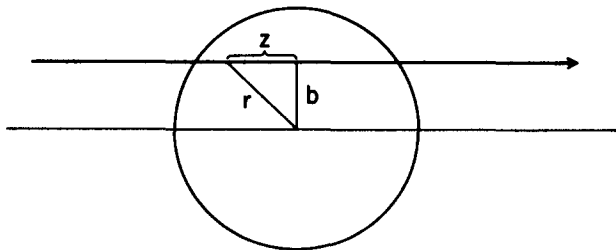

Fig. B-1. The straight-line trajectory of the Glauber approximation, indicating phase-shift accumulation as the trajectory passes through the potential.

constant and we can rewrite the z-integral as a time-integral, $dz = v_\parallel dt$:

$$\theta(b) = \frac{1}{2E} \int_{-\infty}^{\infty} v_\parallel F_\perp(r) \, dt$$

$$= \frac{mv_\parallel}{k^2} \int_{-\infty}^{\infty} F_\perp \, dt$$

$$= \frac{k_\perp(b)}{k_\parallel}. \tag{B.4}$$

That is, although in this approximation its trajectory is a straight line, it accumulates transverse momentum transfer, giving the deflection function the classical mechanics interpretation

$$2\delta'(b)/k = \theta(b) \simeq \sin \theta(b) = k_\perp(b)/k_\parallel. \tag{B.5}$$